A study about the behavior and mechanism of all-optical switching

Tianxun Huang

To cite this version:

Tianxun Huang. A study about the behavior and mechanism of all-optical switching. Physics [physics]. Université de Lorraine; Beihang university (Pékin), 2023. English. NNT : 2023LORR0054 . tel-04205005

HAL Id: tel-04205005
https://hal.univ-lorraine.fr/tel-04205005v1

Submitted on 12 Sep 2023

Thèse

Présentée et soutenue publiquement pour l'obtention du titre de

DOCTORAT DE L'UNIVERSITE DE LORRAINE

Mention : **Physique**

par

Tianxun Huang

A study about the behavior and mechanism of all-optical switching

Soutenue le 30 Mars 2023 devant le jury composé de

M. Michael COEY, Professeur, Trinity College Dublin	Président de jury
Mme Olga KAZAKOVA, Professeure, National Physical Laboratory	Rapportrice
M. Andrei KIRILYUK, Professeur, Radboud University	Rapporteur
Mme Hélène BÉA, Professeure associée, Université Grenoble Alpes	Examinatrice
M. Gregory MALINOWSKI, Chargé de recherche, Université de Lorraine	Examinateur
M. Yong XU, Professeur, Beihang University	Examinateur
M. Stéphane MANGIN, Professeur, Université de Lorraine	Directeur de thèse
M. Weisheng ZHAO, Professeur, Beihang University	Co-directeur de thèse

Institut Jean Lamour
UMR 7198 - Université de Lorraine
Département de Physique de la Matiére et des Matériaux

Résumé

Afin de répondre aux besoins des futures technologies de stockage magnétique à haute densité, à faible consommation d'énergie et à haut débit, le développement d'une nouvelle méthode de manipulation de l'aimantation avec des temps d'inversion d'aimantation plus courts et une consommation d'énergie plus faible est l'une des tâches urgentes dans le domaine de la spintronique. La technologie laser à impulsions ultracourtes offre une nouvelle façon de manipuler le spin sur une échelle de temps femtoseconde, suscitant un grand intérêt de recherche dans les universités et l'industrie.

Deux méthodes de contrôle de l'aimantation par laser, l' retournement tout-optique dépendent de l'hélicité (AO-HDS pour all-optical helicity-dependent switching en anglais) et l' retournement tout-optique indépendent de l'hélicité (AO-HIS pour all-optical helicity-independent switching en anglais), ont récemment été découvertes et leurs mécanismes, comportements et applications ont fait l'objet de nombreuses discussions. Cependant, l'origine de ces deux phénomènes reste très controversée et ce sera la tâche principale de cet article.

Le mécanisme de l'AO-HDS a été étudié à l'aide d'un empilement multicouches Co/Pt présentant le phénomène AO-HDS. Les films ont été réalisée sur un barreau de Hall en un carré magnétique de 10×10 μm^2 et son comportement de commutation a été observé à différentes échelles de temps. La commutation de cette cellule magnétique peut être démontrée par dix impulsions laser successives polarisées circulairement. La dynamique de spin de AO-HDS peut être comprise par nucléation thermique de domaine magnétique induite par Gradient thermique et propagation de paroi de domaine.

Au cours des dernières années, l'AO-HIS n'a jamais été observé dans les transition-métaux terres-rares alliages, à l'exception du fait que la terre-rare est Gd. Pour étudier les caractéristiques de Gd, on a cultivé et étudié une série d'alliages Gd$_y$R$_{1-x-y}$Co$_x$ (R pour Tb, Dy ou Ho), l'AO-HIS peut être observé lorsque la composition de R est aussi faible que 1,5% au voisinage du point de ferrimagnétique compensation. Les diagrammes d'état décrivant les paramètres clés qui dépendent de la concentration de l'élément et de la dynamique de spin dans divers échantillons ont été étudiés, ce qui donne quelques suggestions sur l'origine de l'AO-HIS et ses applications futures en ingénierie.

Mots-clés : retournement tout-optique, renversement de l'aimantation, degré de spirale lumineuse, dichroïsme circulaire magnétique, spintronique ultra-rapide

Abstract

To meet the future needs of high density, low power consumption, and fast rate of magnetic storage technology, it is one of the urgent tasks in the field of spintronics to develop a new method of magnetization manipulation with shorter magnetization reversal time and lower energy consumption. Ultrashort pulsed laser technology offers a new way to manipulate spins in femtosecond timescale, sparking great research interest in both academia and industry.

Two methods of controlling magnetization by laser, all-optical helicity-dependent switching (AO-HDS) and all-optical helicity-independent switching (AO-HIS), are discovered recently and raise numerous discussion on their mechanisms, behaviors and applications. However, the origin of two phenomena is still largely debated, which will be the main task of this thesis.

A Co/Pt multilayered stack exhibiting AO-HDS phenomenon is employed to study the mechanism of AO-HDS. The film is fabricated to a 10×10 μm^2 magnetic square on a Hall bar and its switching behavior is observed optically and electrically at different timescale. The switching of this magnetic unit can be demonstrated with ten consecutive circularly polarized laser pulses. The spin dynamics of AO-HDS can be understood in terms of the magnetic domain thermal nucleation and domain wall propagation driven by thermal gradient.

For the past years, AO-HIS has never been observed in rare-earth transition-metal alloys except when the rare-earth is Gd. To study the speciality of Gd, a complete series of $Gd_yR_{1-x-y}Co_x$ (R represents Tb, Dy or Ho) alloys is grown and investigated, it is demonstrated that AO-HIS can be observed when the composition of R is as low as 1.5% near the compensation point of ferrimagnet. State diagrams describing the key parameters depending on the elements concentrations and spin dynamics in various samples are studied, providing some suggestion on the origin of AO-HIS and its engineering application in the future.

Keywords : all-optical switching, magnetization reversal, light helicity, magnetic circular dichroism, ultrafast spintronics

Acknowledgments

This part concludes all the people who have kindly offer much help for the accomplishment of my Ph.D. thesis, I am so appreciated that I can work with these lovely people during past years.

Firstly, I would like to thank my Ph.D. supervisor Stéphane Mangin. You took me as an intern when I was doing master in China, I had a wonderful internship here and decided to stay for purchasing a Ph.D. degree here. During the past three years, Stéphane provided countless help, whatever from science, laboratory or life. I always feel free on selecting the direction of research that I think worth focusing, and Stéphane always support my idea and offer very constructive suggestions based on my topic.

I would also like to thank my co-supervisor Weisheng Zhao from Beihang University. I did my bachelor and master in Beihang University, Weisheng leaded me to the field of spintronics and then established the collaboration with Université de Lorraine, this is the story about my coming to Nancy. Weisheng offered me the opportunity to study the direction that I am interested in and to do research in both China and France.

I thank prof. Olga Kazakova and prof. Andrei Kirilyuk for reading my manuscript and giving very Valuable suggestions in the brief reports, as well as the remaining members of my Ph.D. jury. The discussions we had during the defense are very helpful for my thesis and publication of new results. I am especially grateful to prof. Michael Coey for being the president of my defense, I admired you a lot before starting my PhD studies, I learned some new understanding towards all-optical switching from you during the defense.

I am so appreciated to all the members of the Nanomagnetism and Spintronics team at Institut Jean Lamour, I would never be able to carry this work out without the help of our professional team. I would like to deeply thank Julius Hohlfeld, you followed my project all the way, I think it was you who defined our theory to explain our results. I am deeply impressed by your scientific spirit, which will guide me in my future work and study. I would like to thank Gregory Malinowski, I feel so lucky that we share the same office and we do experiments together in the laser room, many problems on my experiments solved with the help of you, you have to let me know when you come to China next time, I will take care of you warmly. I thank Michel Hehn for growing samples and also teaching me the usage of PVD system, as well as all the explanation and suggestions on my results, I enjoy every moment you deduce the formula for me. Sébastien Petit-Watelot offers lots of help for the electrical system of my research on all-optical helicity-dependent switching, Daniel Lacour did lots of work for the magnetic characterization of my samples. And Laurent Badie helped me a lot on the fabrication of our device, of course I learnt a lot about the process of micro-nano fabrication from him, I always feel relax and happy when working with Laurent in clean room. I would also like to thank Jon Gorchon and François Montaigne for having lots of discussions on my research.

I would also like to thank all the post-docs and Ph.D. students of our team, Leo, Wei Zhang, Maxime, Danny, Yi Peng, Heloïse, Yann, Quentin, Thibaud, Junta, Eva, Yaohan, Anna, Kaushal. I would especially like to thank Wei Zhang, we did most of the experiments and discussion together, you helped me so much in the formation of my work, I can't imagine how would I carry everything out without you, I think you are kind of my another supervisor to me. And you are my best partner in laser room, I will never forget those moments, the excitement when we see skyrmions after shining laser pulse, or the disappointment when we fail to move the skyrmions by electrical current, I feel lucky that there is always someone sharing such emotion together with me.

I would like to thank my side from Beihang University, many of them accompanied me from the beginning to the end. I would especially thank Xiaoyang Lin, who is also my supervisor from Beihang, I learnt how to do science and what is spintronics from Xiaoyang at the very beginning. I thank Jiaqi Wei for taking care of me when I first came to France, you make my life and research much easier, I had a very happy internship thanks to Jiaqi. I thank Xiaofei, Hangtian, Zongxia, Chen, Wei Yang, for the company from Beijing to Nancy.

Surviving in a foreign country is never easy, especially when I did not speak much French, but thanks to all my friends, either in France or in China, many problems can be easily solved and I had a very happy Ph.D. time. I would thank all the supports from all my friends of Institut Jean Lamour, and Oussama, Qing Liu, Weizhao, Zeyu, Jinjing, Liqiang, Lai Wei. I also thank Hangtian and Zongxia, we traveled lots of places in Europe and I felt so happy and relax in the trip with you. I thank Wei Yang for taking me to Toul for fishing every weekend, I will never forget the moment we fished that 15kg carp, I hope we can find opportunity go fishing again some day after your coming back to China. I thank Yaohan and Chen for the ski time at Gerardmer, I thank Leo for the lunch time in CROUS … Many moments suddenly flashed in my mind frame by frame, I thank all the people who build this wonderful ride in Nancy for me.

Lastly, everything cannot be possible without the support and help from my parents and all my families, I feel lucky that my parents always support my every decision, Nancy is a place very far away from them but they never hesitated to encourage me coming here.

People are like birds by the sky, always flying back and forth. I think I would hardly get opportunity to work with these people again in the future, I hope to see you again in somewhere of the world.

Contents

General Introduction

In 1956, IBM produced the first hard disk drive (HDD)[1], it was a magnetic disk with 5 Mb data storage, which was a huge amount at that time. Now, over half century past, a portable HDD with over 1 Tb data storage can be easily purchased under the discovery and the application of giant magneto resistance effect[2;3]. With the massive information explosion in 21st century, magnetic storage will still maintain lots of influence considering its non-volatile capability and long-time-store capability. Because magnetic memory takes advantage of the two different magnetic orientations of a unit to record information, the writing method of changing the magnetization direction is always popular and necessary to improve the storage performance including power consumption and calculation speed.

Indeed, conventional HDD use a magnetic head with a huge current-generated magnetic field to write-in the information. However, with the decreasing of grain and bit size, high-coercivity material has to be used to maintain the thermal stability for high-density storage, it brings challenges for the generated field of magnetic head as a result. Additionally, the moving magnetic head hinders the development of stability and portability of a storage system. Hence, finding other solutions for magnetization manipulation is an attractive topic in recent two decades. A main solution of writing methods is using spin transfer torque (STT)[4;5] or spin orbit torque (SOT)[6;7] with the help of electric current pulse, which is limited in the nanosecond timescale in traditional silicon-based integrated circuits.

Another new approach to manipulate the magnetization is by using ultrashort laser pulse, this is called all-optical switching (AOS) since no magnetic field or electrical current is introduced in this phenomenon. Indeed, two different types of AOS have been discovered so far : all-optical helicity-independent switching (AO-HIS) in which the magnetization can be switched by a single shot of pulse and its orientation is independent to the helicity of light, and all-optical helicity-dependent switching (AO-HDS) in which the magnetization orientation is determined by the helicity of light. The discovery of AOS has raised lots of attention because the applicability of a single linearly or circularly polarized ultrashort laser pulse to control the magnetization direction in ferromagnetic materials would significantly increase the speed and energy efficiency of data manipulation and therefore revolutionize modern information technology. However, even though the material system and switching behavior have been well studied over recent years, there are still many debates and issues about the mechanisms behind both two types of AOS that have not been solved so far.

Therefore, the main goal of this thesis is to study the behavior and dynamics of the laser-induced process and attempt to give possible mechanisms behind them. This manuscript will be organized in 4 chapters. In Chapter 1, a state-of-the-art of AOS will be presented, as well as some basic concepts and useful tools for better understanding the laser-induced spintronics. In Chapter 2, experimental methods we have used in this thesis will be introduced. In Chapter 3, we will dig into AO-HDS phenomenon, the magnetic properties, switching behavior and spin dynamics of a series of Co/Pt multilayers will be investigated. A combination of imaging system and electrical transportation helps to reveal the behavior of magnetization during and after each pulse excitation. Based on the experimental results, we will propose a model to describe the mechanism and some future direction of AO-HDS will be suggested. In Chapter 4. we study the mechanism of AO-HIS in a series of $\mathrm{Gd}_y\mathrm{R}_{1-x-y}\mathrm{Co}_x$ (R represents Tb, Dy or Ho) alloys. Toggle magnetization reversal by femtosecond laser pulse has been observed in most of the samples, even when the Gd concentration y is as low as 1.5%. By studying the revolution of some key parameters that determine the switching properties among the samples, some rule can be revealed to better understanding the mechanism of AO-HIS, as well as to identify the ideal material and beam parameters for AOS devices from the aspect of energy efficiency and system stability.

Chapitre 1

State-of-the-art of all-optical switching

In this chapter, we will give a general overview of the discovery, mechanism and recent progress on two phenomena of AOS.

1.1 The discovery of AOS

1.1.1 Two phenomena of AOS

The AOS was firstly observed by Stanciu *et al.*[8] in 2007, they demonstrated that the magnetization can be reversed with circularly polarized femtosecond laser pulses. The sample was grown by magnetron sputtering in a multilayered structure : glass/AlTi(10 nm)/SiN(5 nm)/GdFeCo(20 nm)/SiN(60 nm), they excited the sample with a 40-fs laser pulse train at a wavelength of 800 nm and a repetition rate of 1 kHz. As shown in figure 1.1 (a-b), White and black area correspond to $\boldsymbol{M}^-$ and $\boldsymbol{M}^+$ magnetization orientations respectively, after sweeping the σ^+ circularly polarized laser beams (resp. σ^-) from left to right, the exposed $\boldsymbol{M}^-$ area (resp. $\boldsymbol{M}^+$) has been switched to $\boldsymbol{M}^+$ (resp. $\boldsymbol{M}^-$), and $\boldsymbol{M}^+$ area keeps their initial magnetization. For the area swept by linearly polarized (L) laser, a multi-domain state is created in contrast. This work clearly demonstrated that magnetization can be reversed with circularly polarized laser pulse without any applied magnetic field. And in this phenomenon, the direction of magnetization is only determined by the helicity of light, hence this type of behavior is referred as all-optical helicity-dependent switching (AO-HDS).

In order to investigate the mechanism of AO-HDS, they tried to focus the static laser pulse train on a domain wall as shown in figure 1.1 (c). The black, white and gray area correspond to three different magnetic states respectively as : $\boldsymbol{M}^-$, $\boldsymbol{M}^+$ and multi-domain state. The multi-domain area consisting of many small randomly oriented domains occupies the most area in the center of exposed area. While on the boarder of multi-domain area, a clear ring can be observed, and σ^+ (resp. σ^-) pulse train leads to a $\boldsymbol{M}^+$ (resp. $\boldsymbol{M}^-$) ring. For the linearly polarized laser, no ringlike switching can be seen, replaced by a full multi-domain state. Because the fluence of laser spot from center to edge follows a Gaussian distribution, and the ring area indicates a proper laser fluence window where the light can perfectly manipulate the magnetization of sample. When the laser is sweeping in one direction, even though the central area is demagnetized to multi-domain state firstly, as the ring sweeps by, the magnetization is unified to the helicity of light in the end. The result of Stanciu *et al.*[8] firstly presented that magnetization can be reversed in a reproducible way by light, since then, numerous studies on AOS have begun.

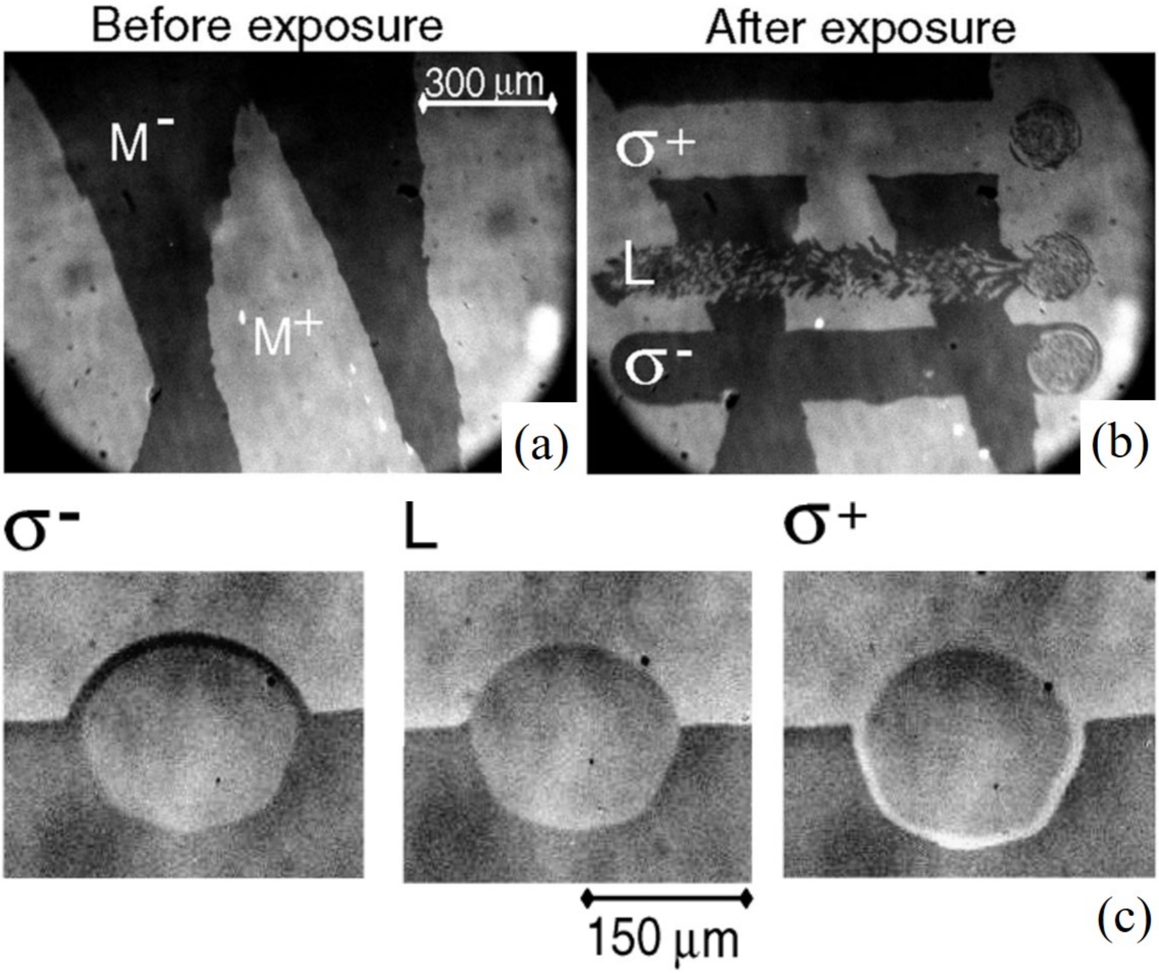

FIGURE 1.1 – The AO-HDS phenomenon in GdFeCo alloy. (a) The initial magnetic state before laser exposure. White and black areas correspond to $\boldsymbol{M}^+$ and $\boldsymbol{M}^-$ domains, respectively. (b) Domain pattern obtained by sweeping linear (L), right (σ^+), and left (σ^-) circularly polarized beams across the sample surface, with a laser fluence of about 11.4 mJ/cm^2. (c) Images of the laser spot focused onto a domain wall during the 1 kHz pulsed laser excitation with linear (L), right (σ^+), and left (σ^-) circular polarization. The central region is demagnetized (gray color) due to extensive heating. For circularly polarized excitation, helicity-dependent switching takes place on the perimeter of the excited area.[8]

In 2011, Radu *et al.* reported a fantastic discovery in GdFeCo alloy[9]. They observed that GdFeCo ferrimagnetic alloy with out-of-plane magnetic anisotropy can actually be switched by a single linearly polarized femtosecond pulse. As shown in figure 1.2, after sending the first femtosecond pulse on the material, the area exposed to the laser beam will change its magnetization, and sending a second pulse on the same area can switch the magnetization back. Every single pulse excitation will trigger a toggle magnetization reversal, and such behavior is not related to the helicity of laser, hence it is referred as all-optical helicity-independent switching (AO-HIS). The discovery of AO-HIS aroused great interest among researchers, because using ultrashort light pulse to switch the magnetization within several pico- or sub-picoseconds can be a promising method for ultrafast data writing of magnetic memories and greatly improves the speed of data processing. Since then, lots of similar results have been reported successively[10–13], confirming the existence of AO-HIS in GdFeCo alloys.

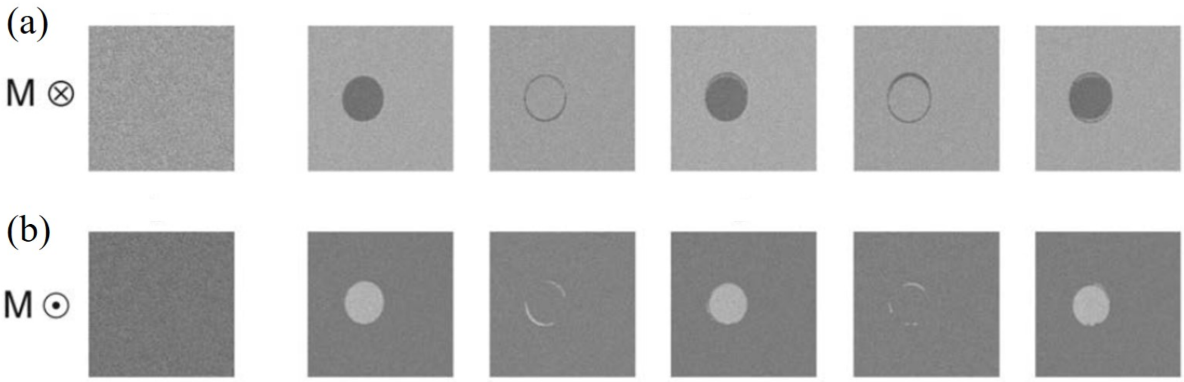

FIGURE 1.2 – The AO-HDS phenomenon in GdFeCo alloy. The magnetization is initially saturated to (a) $\boldsymbol{M}^+$ or (b) $\boldsymbol{M}^-$, after sending a linearly polarized femtosecond pulse on the material, the area exposed to laser beam will change its magnetization, and sending a second pulse on the same area can switch the magnetization back.[9]

Researchers began to realize that there are actually two phenomena of AOS : AO-HIS where the switching can be accomplished with a single shot of laser pulse and is not related to the helicity of light, and AO-HDS where the magnetization reversal is related to the helicity of light. Meanwhile, many questions are aroused on the mechanism of AOS, for AO-HDS, its origin can be simply interpreted as the different absorption of angular momentum from circularly polarized laser, while for AO-HIS, linearly polarized laser pulse brings no angular momentum but only heat. As a result, the enthusiasm of researchers has been greatly stimulated since then, and a large number of studies have been reported on these two different phenomena focusing on material systems, mechanisms and their applications.

1.1.2 AO-HIS

After the first observation of AO-HIS in GdFeCo alloy, many attempts were carried out to find other materials that exhibit this fascinating behavior. However, it is until recent two years that some new materials without Gd have been found to show AO-HIS[14–16], while at the beginning, AO-HIS is only been found in Gd-based ferrimagnetic materials, such as GdFeCo alloy[9–13], GdCo alloy[17–19], Gd/Co multilayers[20;21]. Indeed, GdFeCo alloy is composed of two sublattices : Gd and FeCo, and they are antiferromagnetic coupled, which means their magnetization is always opposite to each other at room temperature, such similar structures which are composed of rare-earth materials and transition-metal materials (RE-TM) have been extensively studied on AO-HIS, such as TbCo alloy[22–24], DyCo alloy[25], HoCo alloy[26], but none of these materials has shown a typical AO-HIS when Gd is absent. There are lots of reasons why Gd is so special that lead to its sdpecial behavior, for example, Radu *et al.* studied the demagnetization time of Gd when exposed to femtosecond laser[9], which is considered to be the most possible origin of AO-HIS ; Zhang *et al.* studied the influence of spin-orbit coupling of Gd by engineering a series of $Gd_{1-x-y}Tb_yCo_x$ samples[24] ; Ceballos *et al.* proposed that engineering the element specific damping of material would be a possible direction to explain AO-HIS in GdCo and find AO-HIS in other materials[23]. According to all the reports so far, it seems that the material to show AO-HIS has to possess two antiferromagnetic coupled sublattices, and Gd is indispensable in the material.

There are still lots of debates on its exact microscopic mechanism, but the pure thermal origin of AO-HIS is well recognized when Wilson *et al.* demonstrated a magnetization reversal in GdFeCo by hot-electrons[27]. They studied a sample of Pt(5 nm)/Au(h nm)/GdFeCo(10 nm) trilayers irradiated at the Pt surface as shown in figure 1.3. AO-HIS can be observed from GdFeCo side in all samples varying Au thickness h from 0 to 200 nm. In this work, the Pt/Au layer serves as an optical absorber and generates thermal current differs to GdFeCo layer. This is an exciting report to prove that AO-HIS could be a pure thermal effect and opens a door to ultrafast magnetization manipulation in spintronic devices. Then, Yong *et al.* observed same result in a similar structure and demonstrated that the reversal takes place in 5 picoseconds[28]. All above results indicate that ultrafast heating of the electronic system is the driving force of AO-HIS in GdFeCo. Besides optical pulse or hot-electron pulse, Yang *et al.* demonstrated that a picosecond electrical current pulse is able to reverse the magnetization in GdFeCo as well[29]. Therefore, the ultrafast magnetization reversal can be attributed to an instantaneous injection of energy, here "instantaneous" refers to the scale of pico- or sub-picosecond, and ultrashort optical pulse is just one of the energy injection methods leads to AO-HIS.

Although the first observation of AO-HIS in GdFeCo has been observed in 2011, it was until 2020 that the second material exhibits AO-HIS was demonstrated[14]. Banerjee *et al.* reported the toggle switching in half-metallic ferrimagnetic Heusler alloy Mn_2Ru_xGa (MRG). Another recent progress in new materials is from Avilés-Félix *et al.*[15], AO-HIS in Tb/Co multilayers was firstly demonstrated, this result is very astonishing because single-shot switching has never been shown in TbCo or other RE-TM alloys except Gd-TM alloys.

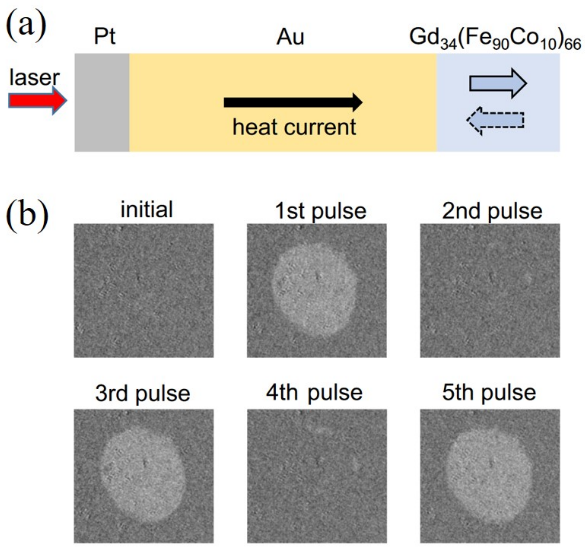

FIGURE 1.3 – Magnetization reversal by hot-electrons in GdFeCo. (a) A laser pulse irradiates the Pt surface and deposits energy in the electrons of Pt and Au. Hot-electrons diffuse across the Au layer to GdFeCo layer. (b) The magnetization can be reversed by such hot-electron pulse as it is switched by ultrashort laser pulse.[27]

1.1.3 AO-HDS

Comparing to AO-HIS, AO-HDS is a more general phenomenon because it has been demonstrated in various materials. After its first observation in GdFeCo[8], AO-HDS in other amorphous RE-TM ferrimagnetic alloy films like TbCo[30] and TbFe[31] have been reported. Then Mangin *et al.* concluded that AO-HDS can be observed not only in RE-TM alloys but also in a broad range of materials, including RE-TM multilayers and heterostructures[26]. Not only in ferrimagnetic materials, AO-HDS has also been observed in ferromagnetic materials, Lambert *et al.* studied numerous ferromagnetic multilayer systems including Co/Pt, Co/Pd and Co/Ni[32], all these material systems exhibit typical AO-HDS phenomenon. All these reports indicate that AO-HDS can exist in most material including RE-TM system and ferromagnetic system.

In 2017, a unique type of AO-HDS phenomenon was reported in cobalt-substituted yttrium iron garnet (YIG :Co)[33]. YIG :Co is an optically transparent ferrimagnetic dielectric which has four magnetic states and complex domain pattern due to its special magneto-crystalline structure as shown in figure 1.4 (a). The magnetic state after an irradiation of laser pulse can be manipulated by the polarization of pulse as shown in figure 1.4 (b), a single laser pulse polarized along [100] axis will lead to a switching from $\boldsymbol{M}^{(L)}{}_{+}$ to $\boldsymbol{M}^{(L)}{}_{+}$ and another switching from $\boldsymbol{M}^{(S)}{}_{-}$ to $\boldsymbol{M}^{(S)}{}_{+}$ at the same time, and all the magnetization can be restored by pumping a pulse polarized along [010] axis. This work demonstrated the first single-shot AO-HDS phenomenon and open up a new opportunity for the design and development of opto-magnetic memory device. However, YIG :Co is a very special magnetic material compares to conventional and popular ferromagnetic

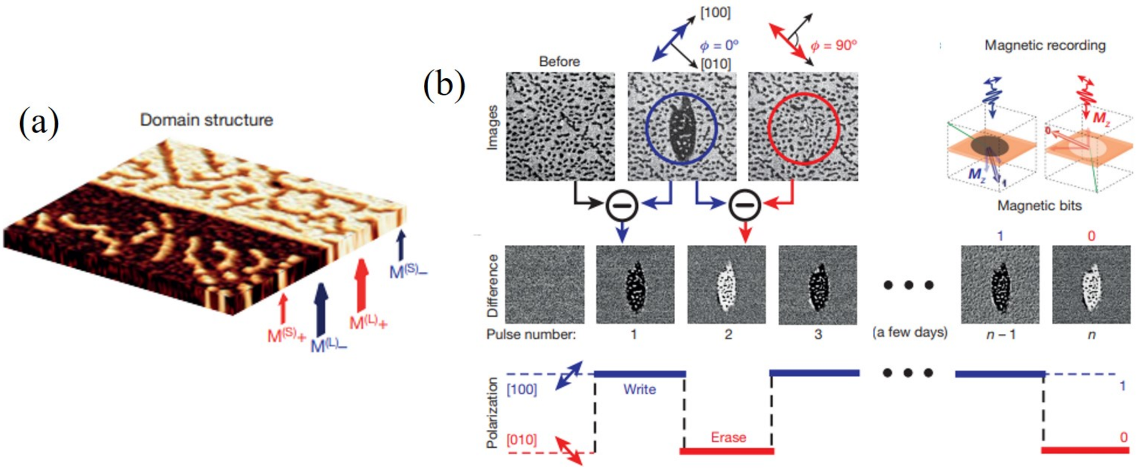

FIGURE 1.4 – (a) Four magnetic states and domain structure of YIG :Co. (b) single-shot AO-HDS phenomenon in YIG :Co, a single laser pulse polarized along the [100] axis will lead to a switching from $\boldsymbol{M}^{(L)}{}_{+}$ to $\boldsymbol{M}^{(L)}{}_{+}$ and another switching from $\boldsymbol{M}^{(S)}{}_{-}$ to $\boldsymbol{M}^{(S)}{}_{+}$ at the same time, and all the magnetization can be restored by pumping with a pulse polarized along [010] axis[33].

materials, and there is no other material has been found to exhibit such single-shot and helicity-dependent switching so far.

The discovery of magnetization reversal by laser pulse in GdFeCo by Stanciu *et al.*[8] attracted great interest among researchers, due to its advantage of ultrafast manipulation of magnetization and mysterious opto-magnetic interaction. However, before the well understanding of AO-HIS, the presentation of AO-HDS in vast material further complicated the study of AOS phenomenon. Even though more and more new materials show AO-HIS or AO-HDS are being dug up and the dynamics of switching process has been well studied, the mechanism behind AOS remains mysterious so far, which is also the main concern of this thesis.

1.2 Laser induced spin dynamics in magnetic films

Before understanding the physics behind AOS, it is necessary to introduce some basic concepts in magnetism, light and their interactions. All the samples discussed in this thesis show perpendicular magnetic anisotropy (PMA), which means the magnetic moments aligned perpendicular to the film plane. PMA is a crucial factor for magnetic film in emerging spin-electronic technology, and most of the research on AOS is based on systems with PMA, so is this thesis. In the following, we will start by presenting the magnetic interactions that help for the establishment of PMA in magnetic film.

1.2.1 Magnetic interactions

Heisenberg exchange interaction

In a ferromagnetic system, atomic magnetic moments can overcome the adverse effect of thermal disturbance and be arranged orderly, this can be well explained by Weiss molecular field theory and Heisenberg model.

The interaction between two electron spins is called exchange interaction, and this kind of interaction is the result of the competition between Pauli's exclusion principle and the Coulomb interaction. The Heisenberg exchange interaction thinks, exchange interaction between atoms strongly exists in magnetic materials, and only between neighboring atoms. The spin interaction energy between atoms can be expressed as :

$$E_{ex} = -2J \int \overrightarrow{S_i} \cdot \overrightarrow{S_j} \tag{1.1}$$

Where J is called exchange integral and $\overrightarrow{S}$ is the total spin moment of corresponding atom. If J is positive, the system favors a ferromagnetic state at which the system energy will be minimized, whereas the negative J leads to antiferromagnetic state. This gives the reason why the spins tend to be aligned in parallel or antiparallel.

From Heisenberg model, the conditions for materials exhibit ferromagnetic behavior are : first, the atom has an incomplete electron shell, that is, the material has atomic magnetic moment ; second, the exchange integral J has to be positive.

Zeeman interaction

A magnetic moment μ tends to align towards an external magnetic field H, as the needle on a compass aligns to the earth's magnetic field. The interaction between the magnetic moment and external field is called Zeeman interaction :

$$\delta E_Z = -\mu_0 H \cdot \mu \tag{1.2}$$

And the total energy :

$$E_Z = -\mu_0 \iiint H(r) \cdot M\,(r)\, d^3 r \tag{1.3}$$

Dipolar interaction

A magnetic moment μ has its own environment which brings influence to its neighboring spins, this is called dipolar interaction. The environment can be understood as a magnetic field H_D related to the distance to the magnetic moment r :

$$H_D = \frac{1}{4\pi}\left[\frac{(\overrightarrow{\mu} - \overrightarrow{r}) \cdot \overrightarrow{r}}{r^5} - \frac{\mu}{r^3}\right] \tag{1.4}$$

In a permanent magnetized sample $\overrightarrow{M}$, the total dipolar field is the sum of all individual dipolar fields of its many small magnetic dipoles. The dipolar field outside the magnetic material is called "stray field", and inside the material is called "demagnetizing field" because it points to the opposite direction of $\overrightarrow{M}$ and tends to lower the total magnetization of system. Under this demagnetizing field, the demagnetizing energy is defined as :

$$E_d = -\frac{1}{2}\int_V \overrightarrow{H_D} \cdot \overrightarrow{M} dV \tag{1.5}$$

But the computation of dipolar interaction considering all the elements in an actual material would be very complicate. Hence, there is another way to represent the total dipolar field as :

$$H_D^T = -N \cdot \overrightarrow{M} \tag{1.6}$$

Where N is the demagnetizing tensor. Consider the case of a simple ellipsoid, the demagnetizing field can be written as :

$$H_D^T = -\begin{pmatrix} N_{xx} & 0 & 0 \\ 0 & N_{yy} & 0 \\ 0 & 0 & N_{zz} \end{pmatrix} \cdot \overrightarrow{M} \tag{1.7}$$

And $N_{xx} + N_{yy} + N_{zz} = 4\pi$. For a thin film with magnetization along z-axis, which is the only case that will be discussed in this thesis, the ellipsoid can be considered with two infinite axis and then $N_{xx} = N_{yy} = 0$, $N_{zz} = 4\pi$. Hence, the demagnetizing energy per volume can be expressed as :

$$E_D = 2\pi M_z^2 \tag{1.8}$$

It is been called the shape anisotropy to describe the relationship between the demagnetizing energy and the shape of sample. From the equation, it can be seen that the demagnetizing energy is minimized when the magnetization points to in-plane ($M_z = 0$), which means that the shape anisotropy favors to bring magnetization to in-plane.

Magneto-crystalline anisotropy

In this thesis, Co/Pt film owns a strong out-of-plane magnetic anisotropy, however, when the magnetization points to its z-axis, the demagnetizing energy reaches a maximum and the shape anisotropy tends to bring magnetization to in-plane. Therefore, in order to keep PMA in Co/Pt film, the shape anisotropy must be overcome.

When measuring the magnetization curve of a single crystal material, it comes that the shape of curve is related to the crystal axis of material. Figure 1.5 demonstrates the magnetization curve follows different crystal direction in single crystal Fe, the magnetization shows anisotropy with different crystal direction, and this is called magneto-crystalline anisotropy (MCA). Because of MCA, there are some directions easier to be magnetized ([100] for Fe for instance), and these directions are called easy axis of magnetization, otherwise they are called hard axis.

With the concept of energy, the MCA can be well understood. The work required from

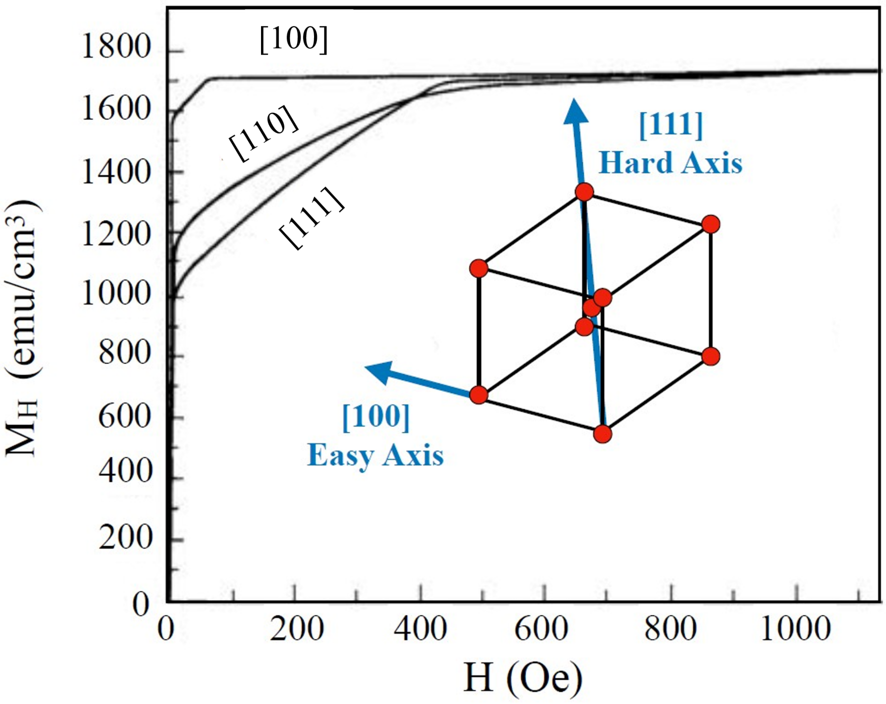

FIGURE 1.5 – Magnetization curve follows different crystal direction in single crystal Fe. Saturation is reached at lower field in [100] direction (easy axis) than in [111] direction (hard axis).

demagnetized state to saturation state for a ferromagnetic system is :

$$\int_0^M \mu_0 H \cdot dM = \int_0^M dE = E(M) - E(0) \tag{1.9}$$

The work for magnetizing, which is the left part of the equation, is determined by the area size between the magnetization curve and vertical M_H axis. The right part of the equation is the free energy increased during magnetizing, also called MCA energy. From figure 1.5, the MCA energy varies following different crystal direction in ferromagnetic crystal. Obviously, the anisotropy energy is minimized following the easy axis.

For hexagonal crystals such as Co, the hexagonal c-axis is the easy axis, and the plane to which c-axis is orthogonal is a hard plane of magnetizing. The anisotropy energy E_K can be described as :

$$E_K = K_1^{'}\sin^2\theta + K_2^{'}\sin^4\theta + \cdots \tag{1.10}$$

Here, $K_1^{'}$ and $K_2^{'}$ are called anisotropy constants, and the uniaxial anisotropy is mainly determined by the value of these constants. If $K_1^{'} = K_2^{'} = 0$, the ferromagnet is isotropic ; if $K_1^{'}$ and $K_2^{'}$ are positive, E_K is minimized when $\theta = 0$, meaning the c-axis is an easy axis ; if $K_1^{'}$ and $K_2^{'}$ are negative, the plane orthogonal to c-axis is an easy axis ; if $K_1^{'}$ and $K_2^{'}$ are of different sign, the boundary between uniaxial and planar anisotropy is defined by $K_1' = -K_2'$. In room temperature, all the anisotropy constant of Co is positive and it gets c-axis as the easy axis.

The magnetization tends to point to the easy axis because of the existence of MCA, acting like a magnetic field H_K is pulling the magnetization. The field H_K is called MCA field. Similarly, H_K in hexagonal crystal materials like Co can be described as :

$$E_K = \frac{2K_1'}{\mu_0 M_S} \tag{1.11}$$

Interfacial anisotropy

In 1954, Louis Néel proposed an interfacial contribution to MCA[34]. With the improvement of film deposition technology, the growth of very thin film in sub-nanometer scale had been realized, and this interfacial contribution was evidenced. The crystalline symmetry responsible for the quenching of orbital momentum is lost when the film thickness downs to the order of few atomic monolayers, and the increase of orbital momentum can be observed at the interface, leading a local enhancement of anisotropy. This phenomenon is especially obvious when a ferromagnetic material is interfaced with material showing large spin-orbit coupling, such as Pt, Ta, Ir. The interfacial anisotropy constant K_S (in J/m^2) can be used to describe the interaction by this interfacial phenomenon. The corresponding energy can be written as :

$$E_A = -\frac{K_S V}{t_{FM}}(m \cdot u)^2 \tag{1.12}$$

Where t_{FM} is the magnetic layer thickness and u is the direction of easy axis.

In a very thin film, like Co/Pt multilayers, the bulk MCA is usually neglected since the samples grown by physical vapor deposition is usually amorphous and their body effect is very weak. The interfacial anisotropy is dominant and becomes the main origin of PMA.

Perpendicular magnetic anisotropy

Finally, the sum of demagnetizing energy, MCA energy and interfacial anisotropy energy defines the direction of the easy axis of a sample. Therefore, we can use an effective anisotropy constant to determine the easy axis :

$$K_{eff} = \frac{K_S}{t_{FM}} + K_V - 2\pi M_s^2 \tag{1.13}$$

In this equation, the first term indicates the interfacial anisotropy, the second term is the bulk MCA which is not dominant in our case, and the third term is the shape anisotropy. The magnetization orientation is the result of the competition of shape anisotropy and interfacial anisotropy if we ignore the MCA. When K_{eff} is positive, meaning the interfacial anisotropy is greater and the sample will show a perpendicular magnetic anisotropy. Otherwise, the magnetization lays within the sample's plane.

1.2.2 Magnetic domains and domain wall

Magnetic domains

In ferromagnetic materials, exchange interaction exists between the electron spins of different atoms, the magnetizations of neighboring atoms will favor the same orientation below Curie temperature (T_C). Both theory and practice have proven the domain structure will form in a bulk ferromagnetic crystal under T_C, the magnetization orientation is unified inside each domain and varies between different domains. So that all the magnetization of domains is compensated and the system shows zero net magnetization in general under zero external magnetic field. A typical domain width is in the scale of about 10 μm,thus the volume is about 10^3 μm^3 and about 10^{14} magnetic atoms is contained in such a domain.

Why does the domain structure appears in ferromagnetic crystal ? What affects the size, shape and distribution of domain ? Indeed, the formation and properties of domain are determined by its minimum total free energy. As we discussed above, there are several interactions exist in a ferromagnetic system, and their corresponding energies are exchange energy (E_{ex}), Zeeman energy (E_Z), demagnetizing energy (E_D), MCA energy (E_K) and interfacial anisotropy energy (E_A). According to the principles of thermodynamics, a stable magnetic state must correspond to a state where the total free energy is minimized, the appearance of domain is the inevitable result from that a magnetic system balances its magnetization distribution and satisfies the principle of minimum energy.

In Co/Pt multilayers without the force of external magnetic field or stress, the magnetizatic state will be determined by the minimum total free energy of E_{ex}, E_D and E_A. E_{ex} results in the same spin orientation of neighboring atoms, leading to spontaneous magnetization ; while E_A is the reason why the spin orientation points to the easy axis. Hence, E_{ex} and E_A are minimized when the magnetization is saturated to easy axis and no domain will be generated. However, a uniform magnetization will cause the free pole at the surface of magnetic crystal with certain size and shape, leading to demagnetizing field. Demagnetizing field increases the total free energy and the spontaneous magnetizing state is no more stable. In order to decrease the surface demagnetizing energy, the spontaneous magnetization distribution has to be changed. Consequently, lots of regions with opposite orientation are generated in ferromagnetic system, every region is called a domain.

Domain wall

After the domains are formed, there is a transition on the order of 10^3 atoms wide between two neighboring domains, this transition is called domain wall (DW). In DW, the magnetic moment also follows the principle of minimum energy and gradually changes from one direction to another. Because the magnetization orientations are different inside the DW, the exchange energy and MCA energy will increase, constituting DW energy.

Even though forming more domains decreases the demagnetizing energy, meanwhile, creating more DWs elevates the system energy considering DW energy. Therefore, the number of domains is the results of the collective effect of E_D and DW energy.

Here we use a simplified model to calculate DW energy. Assuming that the spins rotate from $\theta = 0$ to $\theta = \pi$ in N atom layers. The exchange energy between to atoms is :

$$E_{ex} = -2AS^2 \cos\theta \tag{1.14}$$

Where A is the the exchange stiffness constant. For a simple cubic lattice, where a is the lattice constant, the number of atoms per unit area in each atom layer is $1/a^2$, and the number of neighboring spin pears per unit area in DW is N/a^2. The stored exchange energy per unit area in DW is :

$$\gamma_{ex} = AS^2 \frac{\pi^2}{Na^2} \tag{1.15}$$

The above equation indicates that, the thicker of the DW, the less exchange energy in DW.

On the other hand, every spin in DW deviates the direction of easy axis, causing the increase of MCA energy. The incremental of MCA energy per unit area in DW can be expressed as :

$$\gamma_K = \frac{NaK_1^{'}}{2} \tag{1.16}$$

Then, by calculating the minimum of $(\gamma_{ex} + \gamma_K)$, the thickness of DW can be obtained :

$$\delta = \pi S \sqrt{\frac{2A}{aK_1^{'}}} \tag{1.17}$$

And the DW energy per unit area is :

$$\gamma_W = \sqrt{2}\pi S \sqrt{\frac{K_1^{'}A}{a}} \tag{1.18}$$

According to the way of spin transitioning from one direction to another, the DW can be classified to two types : Bloch wall and Néel wall, as illustrated in figure 1.6. In Bloch wall, the spins are parallel to the plane of the DW during the transition, so that there is no free pole generated on the surface of DW, which makes sure that no demagnetizing field will be caused and the DW energy is minimized. But poles appear at the up and down surface of crystal, so usually Bloch wall shows up in a bulk material where the demagnetizing energy is ignorable.

Unlike Bloch wall, Néel wall is more favorable in an ultrathin magnetic film mostly. In Néel wall, the spins rotate following the normal direction of the film plane, then free poles generated on the two sides of DW. But when the DW width δ is much greater than

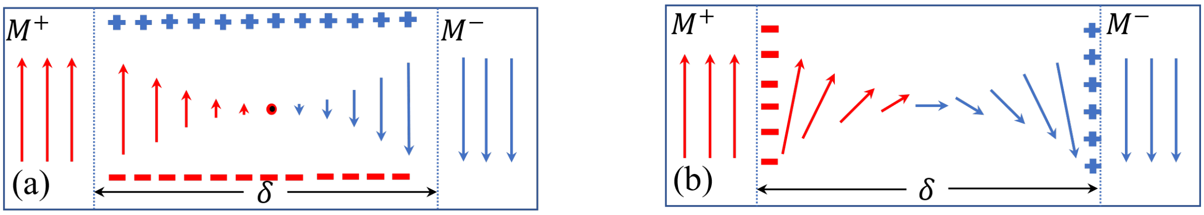

FIGURE 1.6 – Illustration of (a) Bloch wall and (b) Néel wall.

the film thickness, the demagnetizing field on the sides of DW is very small. To conclude, Bloch wall energy increases with decreasing the film thickness while Néel wall is opposite. Therefore, Bloch wall is more stable in a thick bulk ferromagnetic material and Néel wall is more stable in thin film.

1.2.3 Models of spin dynamics

It is important to understand the spin dynamics in ultrafast laser-induced magnetization experiments, in this section we present some models to explain the spin dynamics under external magnetic field first.

Static micro magnetism – Brown equation

When a micro magnetic system reaches its minimum of Gibbs free energy, the thermodynamics of this system reach equilibrium. And the Brown's equations allow one to find this equilibrium solution :

$$\overrightarrow{m} \times H_{eff} = 0 \tag{1.19}$$

And its boundary condition :

$$\frac{\partial E^{'}}{\partial m} + \frac{\partial E}{\partial (\nabla m)} \cdot n = 0 \tag{1.20}$$

It means that the magnetization has to be parallel to the effective field H_{eff} within the body at the equilibrium, or the torque exerted on magnetization by H_{eff} must vanish. Where H_{eff} is the sum of external field, exchange field, demagnetizing field, and MCA field :

$$H_{eff} = H_Z + H_{ext} + H_D + H_A = -\frac{1}{\mu_0 M_S}\frac{\partial E_{tot}}{\partial m} \tag{1.21}$$

Landau-Lifshitz-Gilbert equation

Brown equation gives the magnetization arrangement at the equilibrium, but the spin dynamics has to be studied when it comes to the magnetization revolution with time. For a magnetic moment m and its corresponding angular moment P, they satisfy :

$$\mu_0 \overrightarrow{m} = -\gamma_0 P \tag{1.22}$$

Where γ_0 is the absolute value of the gyromagnetic ratio :

$$\gamma_0 = \frac{g\,|e|}{2m_e c} \tag{1.23}$$

Where g is the Landé splitting factor, e is the electron charge, m_e is the electron mass and c is the speed of light.

Under the force of effective field H_{eff}, the magnetic moment feels the torque L :

$$L = \mu_0 \overrightarrow{m} \times H_{eff} \tag{1.24}$$

The precession of the spin magnetic moment around the field can be described as :

$$\frac{dP}{dt} = \mu_0 \overrightarrow{m} \times H_{eff} \tag{1.25}$$

And by recalling the definition of magnetization vector $\overrightarrow{m}$, the following continuum gyromagnetic precession model can be obtained :

$$\frac{\partial \overrightarrow{m}}{\partial t} = -\gamma_0 \overrightarrow{m} \times H_{eff} \tag{1.26}$$

From the equation, the length of vector $\overrightarrow{m}$ is constant, and the movement track of the vector end can be seen as a circle, that is to say the magnetization vector $\overrightarrow{m}$ is doing a non-dissipative precession.

While indeed, the precession of $\overrightarrow{m}$ will not last forever in real materials, because of the interaction with its environment, energy is been consumed. If there is no applied external torque, the end of $\overrightarrow{m}$ will spiral to the direction of H_{eff} gradually.

In 1955, Thomas Gilbert introduced a phenomenological damping effect into the precession of magnetization and came up with Landau-Lifshitz-Gilbert (LLG) equation[35] :

$$\frac{\partial \overrightarrow{m}}{\partial t} = \gamma \mu_0 \overrightarrow{m} \times \overrightarrow{H}_{eff} + \frac{\lambda}{\left|\overrightarrow{m}\right|} \overrightarrow{m} \times \frac{\partial \overrightarrow{m}}{\partial t} \tag{1.27}$$

Where the second term is the Gilbert damping term, and λ is the Gilbert damping factor, it indicates the speed that $\overrightarrow{m}$ rotates to H_{eff}. The origin of damping could be magnon-magnon interaction, magnon-phonon interaction etc. The value of λ can be measured using some methods like ferromagnetic resonance[36]. Even though the damping term cannot be rigorously calculated by energy transfer equations, but it describes the spin dynamics precisely.

Landau-Lifshitz-Bloch equation

However, LLG equation is a low temperature approach, in the story of AOS, thermal effect from laser dominates the physical behavior of the system. Landau-Lifshitz-Bloch

(LLB) equation combines the LLG equation at low temperature and the Bloch equation at high temperature. For $\overrightarrow{m}$ is the spin polarization normalized to its zero-temperature value, the LLB equation can be written in the form :

$$\frac{\partial \overrightarrow{m}}{\partial t} = \gamma \left[\overrightarrow{m} \times \overrightarrow{H}_{eff} \right] - \gamma \lambda_{\parallel} \frac{\left(\overrightarrow{m} \cdot \overrightarrow{H}_{eff} \right) \overrightarrow{m}}{m^2} + \gamma \lambda_{\perp} \frac{[\overrightarrow{m} \times [\overrightarrow{m} \times \overrightarrow{H}_{eff}]]}{m^2} \tag{1.28}$$

In LLB equation, the length of $\overrightarrow{m}$ is not assumed to be constant and its equilibrium value is temperature dependent. Comparing to LLG equation considering the usual precession and relaxation terms, the LLB equation also contains the term controls longitudinal relaxation. $\lambda_{\parallel}$ and $\lambda_{\perp}$ are the longitudinal and transverse damping parameters respectively, for $T < T_C$:

$$\lambda_{\parallel} = \frac{2\lambda T}{3T_C} \tag{1.29}$$

$$\lambda_{\perp} = \lambda(1 - \frac{T}{3T_C}) \tag{1.30}$$

For $T < T_C$:

$$\lambda_{\parallel} = \lambda_{\perp} = \frac{2\lambda T}{3T_C} \tag{1.31}$$

Here λ can be considered to characterizes the coupling between spins and the heat bath. The LLB equation can be very useful not only for the ultrafast laser induced magnetization dynamics, but also for the domain wall motion by the thermal gradient which could be one of the origins of AO-HDS.

1.2.4 Laser induced ultrafast demagnetization

Indeed, pulse laser technology has already been used to detect the relaxation time of electron-phonon coupling in non-magnetic metals for a long time. In 1987, Elsayed-Ali *et al.* demonstrated that the relaxation time in electron-phonon is in the order of several picoseconds[37]. Later, Fann *et al.* studied the relaxation time of hot-electrons in Au by similar methods[38]. During that period, a very important model called two temperature model was proposed to explain the coupling between electrons and phonons, this model has been widely used in lateral research on the ultrafast demagnetization of magnetic materials.

Afterwards, researchers started to study the laser induced dynamics in magnetic materials. Agranat *et al.* did not observed demagnetization in Ni thin film using picosecond laser pulses, but with nanosecond pulses[39]. Based on this, they proposed that the spin relaxation time is in the scale of tens of nanoseconds, which matches to the spin-lattice relaxation time. Later, Vaterlaus *et al.* reported that the spin-lattice relaxation time in Gd film is about 100 picoseconds by time resolved spin-polarized photoemission with picosecond laser pulse[40]. Another similar experiment shows that the spin relaxation time is between 30 ps and 20 ns in polycrystalline thin film of iron[41]. Before the year of 1996, scientists generally considered that the responsing time of spin to the light matches to the spin-lattice relaxation time, from tens of picoseconds to even nanoseconds.

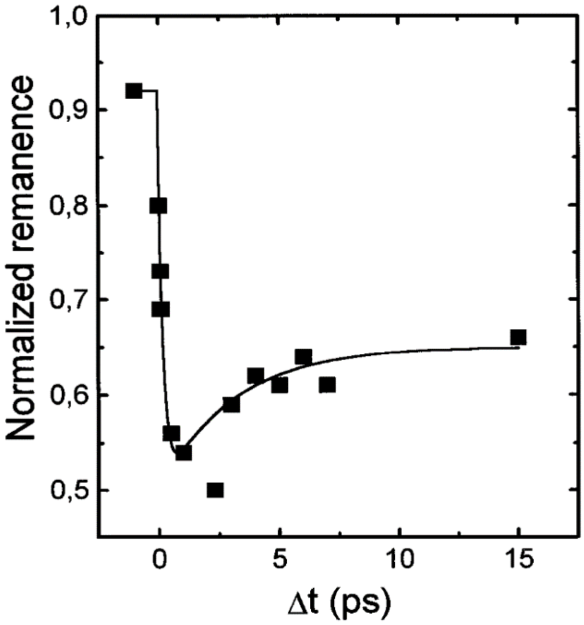

FIGURE 1.7 – Ultrafast demagnetization phenomenon induced by a 60-fs pump laser pulse in a Ni(20 nm)/MgF_2(100 nm) film.[42]

In 1996, Beaurepaire *et al.* reported an influential result[42]. They employed a pump laser with 60-fs pulse duration to measure time resolved magneto-optical Kerr effect, and observed an ultrafast demagnetization phenomenon, which is less than 1 ps, in Ni thin film, as shown in figure 1.7. This work is of great significance because they revealed that the response of spin to light is in the scale of femtosecond. Since then, lots of similar results have been reported successively. Hohlfeld *et al.* observed similar phenomenon in Ni film with the help of time resolved second harmonic effect[43], and they showed the magnetization changes with temperature follows the rule of classical thermal balance in 300 fs after the laser excitation. The ultrafast demagnetization in Co thin film also been demonstrated and its demagnetization time is even less than 50 fs, and Co thin film can be fully demagnetized when the laser fluence is high enough[44]. Later, Scholl er al. observed two different demagnetization process in two different time scale by femtosecond spin-resolved two-photon photoemission[45] : one is a very fast process in a subpicosecond time scale, and reaches 20% of demagnetization, maybe due to an excitation of Stoner pairs by hot electrons gas ; the second one is a slow process lasting for a few hundreds of picoseconds, which could be the spin-lattice interaction. This explanation made a connection to the previous results before the year of 1996.

Except for typical 3d metals Fe, Co and Ni, in the past 25 years, ultrafast demagnetization phenomenon has also been reported in massive and various systems, including alloy or multilayers like NiFe, $CoPt_3$, GdFeCo, Fe/Gd, Co/Pt[46], oxide system like CrO_2, Sr_2FeMoO_6, $La_{1-x}Sr_xMnO_3$[47–49], and magnetic semiconductors like InMnAs[50].

However, it is undeniable that our understanding of ultrafast demagnetization is not deep and accurate enough until now, with the discovery of AOS, more and more fundamental physics still need to be well explained. In the following, we will introduce some basic solutions and models most often used to study ultrafast demagnetization phenomenon.

1.2.5 Models of ultrafast laser induced spin dynamics

Phenomenological three-temperature model (3TM)

The nature of 3TM is to transfer the ultrafast spin dynamics into a relaxation of thermal effect. In this model, the electron, lattice and spin are regarded as three thermal baths which are coupled with each other, and their temperatures are changing under the excitation of external energy. Firstly, because the heat capacity of electron system is relatively small, its temperature increases rapidly, in the following the lattice and the spin are driven to change their temperatures. Because the three baths are coupled in specific coupling constants, the system will relax to an equilibrium state in the end. The three-temperature model can be described by the following three differential equations :

$$C_e\frac{\partial T_e}{\partial t} = -G_{ep}\left(T_e - T_p\right) - G_{es}\left(T_e - T_s\right) + S(t) \tag{1.32}$$

$$C_p\frac{\partial T_p}{\partial t} = -G_{ep}\left(T_p - T_e\right) - G_{ps}\left(T_p - T_s\right) \tag{1.33}$$

$$C_e\frac{\partial T_s}{\partial t} = -G_{es}\left(T_s - T_e\right) - G_{ep}\left(T_s - T_p\right) \tag{1.34}$$

Where, $S(t)$ represent the energy from laser, C is the heat capacity of three systems, G is the coupling strength between each other and T is their temperature respectively. 3TM assumes that the laser-induced ultrafast heating only occurs in the electron bath. A classic behavior of three temperatures with time was given by Beaurepaire *et al.* in figure 1.8[42]. The electron temperature rapidly rises up above Curie temperature and reaches a peak within the first 500 fs, this indicates that most of the laser energy is absorbed by electrons instantaneously due to electron-electron interactions[51]. Then the electron temperature experiences an exponential-like decay until reaching a saturation temperature at 550 K. The spin temperature rises much slower than electron temperature, but follows the same trend as the electron temperature after reaching a broad maximum $T_s = 580K$ at 2 ps. The decay of electron temperature is because electrons transfer their energy to the lattice by electron-phonon interaction, leading to the increase of lattice temperature. In the end, the three thermalized baths reach a quasi-equilibrium state.

The advantage of 3TM is that people can easily understand and accept ultrafast demagnetization phenomenon from the phenomenological point of view, until now, it is still

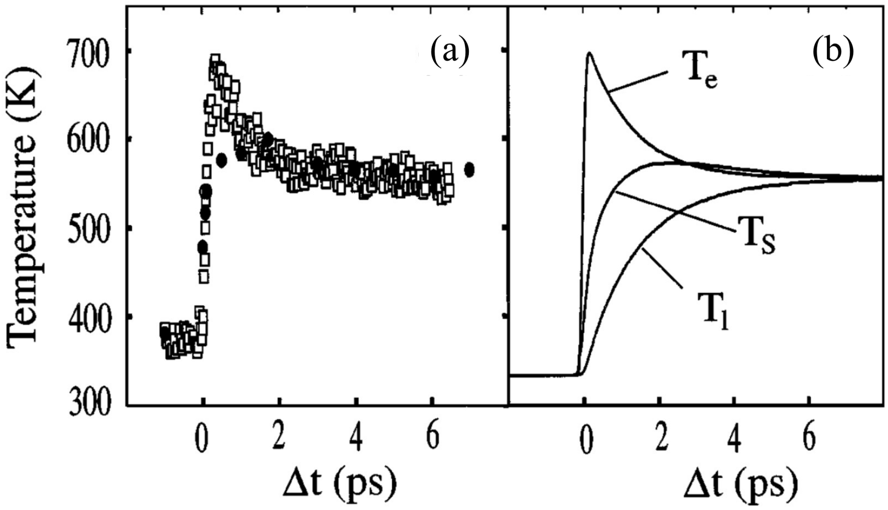

FIGURE 1.8 – (a) Spin (T_s) and electron (T_e) temperatures from experiment, where open squares are T_e and solid dots are T_s. (b) Calculated spin (T_s), electron (T_e) and lattice (T_p) temperatures from 3TM.[42]

of great significance for a beginner in ultrafast spin dynamics. But there are two disadvantages of this model, first, it only considers the energy transfer between three thermalized reservoirs but ignores the exchange of angular moment, which is more important especially when one considers the revolution of spin ; second, 3TM only reveals the spin temperature with time, however, it is meaningless to define the spin temperature under high non-equilibrium state, the revolution of magnetization with time is more important.

Atomistic spin dynamics model

the atomistic spin dynamics model is based on the phenomenological LLG equation. Let's now rewrite the LLG eqaution to describe the dynamics of spin S_i at each localized lattice as :

$$\frac{\partial \overrightarrow{S}_i}{\partial t} = -\frac{\gamma}{\left(1+\lambda^2\right)}\left[\overrightarrow{S}_i \times \overrightarrow{H}_i + \lambda \overrightarrow{S}_i \times \left(\overrightarrow{S}_i \times \overrightarrow{H}_i\right)\right] \tag{1.35}$$

Where the effective field $\overrightarrow{H}_i$ is derived from :

$$\overrightarrow{H}_i = -\frac{1}{\mu_0}\frac{\partial H}{\partial \overrightarrow{S}_i} \tag{1.36}$$

The spin Hamiltonian $H = -\int_{i\neq j} J_{ij}\overrightarrow{S}_i \cdot \overrightarrow{S}_i - K_{eff}\int_i \left(\overrightarrow{S}_i \cdot \overrightarrow{e}\right)^2 - \int_i \mu_0 \overrightarrow{S}_i \cdot \overrightarrow{H}_{ext}$, where the first term describes the spin exchange interaction, the second and third terms represent the effective anisotropy energy and Zeeman energy respectively.

However, LLG equation cannot be directly used to describe the laser induced spin dynamics because it does not consider the thermal effect by laser excitation. To solve this problem, a way is to introduce Langevin dynamics based on an approach developed by Brown[52], which is to add thermal fluctuation to each atom. The thermal fluctuation

$\Gamma(t)$ is a Gaussian distribution with the white-noise characteristics, hence, based on LLG equation, a thermal-effect field H_{th} is added to the effective field[52] :

$$H_{th} = \Gamma(t)\sqrt{\frac{2\lambda k_B T}{\gamma \mu_s \Delta t}} \tag{1.37}$$

Where k_B is the Boltzmann constant, μ_s is the atomics magnetic moment and Δt is the integration time for each atom. And T is the most important parameter whose value equals to the electron temperature T_e calculated from electron-phonon two temperature model :

$$C_e \frac{\partial T_e}{\partial t} = -G_{ep}\left(T_e - T_p\right) + S(t) \tag{1.38}$$

$$C_p \frac{\partial T_p}{\partial t} = -G_{ep}\left(T_p - T_e\right) \tag{1.39}$$

Therefore, by iterating over each atom and averaging all the atoms using LLG equation considering thermal-effect field, the revolution of magnetization over time can be obtained. This model has been widely used to simulate and analysis the process of laser-induced spin dynamics.

Micro three temperature model (M3TM)

Similar to phenomenological 3TM, the M3TM, proposed by Koopmans *et al.*[53–55], also considers the system as three thermal baths : electron, phonon, spin. The difference is that M3TM considers not only the energy transfer between the three thermal baths, but the angular moment dissipation during the process. This model allows researchers to understand the physical mechanism of ultrafast demagnetization from a microscopic perspective, especially from the perspective of electron scattering. The M3TM model suggests that the ultrafast demagnetization is mediated by Elliott-Yafet-like scattering mechanism[56]. In this mechanism, the spin-mixing of electronic state due to spin-orbit coupling is very important, the spin would flip during the electron-phonon momentum scattering events because of the mix state. The M3TM model describes the ultrafast demagnetization as :

$$\gamma T_e \frac{dT_e}{dt} = \nabla_z(\kappa \nabla_z T_e) + G_{ep}(T_p - T_e) \tag{1.40}$$

$$C_p \frac{dT_p}{dt} = G_{ep}(T_e - T_p) \tag{1.41}$$

$$\frac{dm}{dt} = Rm\frac{T_p}{T_c}(1 - m\ \coth(\frac{mT_c}{T_e})) \tag{1.42}$$

Where T_e, T_p and m are electron temperature, phonon temperature and magnetization in z direction respectively, κ is the thermal conductivity of electrons. R describes the demagnetizing speed of material system, its dependence on relevant magnetic parameter is given by $R \propto a_{sf} T_C^2/\mu_s$, where a_{sf} is the spin-flip probability. M3TM is able to explain the two-step demagnetization phenomenon by the huge difference of T_C/μ_s in different materials[57]. For instance, Gd is a typical material that shows two-step demagnetization, its atomic magnetic moment and Curie temperature T_C are $\mu_s = 7.55\ \mu_B$, $T_C = 297$ K respectively, the value of T_C/μ_s is 1/25 to that in Ni. Therefore, the large magnetic moment and low T_C yielded a lower demagnetization rate for Gd.

1.3 AO-HIS in ferrimagnetic materials

In the first section of this chapter, we introduced the discovery of two phenomena of AOS, in the following two sections we will discuss about AO-HIS and AO-HDS in more depth. We will first introduce some recent progress in the material systems, spin dynamics and mechanisms in AO-HIS in this section, because AO-HDS is a relatively more complicate phenomenon involving different timescales and helicity of light.

1.3.1 Mechanism of AO-HIS in RE-TM system

As we already known, the first observation of AO-HIS was demonstrated in GdFeCo alloy[9], which is an amorphous RE-TM ferrimagnet, the magnetization of RE and TM sublattice are opposite to each other in out-of-plane direction. The net magnetization of RE-TM can be adjusted over a wide range by changing the temperature or the concentration of elements, at a certain temperature or concentration, the magnetizations of two sublattices can be perfectly compensated and shows zero net magnetization, then this temperature or concentration is called compensation temperature T_M or compensation point x_{comp}.

Based on the demonstration of toggle switching using ultrashort hot-electrons pulse[28] and current pulse[29], the pure thermal origin of AO-HIS is now well accepted and the temperature evolutions of electrons and phonons have to be studied. The energy transfer between photons, electrons and phonons can be calculated by 3TM accompanies with angular momentum transfer, which is considered to be important to lead the switching. Because of conservation of angular momentum and the negligible dissipation of angular momentum to the electromagnetic field, the source of such angular momentum must come from the material itself. Thence AO-HIS is only expected to be exhibited in materials with two antiferromagnetic coupled sublattices, after the first observation in GdFeCo, various Gd-based RE-TM materials are reported to exhibit AO-HIS, such as GdCo alloy[17–19], Gd/Co multilayers[20;21], GdTbCo alloy[24]. But we have reason to believe all these materials share identical mechanism, considering their similar magnetic properties, switching behavior and ultrafast dynamics.

Radu *et al.* used a technique called X-ray magnetic circular dichroism (XMCD) measured the dynamics of two sublattices in GdFeCo film[9], the results provided an important idea for the mechanism study of AO-HIS. As shown in figure 1.9, two sublattices shows

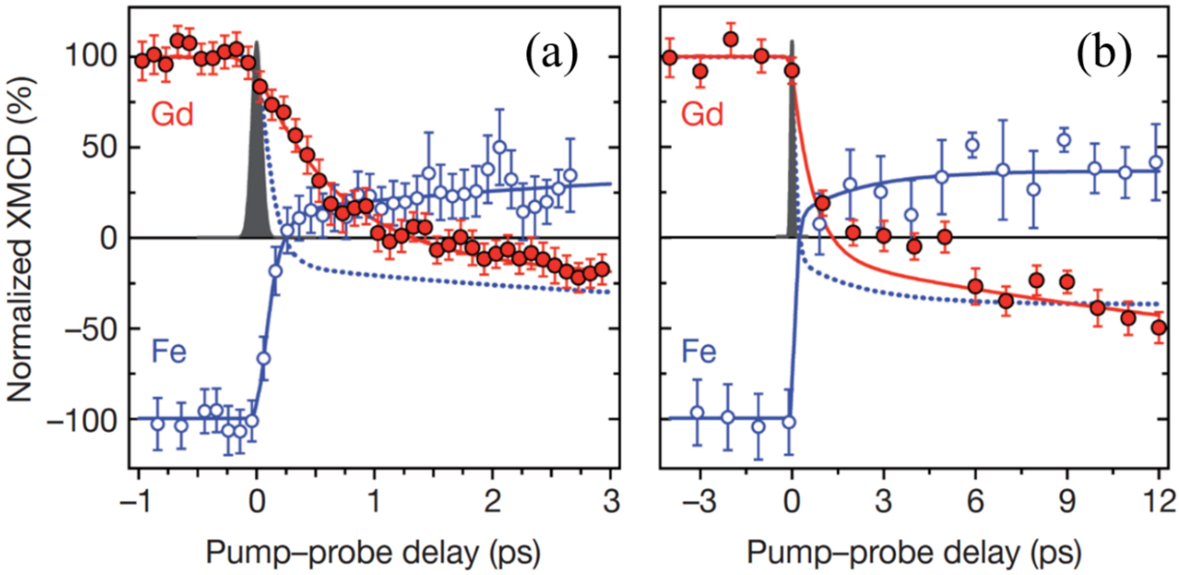

FIGURE 1.9 – Element-resolved spin dynamics of Fe and Gd magnetic moments by time-resolved XMCD in (a) the first 3 ps and (b) 12 ps. The solid lines are fit according to a double exponential function, the dashed lines depict the spin dynamics of Fe sublattice taken with the opposite sign.[9]

distinct dynamics, indeed, the TM moment is quenched in 300 fs, whereas the demagnetization of Gd is much slower and takes about 1.5 ps. Thereafter, their respective magnetic moment is rebuilt in the opposite direction in 12 ps. A transient ferromagnetic-like state appears at approximately 1 ps as a consequence of the difference in reversal time. The different demagnetization rate was originally understood from M3TM as we introduced in previous section[55], where the large magnetic moment and low T_C leads to a low demagnetization rate in Gd.

Mentink *et al.* developed a model to explain the magnetization reversal by considering the spin angular momentum flow[58], the generated angular momentum $\frac{dS_i}{dt}$ in two sublattice due to ultrafast demagnetization are described as :

$$\frac{dS_1}{dt} = \lambda_e (H_1 - H_2) + \lambda_1 H_1 \tag{1.43}$$

$$\frac{dS_2}{dt} = \lambda_e (H_2 - H_1) + \lambda_2 H_2 \tag{1.44}$$

Where the first term on the right side represents the angular momentum transfer between sublattices through the coupling strength λ_e due to the exchange scattering of electron spins, and the second term is the angular momentum that transfers to the environment, λ_1 and λ_2 describe the coupling strength between each sublattice and its environment, they can be described by the longitudinal relaxation time in the Bloch equation :

$$\lambda_i \propto \frac{\gamma_i \alpha_i k_B T}{\mu_i} \tag{1.45}$$

H_1 and H_2 are the effective magnetic fields $H_i = -\delta W/\delta S_i$ which are derived from the magnetic energy W, and there is :

$$W = \int dr \left[f_1 \left(S_1^2 \right) + f_2 \left(S_2^2 \right) + f_1 \left(S_1 S_2 \right) \right] \tag{1.46}$$

$f_\mathrm{i} \left(S_\mathrm{i}^2 \right)$ describes the exchange energy responsible for the formation of macroscopic magnetic moment in each sublattice, and the third term describes the exchange interaction of two sublattices. In this case, a larger damping parameter and smaller magnetic moment in TM leads to a larger λ_i, which is the strength of coupling to the environment, and that explains why the demagnetization rate of TM is much faster than that of Gd. The significant difference of demagnetization rate for Gd and TM and the angular momentum transfer between the two are essential for AO-HIS. This theoretical framework has been used to explain the spin dynamics methods for GdFeCo and MnRuGa alloys[59;60]. Based on the theory of demagnetization rate, the magnetization dynamics of AO-HIS are well reproduced with atomistic spin dynamics model[10] in a wide range of pulse duration and alloy composition[61].

1.3.2 Spin-valves

Another pathway to exhibit or to study AO-HIS is the ultrafast spin-transport in metallic multilayers. It has been theoretically predicted that ultrafast demagnetization is caused by spin-polarized excited electron diffusion in the superdiffusive regime[62] and the spin angular momentum will be transferred from ferromagnetic layer to a nonmagnetic layer in metallic films.

Melnikov *et al.* experimentally observed this phenomenon in Fe/Au multilayers firstly[63]. In this work, after the Fe layer was irradiated by a 35-fs laser pulse, the spin accumulation signal in Au layer can be detected. The spin accumulation dynamics in Au layer is shown in figure 1.10 (a-b). Later, Choi *et al.* designed a clever experiment as shown in figure 1.10 (c)[64], they deposited a multilayered structure of Pt/FM1/Cu/FM2, where FM1 and FM2 are two ferromagnetic layers whose easy axis are orthogonal to each other. The laser pulse excites the Pt layer and leads the demagnetization of FM1, then the spin accumulation in Cu layer and spin transfer torque in FM2 has been detected. This result proves the present of spin-current generation due to ultrafast demagnetization. Based on this, many works have shown the ultrafast demagnetization dynamics due to the angular momentum transfer in spin-valves[53;65], which is a structure consisting two collinear ferromagnetic layers separated by a nonmagnetic metal layer[66], as well as in similar structure of two noncollinear ferromagnetic layers[64;67;68].

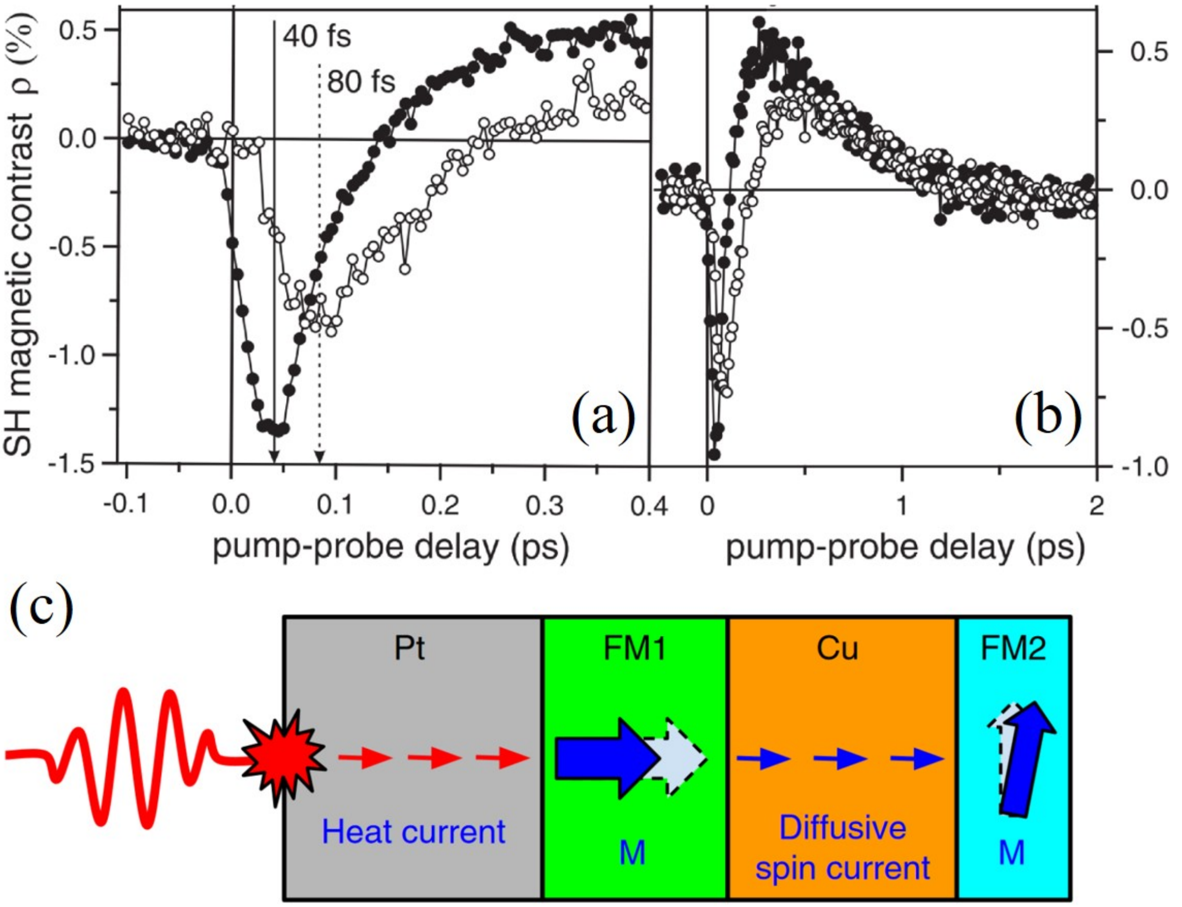

FIGURE 1.10 – Spin accumulation dynamics of Au layer in Fe/Au bilayer in (a) the first 0.5 ps and (b) 2 ps, results detected by second harmonic probe after the Fe layer was irradiated by a 35-fs laser pulse. (c) Schematic illustration of spin current generated by thermally driven ultrafast demagnetization, the laser pulse excites the Pt layer and leads the demagnetization of FM1, then the spin accumulation in Cu layer and spin transfer torque in FM2 have been detected.[63;64]

It is nature that researchers start attempting to utilizer such spin current leads from ultrafast demagnetization to realize the magnetization reversal. In 2018, Iihama *et al.* firstly demonstrated a switching of a ferromagnetic Co/Pt layer with a polarized electron pulse in a GdFeCo/Cu/[Co/Pt] spin-valve[69]. The spin current generated from the demagnetization of GdFeCo layer then injects to the Cu layer and switches Co/Pt layer, as shown in figure 1.11, the magnetization of Co/Pt layer can be manipulated by changing the amount of generated spin current from various laser fluence. Two subsequent studies[70;71] confirmed the suggested switching mechanism for ferromagnets and predicted that the phenomenon is very general and can be observed for a large variety of magnetic multilayers. Recently, Junta *et al.* have realized AO-HIS in various of FM1/Cu/FM2 spin-valve structure in which Gd is absent[72].

These demonstrations of AO-HIS in spin-valves offer a new idea of magnetization

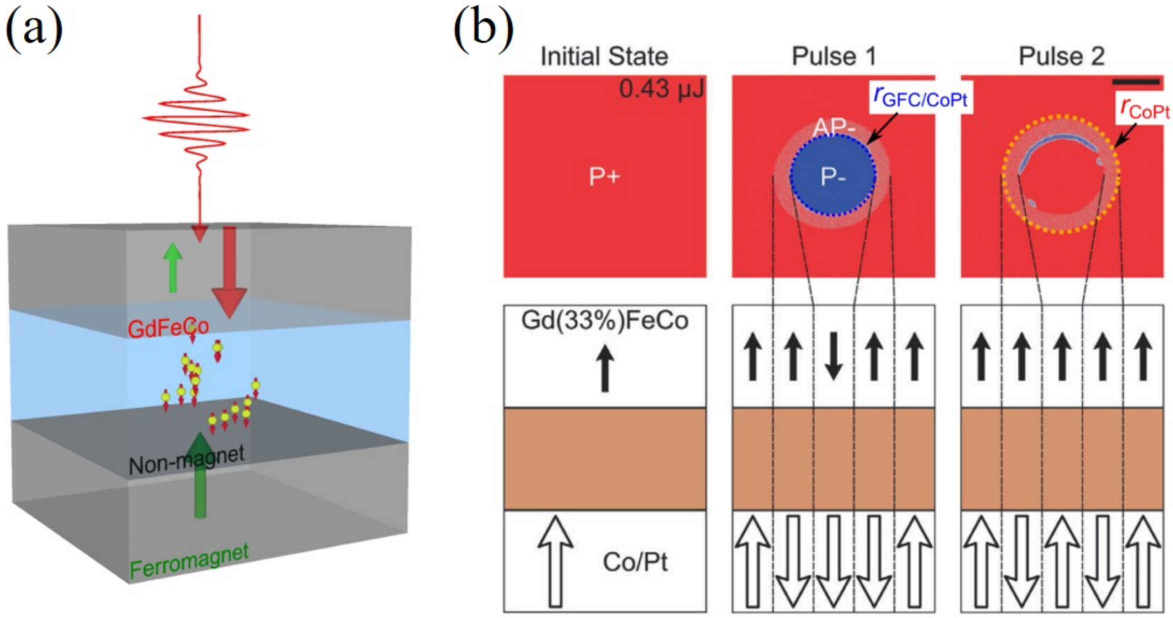

FIGURE 1.11 – (a) Schematic illustration of spintransport mediated AOS in a GdFeCo/non-magnet/ferromagnet spin-valve. (b) The magnetic states after irradiation of two fs laser pulses in a Gd-rich spin-valve, the magnetization of Co/Pt layer can be manipulated by changing the amount of generated spin current from various laser fluence.[71]

manipulation by light, it also helps to understand the physics of traditional AO-HIS in GdFeCo alloy even if they may have different mechanisms. Besides, it provides a way to engineer ferromagnetic materials for AO-HIS and avoid the disadvantages, such as the limitation of pulse duration and power consumption, that Gd-based materials have.

1.3.3 Opto-spintronics for applications

Despite the debates on the mechanism or novel materials of AO-HIS, the technology of optical magnetization manipulation has its advantages when applied to a magnetic device, such as its robustness, fast speed and reproducibility. Recently, many attempts to implement AOS materials into a magnetic device and to study the speed, dissipation and scalability of the device have been reported.

A popular method of application is integrating AOS material, particularly GdFeCo, into a magnetic tunnel junction (MTJ)[73–75]. MTJ is the storage unit of a magnetic memory device, it includes a magnetic free layer, a tunnelling layer and a magnetic fixed layer. When the two magnetic layers are parallelly (P) aligned, the tunnelling magnetoresistance (TMR) is at low level ; when they are anti-parallelly (AP) aligned, the TMR is at high level. The TMR ratio which defined by $(\mathrm{TMR}_{\mathrm{AP}}-\mathrm{TMR}_{\mathrm{P}})/\mathrm{TMR}_{\mathrm{P}}$ is a key parameter to describe the performance of an MTJ. The writing operation of an MTJ can be realized by injecting current pulse in different perpendicular direction to switch the free layer based on spin transfer torque, while the read-out operation can be achieved by measuring

TMR. Replacing the free layer as AOS material to enable the optical operation to a MTJ is then demonstrated by Chen *et al.*[73]. In this work, they designed an optically switchable MTJ using GdFeCo as the free layer with a TMR ratio of 0.6%, the switching can be achieved under a repetition rate of MHz level, and they suggested that the fundamental upper limit should be higher than tens of GHz. However, such structure limits the TMR ratio due to the low degree of spin polarization of GdFeCo layer. To increase the TMR ratio of opto-MTJ, Wang *et al.* coupled the AOS free layer with another CoFeB layer and developed the TMR ratio to 34.7%[74]. Interestingly, the first observation of AO-HIS in Tb/Co multilayers was initially for the designing of MTJ[15]. They use Tb/Co multilayers as the free layer to obtain a high TMR ratio and unexpectedly discovered that Tb/Co multilayers can be switched with single laser pulse.

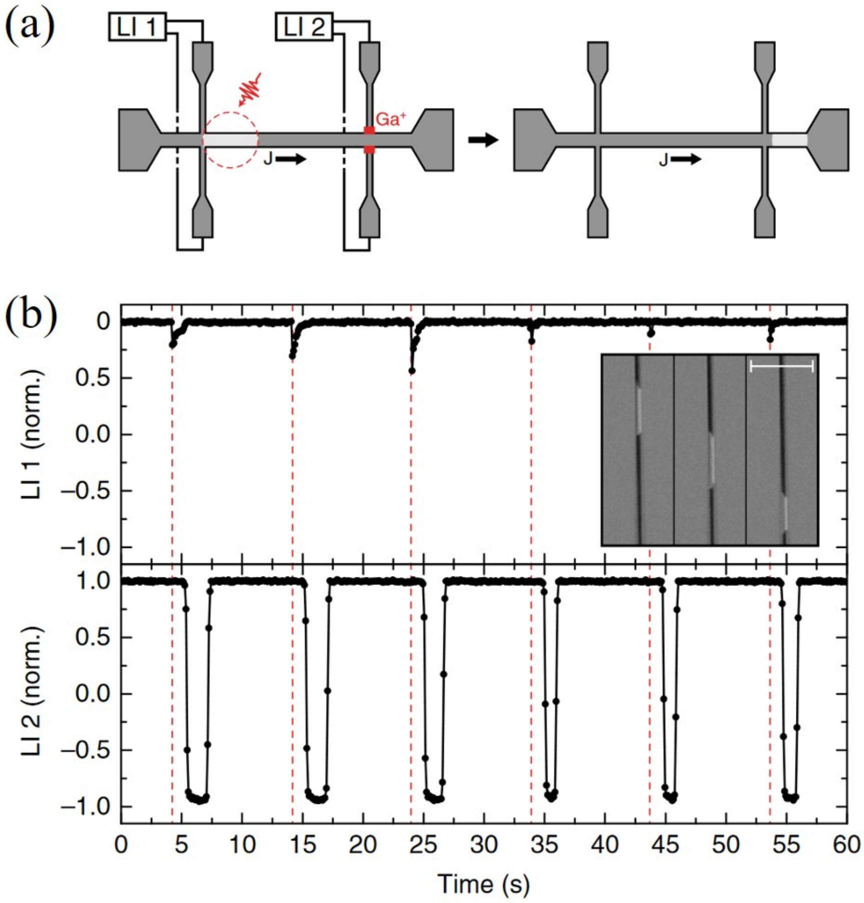

FIGURE 1.12 – The combination of AO-HIS and racetrack memory. (a) the schematic illustration of the concept, the data is write-in by laser pulse in knot LI 1, then the current push the DW to LI 2 and the information is read-out by measuring the anomalous Hall voltage at LI 2. (b) the voltage read out from LI 1 and LI2 when sending a periodic pulse train and injecting a DC current.[76]

Another path for opto-magnetic device is the combination of AO-HIS and racetrack memory. A racetrack memory uses a spin-coherent electric current to move the magnetic domain along the nanowire, which is very similar to the idea of a magnetic tape. Lalieu *et al.* fabricated a Pt/Co/Gd racetrack[76], the material can be optically write-in and the DW can be moved by electrical current. As shown in figure 1.12, the data is written in by laser pulse in knot LI 1, then the current pushes the DW to LI 2 and the information can be read out by measuring the anomalous Hall resistance at LI 2. This work paves the way towards integrated photonic memory devices, some subsequent works have been done to develop the performance of opto-racetrack memory, such as increasing the DW velocity of AOS material[77], optimizing the energy efficiency of devices[78–80].

So far, the application of AO-HIS into storage devices still faces lots of challenges. Limited by the scalability of the laser source and beam size, its integration in a large array with high density and random access for write-in and read-out would be very difficult, it is unlikely that opto-magnetic devices (either the opto-MTJ or the opto-racetrack memory) can reach the same level of data density as other memory technologies do. There is still a long way to go for researchers to consider the proper application of opto-magnetic recording or other unexpected fields.

1.4 AO-HDS in ferromagnetic materials

The behavior and material system of AO-HDS are quite different from that of AO-HIS, thus as well as its mechanism, because it evolves under high non-equilibrium conditions due to the action of many different processes act on different length- and time-scales and are subjects of intensive debates, the complexity of AO-HDS has frustrated the development of a unified predictive theory and continues to challenge our understanding of opto-magnetic matter interactions and of the resulting relaxation dynamics. However less research has been carried out recent years due to its less promising application prospect compared to AO-HIS, even though it was discovered earlier than the lateral. But studying its mechanism helps to understand the physics of opto-magnetic interactions and pave the way for the possible demonstration of single-shot AO-HDS.

The origin of AO-HDS is now mainly explained by two effects : inverse Faraday effect (IFE), in which a circularly polarized pulse can generate a magnetic field following its wave vector, and magnetic circular dichroism (MCD) which describes the absorption difference of a magnetization orientation from light with various helicities. Besides, another recently discovered effect, namely the magnetization induced by light absorption (MILA), also contribute in the generation of AO-HDS. In this section, the material systems and recent progress of AO-HDS will be introduced firstly, then we will focus on its two origins and discuss the way they control the magnetization respectively.

1.4.1 AO-HDS in vast materials

The first observation and early studies of AO-HDS are based on RE-TM systems. An extensive collection of its switching behavior in RE-TM system is shown in figure 1.13, where a large range of RE-TM alloys (with RE = Gd, Tb, Dy, Ho and TM = Fe, Co) and multilayers (with RE = Tb, Ho and TM = Co) with various magnetic properties by changing the elements composition is investigated. For RE-TM alloys with PMA, AO-HDS can only be observed in TM-rich samples from the work of Mangin *et al.*[26], but it still remains debates on relationship of compensation temperature and switching behavior because some other works show that RE-rich alloys exhibit AO-HDS as well[31;81;82]. For multilayer systems, not only the composition range for maintaining PMA is enlarged, but the range for showing AO-HDS, including some RE-rich multilayers which are not very far away from its compensation point. These results show that the atomic ordering or the exchange coupling between RE and TM sublattices plays an important role on the observation of AO-HDS, but the physics leads to such behavior is complex and multi-causal, it would origin from the first step which is the ultrafast demagnetization of the whole process, for instance, it has been demonstrated that the ultrafast demagnetization can be quite different between FeNi alloy[83] and Fe/Ni multilayers[65].

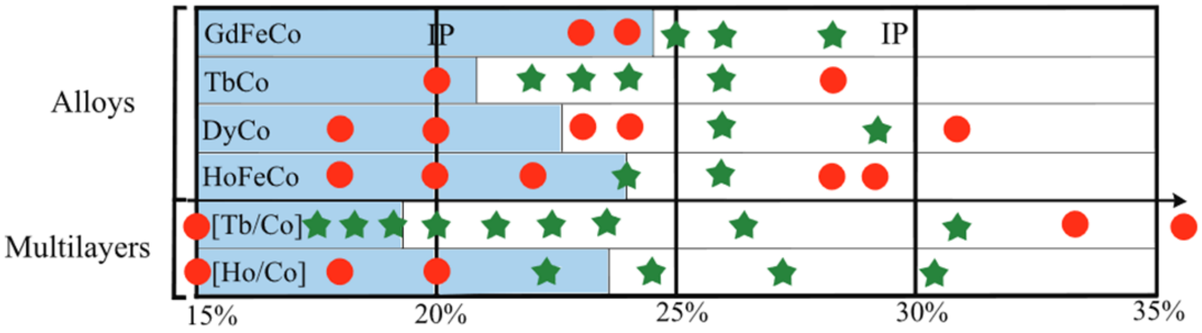

FIGURE 1.13 – A conclusion of the RE-TM materials that exhibit AO-HDS, those samples with AO-HDS are indicated by green stars, otherwise by red dots. All the alloys show PMA except two GdFeCo alloys marked IP (for in-plane anisotropy), the shaded regions correspond to TM-rich materials.[26]

Afterwards, The breakthrough discovery of AO-HDS in Co/Pt ferromagnetic material largely excited the researching interest because these materials usually exhibit strong PMA, which is helpful for high-density magnetic recording. Thence, after the conclusion of AO-HDS in RE-TM ferrimagnetic systems from Mangin *et al.*[26] and in ferromagnetic multilayer systems from Lambert *et al.*[32], the exploration towards its material system is almost accomplished because this phenomenon appears in most of the materials with PMA. Therefore, recent researchers shift their focus on the magnetic properties of the sample on the switching behavior.

Lambert *et al.* also noticed that the anisotropy plays a significant role in exhibiting

AO-HDS[32]. They grew a series of [Co(0.4 nm)/Pt(0.7 nm)]$_N$ multilayers with N = 3, 5, 8, in this case the anisotropy is enhanced with more repetition layers theoretically. However, only thermal demagnetization is observed for samples with N = 5, 8 which have stronger anisotropy, samples with less repetition show better switching behavior. Similar result is shown by El Hadri *et al.* in figure 1.14(a)[81]. In order to study how the magnetic properties, such as anisotropy, Curie temperature, saturation magnetization, impact the behavior of switching, El Hadri *et al.* designed an experiment to give some clue[84], they studied the effect of He$^+$-ion irradiation on the AO-HDS ability, the irradiation process on the Co/Pt multilayers induces intermixing at the interface, which leads to a significant decrease of the interfacial anisotropy[85;86]. By changing the dose of irradiation, the PMA in the samples can be controlled, a behavior change from AO-HDS to thermal demagnetization for various irradiation dose is demonstrated in figure 1.14 (b). The as-deposit samples show typical AO-HDS behavior, whereas samples with irradiation gradually lost their switching property as the irradiation dose increases. Such result shows sample with weaker anisotropy is less possible to shows AO-HDS. However, such conclusion is opposite to previous results from Co/Pt with various layer repetition. Therefore, it seems anisotropy may not be the criterion, or at least the only criterion, for the observation of AO-HDS.

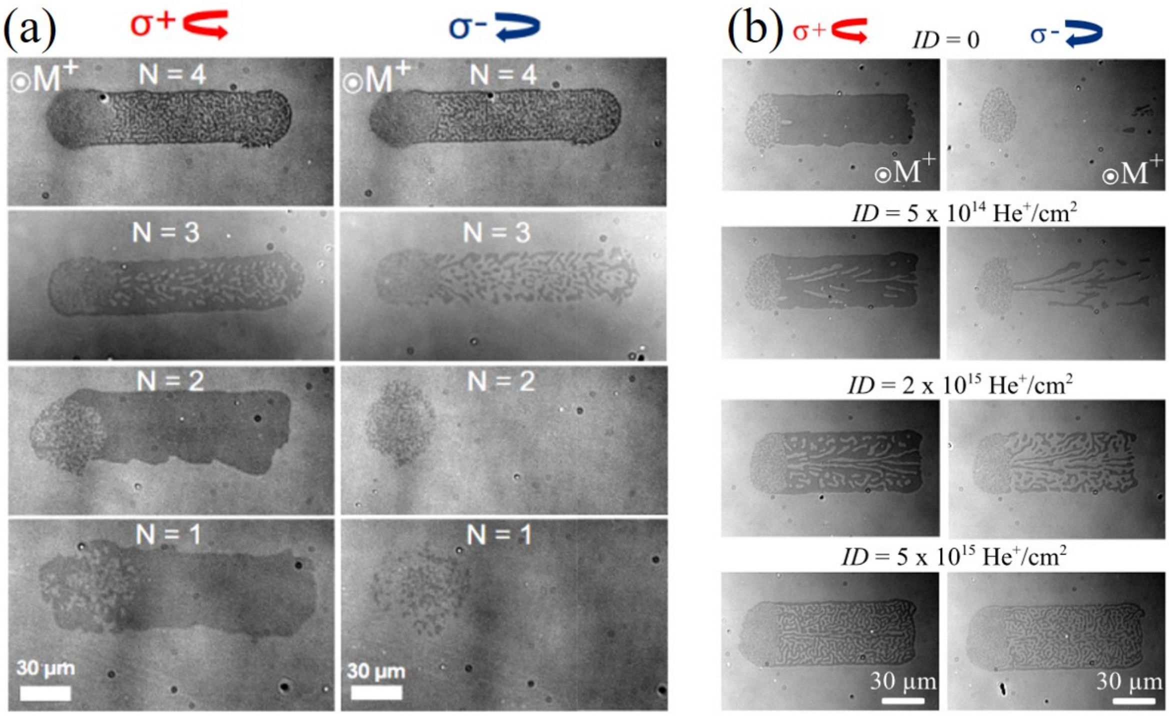

FIGURE 1.14 – The effects of magnetic properties on the behavior of AO-HDS in Co/Pt multilayers. (a) magnetic states of [Co/Pt]$_N$ samples with different layer repetition after swept by circularly polarized pulse train. (b) magnetic states after swept by circularly polarized pulse train for Co/Pt samples after He$^+$-ion irradiation of various processing dose.[81;84]

Some publications proposed that the domain size is an important criterion in exhibiting AO-HDS[81;84], the equilibrium size of magnetic domains that forms during the cooling process after the pulse should be larger than the laser spot size. The evolution of domain size in samples with various Co thickness, layer repetition and magnetic anisotropy is shown in figure 1.15, those samples with smaller domain size than the spot size is indeed more possible to show AO-HDS property, otherwise, the samples will tend to break into multi-domains after the laser exposure. Later, Vomir *et al.* demonstrated surprising single-shot AO-HIS in Co/Pt multilayers by using a highly focused laser beam spot of a 0.8 μm-size, which is far smaller than the domain size of the sample[87]. But no subsequent result has been reported to explain the mechanism of such phenomenon and if the order of domain size and spot size is important remains unknown.

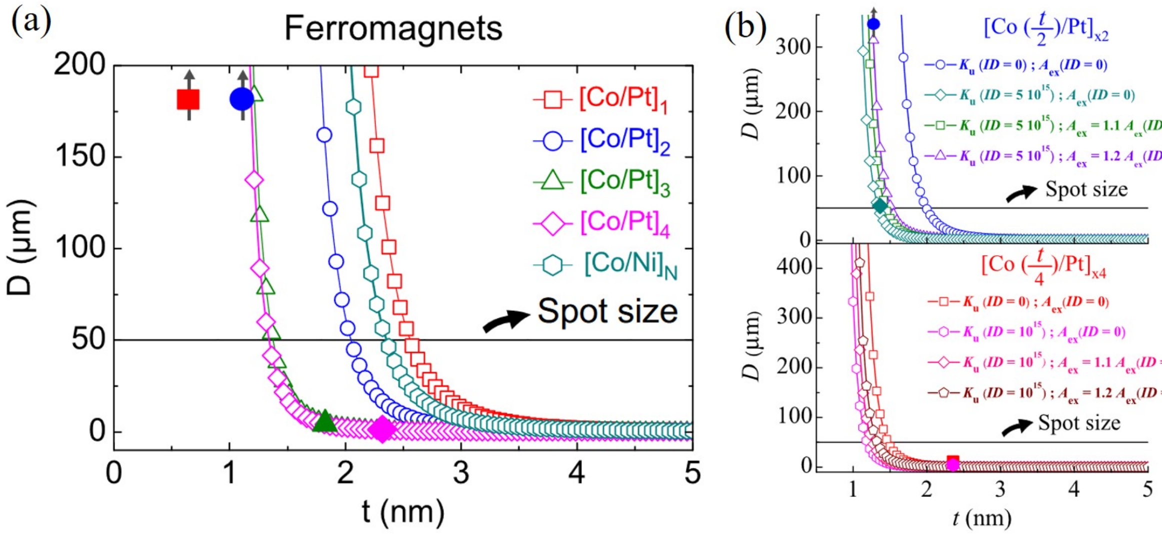

FIGURE 1.15 – Estimation of the domain size as a function of the Co thickness in Co/Pt multilayers with (a) various layer repetition and (b) various anisotropy constant K_u controlled by He$^+$-ion irradiation dose. It has been suggested that samples with smaller domain size than the spot size is more likely to show AO-HDS property.[81;84]

Cheng *et al.* suggested that AO-HDS process is closely related to the competition between the opto-thermal and opto-magnetic effects of the laser pulses[88]. Therefore, they designed a hybrid metal-ferromagnet film, which consist of Co/Pt multilayers with PMA and an Au capping layer on top. The Au layer facilitates AO-HDS in the following two aspects : first, it works as a heat sink and cools down the magnetic film to decrease the thermal effect of the pulse ; second, it prolongs the lifetime of IFE field induced by pulse to enhance the opto-magnetic effect, an opto-magnetic coupling method was employed to explain the physics of such effect[89]. As shown in figure 1.16, the hybrid metal-ferromagnet film shows more pronounced AO-HDS in comparison with bare Co/Pt multilayers. Such mechanism seems to emphasize the role of IFE but regards the thermal effect induced by MCD as negative to AO-HDS, whereas both two effects should be beneficial in establishing aligned magnetization with light helicity. Nevertheless, with the addition of Au top layer, the hybrid metal-ferromagnet material indeed demonstrates clear advantages and pronounced AO-HDS, which could potentially broaden the application of AO-HDS.

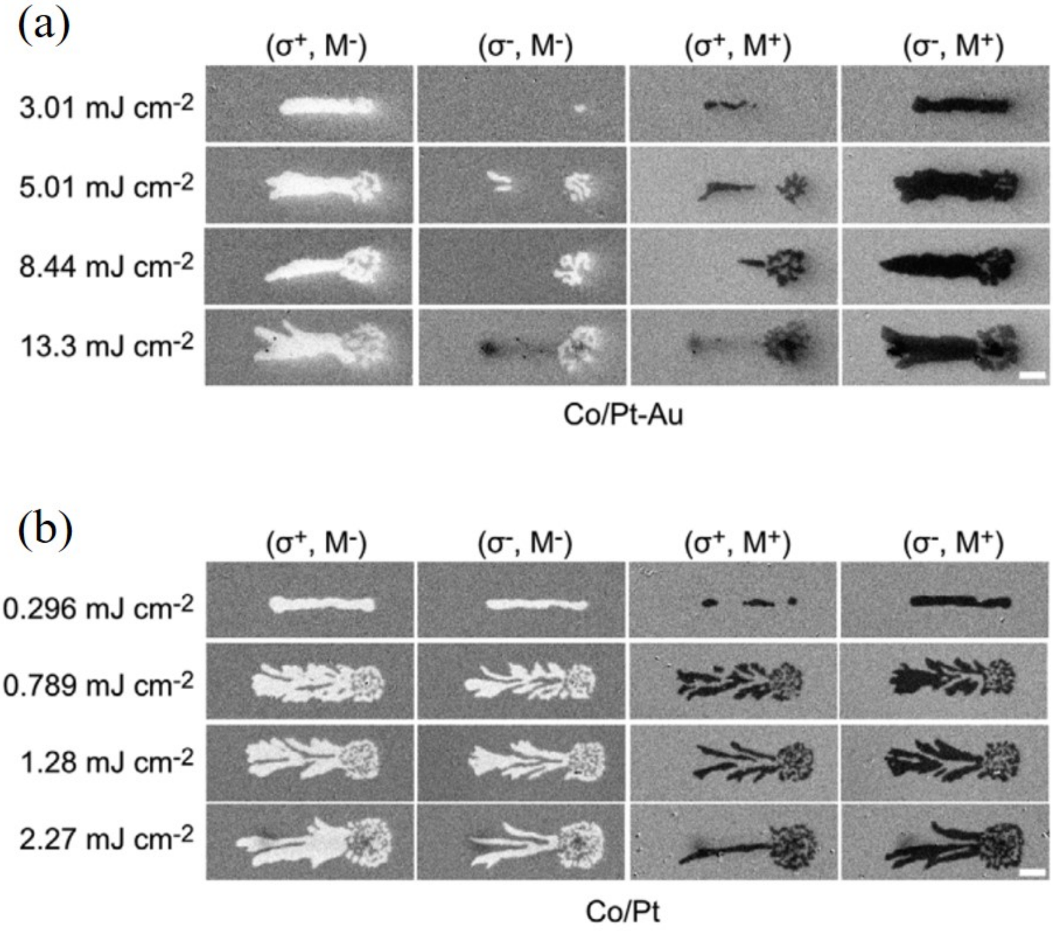

FIGURE 1.16 – The AO-HDS behavior in (a) hybrid Co/Pt-Au samples and (b) bare Co/Pt samples under various laser fluence and light helicities. The hybrid metal-ferromagnet films show pronounced AO-HDS, because the Au layer not only functions as a heat sink but also prolongs the IFE field to longer timescale.[88]

So far, even though numerous materials have been reported to exhibit AO-HDS, its mechanism behind the simplest Co/Pt multilayers is still not conclusive. In the following, three main possible origins : IFE, MCD and the recently introduced effect of magnetization induced by light absorption (MILA) will be introduced, as well as the current explanations on how they impact the magnetization.

1.4.2 Inverse Faraday effect

Michael Faraday discovered the first interaction between light and electromagnetism which is then called Faraday effect[90]. The Faraday effect causes a rotation of the plane of polarization and the rotation is linearly proportional to the component of magnetic field in the direction of light wave propagation. Reciprocally, it was suggested that circularly-polarized light might induce a magnetic polarization, this phenomenon is called inverse Faraday effect (IFE). IFE was firstly predicted by van der Ziel *et al.* in 1965[91], they observed that circularly polarized light can induce magnetization in Eu^{2+}-doped CaF_2 diamagnetic glasses, and even in non-absorbing materials such as organic or inorganic liquids. In transparent and non-magnetic mediums, a phenomenological relation to describe the effective field generated from a monochromatic electric field of light $E(\omega)$ is :

$$M = \chi^{MO}\left[E(\omega) \times E(\omega)^*\right] \tag{1.47}$$

Where χ^{MO} is the magneto-optical susceptibility and ω the electromagnetic wave frequency, it can be seen that left and right circularly polarized pulse can generate transient field with opposite direction along the light wave vector, a quantum-mechanical explanation of IFE is given in terms of an optically induced "effective Hamiltonian" by Pershan *et al.*[92]. However, it is necessary to emphasize that Eq. 1.47 is not the case in magnetized materials, the existence and magnitude of IFE in magnetic materials are still unclear.

The improvement of laser technique has shortened the laser pulse duration continuously, the ultrashort laser pulse greatly enhanced the magneto-optical effect in magnetically ordered materials. In 2005, Kimel *et al.* realized the possible laser-induced magnetization control with IFE field since this field can be very strong with ultrashort pulse[93], they demonstrated that one can non-thermally excite and coherently control spin oscillations in weak ferromagnet $DyFeO_3$ with circularly polarized femtosecond laser pulses, and such laser pulse whose energy is 500 mJ/cm^2 and duration is 200 fs is shown to be equivalent to a magnetic field up to 5 T with similar duration. Such theoretical base leads to the fist observation of AO-HDS in GdFeCo[8], it is now understandable why it was AO-HDS firstly discovered in GdFeCo rather than AO-HIS, even though both two effects exist in GdFeCo alloy. Later, some models have been built to explain the all-optical magnetization reversal by circularly polarized laser pulses[94;95].

By employing the M3TM that we introduced in last section and considering IFE as an effective field, the magnetization dynamics under the irradiation of circularly polarized pulse can be described as :

$$\frac{dm}{dt} = \frac{RT_p}{T_c}\left[M + b_{eff}\right]\left(1 - m\coth\left(\frac{T_c}{T_e}\left[m + b_{eff}\right]\right)\right) \tag{1.48}$$

Where b_{eff} is the IFE induced effective field normalized to the exchange field. based on this, Cornelissen *et al.* calculated the switching dynamics in ferromagnets[95]. The simulation result shows the magnetization as a function of time after laser excitation is shown in figure 1.17, the circularly polarized pulses are assumed to induce a magnetic field pulse with a magnitude of 20 T and a lifetime of 0.4 ps, while the linearly polarized L pulse is assumed to induce zero magnetic field. For linearly polarized L or right circularly polarized σ^+ pulse, an ultrafast magnetization quenching followed by a relaxation beck to initial state is observed, and the speed of relaxation with σ^+ pulse is faster than with L pulse. For left circularly polarized σ^- pulse, a switching is realized by an ultrafast magnetization quenching and a remagnetization towards reversal direction. A phase diagram of the final magnetic states after laser pulse excitation with given fluence and pulse duration is shown in figure 1.17 (b), the fluence window is enlarged with increasing the pulse duration. It can also be seen that a lifetime of at least 0.15 ps is necessary to obtain a switching in the case where the IFE field is in the range of 10 T to 24 T.

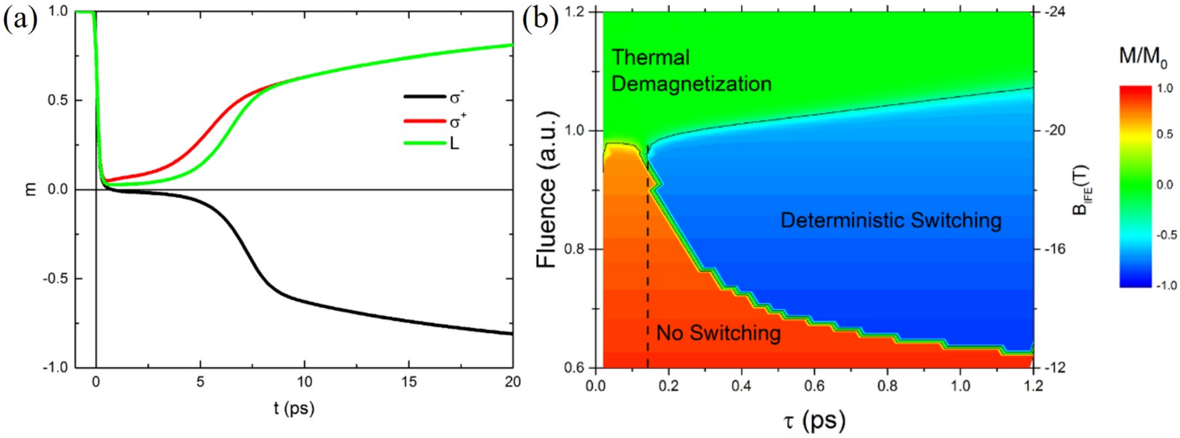

FIGURE 1.17 – (a) The calculated magnetization as a function of time after laser excitation of three helicities using M3TM. (b) The phase diagram of the final magnetic states after laser pulse excitation with given fluence and pulse duration.[95]

Although such model works very well in reproducing the experimental observation, there has been many questions to be answered if such effect is the origin of AO-HDS. Firstly, the dynamics of such IFE induced reversal remains unclear, both the full switching accomplished by the spin flip of the many cells in picosecond timescale or the IFE field driven DW motion in longer timescale are possible. Secondly, the lifetime of the IFE field needs to be quantitatively described or experimentally measured since it is a critical parameter to generate a switching. Lastly, the single-shot AO-HDS should be possible based on the mechanism of IFE, however no such experimental result has been reported in ferromagnetic materials.

1.4.3 Magnetic circular dichroism

Magnetic circular dichroism (MCD) is the difference of absorption between left (A_L) or right (A_R) circularly polarized light for a longitudinal magnetized material. The effect of MCD mainly contributes to the temperature difference of a magnetic system and it is the subsequent effects from the temperature difference that generate the switching. Under the irradiation of a circularly polarized laser pulse, the magnetic domains with different spin orientations will rise up to different temperatures, then leads to many subsequent asymmetric behaviors, such as different anisotropy, stability or spin dynamics of two domains. There have been some discussions about possible lateral effects that immediately drive the switching.

Gorchon *et al.* considered the magnetic stability and the stochastic spin flip as the possible direct reason of AO-HDS[80]. They built a simple and intuitive model to describe the switching : the opposite domains will rise to different temperature T_{hot} and T_{cold} after the irradiation to circularly polarized pulse. The temperature difference leads to different magnetic stability, when T_{hot} reaches a certain threshold and hot domains will be prone to stochastic switching, whereas the cold domains remain stable. Thence the full switching is accomplished by repeating this process multiple times. In this model, the magnetic system is represented as an array of macrospin cells with opposite out-of-plane magnetic state up (state a) and down (state b). The characteristic hopping time for magnetization reversal is given by Arrhenius-Néel law :

$$\tau_{ab}\left(T\right) = \tau_0 \exp\left(\frac{E_{ab}\left(T\right)}{k_B T}\right) \tag{1.49}$$

Where τ_0 is a characteristic time, E_{ab} is the energy barrier that need to overcome for a spin flip. By introducing a laser pulse to heat up the cell to $(T_0 + \Delta T)$ with a duration t_{hot}, the cell has a probability P to switch from state a to state b :

$$P = \frac{1}{2}\left[1 - \exp\left(-\frac{t_{hot}}{\tau\left(T_0 + \Delta T\right)}\right)\right] \tag{1.50}$$

And thus $(1 - P)$ to remain its initial state. Then take MCD into consideration by impacting the cell temperature :

$$T_{hot} = T_0 + \left(1 + \frac{MCD}{2}\right)\Delta T \tag{1.51}$$

$$T_{cold} = T_0 + \left(1 - \frac{MCD}{2}\right)\Delta T \tag{1.52}$$

After building the model consider the accumulative effect of multiple pulses, the numerical solution is calculated for an FePt-C-L1_0 granular film with a cell volume of 5×5×7 = 175 nm^2 and the MCD of 5.8%. The simulation result is shown in figure 1.18 (a), the AOS probability is calculated by countering the ratio of switching cells, $(T_0 + \Delta T)/T_C$ can be regarded as the laser fluence. For certain number of pulses, there is a certain fluence window that ensuring a maximum AOS probability around the system T_C. The AOS probability can be increased to 100% by increasing the pulse number, the threshold fluence is lowered for larger pulse number, and the AOS probability drops sharply after the system temperature is higher than T_C and ends up at 50% above a certain temperature threshold. In figure 1.18 (b), the spatial magnetization profile after exposed to static and sweeping laser beam is demonstrated, which is consistent to the experiment of Lambert *et al.* in FePt-C[32].

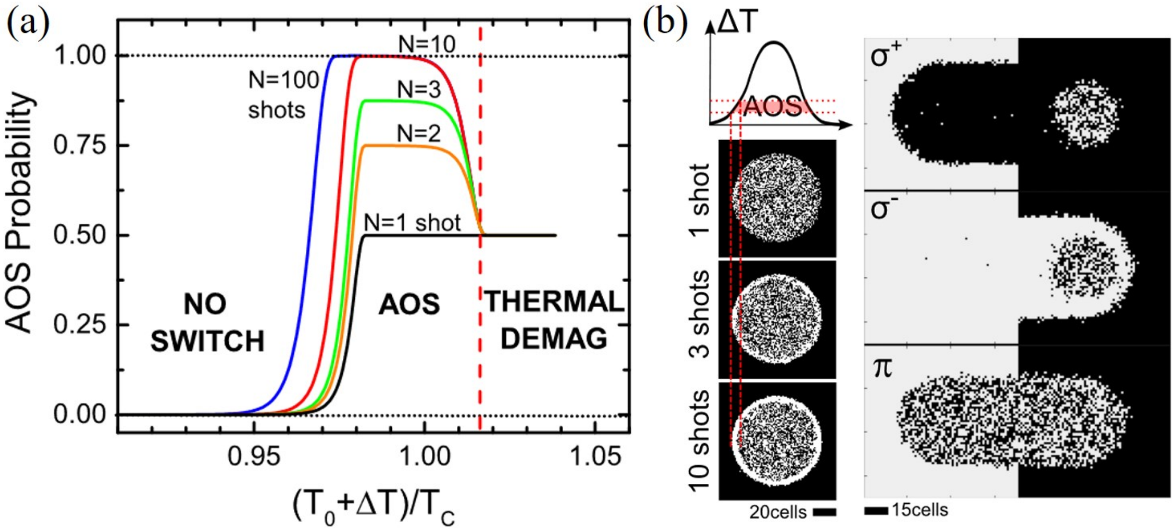

FIGURE 1.18 – (a). Switching probability as a function of the laser-elevate temperature Δt for different pulse number. (b) The calculated spatial magnetization profile after exposed to static and sweeping laser beam from the model of Gorchon er al.[80]

The model from Gorchon *et al.* demonstrated such pure thermal spin-flip mechanism due to MCD can generate a switching in a broad range of materials, and the MCD as small as 0.5% is sufficient for magnetization reversal but with very narrow fluence range. And based on this mechanism, some more simulation results which are in good agreement with experiment have been reported to show the impact of MCD[96–98].

Another possible mechanism related to MCD is all-optical helicity-dependent domain wall motion, initially proposed by Medapalli *et al.*[99]. They first observed that the DW can be manipulated using laser pulse with different helicity as shown in figure 1.19, when left circularly polarized σ^- laser pulse shine exactly on the DW, the DW will gradually move upwards, whereas the moving direction is reversed when shining a right circularly polarized σ^+ laser pulse train. From this phenomenon, they came up a mechanism based on the thermal gradients between areas with opposite magnetization orientation due to MCD. The absorption difference leads to a temperature gradient from low-absorbing domain to high-absorbing domain over a longer distance than the width of DW, and it has been theoretically proved[100–103] and experimentally observed[104–106] that the DW can be moved under thermal gradient arising from a magnonic spin Seebeck effect. Similarly, consider a multiple shots situation, after the magnetic system is nucleated into a multi-domain state by the first several pulses, the lateral pulses will gradually move the DWs and accomplish a full switching. Since this mechanism includes lots of effects concerning various timescale from laser absorption in picosecond timescale to DW motion in nanosecond timescale, no model has been established to well reproduce this assumption so far. But some lateral experimental results support and supplement this mechanism[106;107], in this thesis, we believe this is a higher likelihood origin of AO-HDS and it will be discussed in Chapter 3 in more depth.

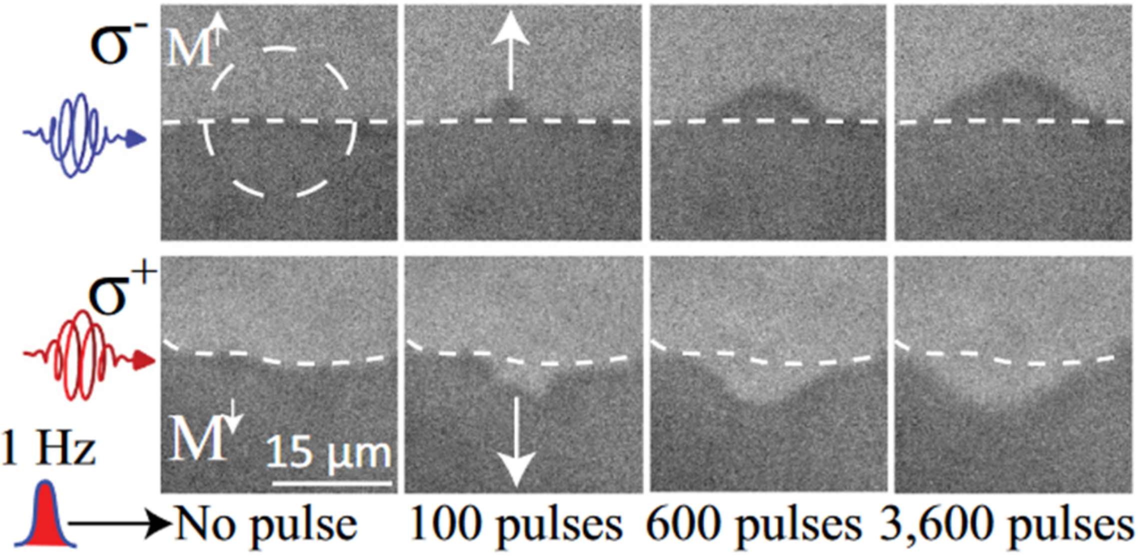

FIGURE 1.19 – The DW displacement operated by σ^- or σ^+ polarized consecutive pulse trains at a repetition rate of 1 Hz, a fluence of 0.4 mJ/cm^2 and a pulse duration of 4 ps. The direction of DW displacement can be controlled by the light helicity.[99]

However, over the years, even though both IFE and MCD have been numerically demonstrated that they can generated a switching, it has often argued which effect is the real or dominant origin of AO-HDS[107–109].

1.4.4 Magnetization induced by light absorption

Unlike MCD explain AO-HDS from the perspective of pure thermal absorption and its consequence of domain temperature, the magnetization induced by light absorption (MILA) is a purely optical effect and considers the angular momentum transferred from the light to the matter. Meanwhile, compares to IFE which is proportional to the intensity of the light and vanishes with the light pulse, in MILA effect, much like an absorbed energy, the induced atomic magnetic moment stays even after the light is gone.

MILA effect was recently proposed by Scheid *et al.*[110], the rate of transition between two Kohn-Sham eigenstates[111] : $|\psi_{n,\vec{k}}\rangle$ and $|\psi_{n',\vec{k}}\rangle$ induced by light-matter interaction Hamiltonian $\hat{W}$ can be computed using Fermi's golden rule :

$$\begin{aligned}\Gamma_{n\vec{k}\to n'\vec{k}} = \frac{2\pi}{\hbar}|\langle\, \psi_{n',\vec{k}}|\hat{W}|\psi_{n,\vec{k}}\rangle|^2 f_{n,\vec{k}}\left(1 - f_{n',\vec{k}}\right) \\ \times\left[\delta\left(\varepsilon_{n',\vec{k}} - \varepsilon_{n,\vec{k}} - \hbar\omega\right) + \delta\left(\varepsilon_{n',\vec{k}} - \varepsilon_{n,\vec{k}} + \hbar\omega\right)\right]\end{aligned} \tag{1.53}$$

Where, n is the band index and $\vec{k}$ is the vector of the first Brillouin zone, ω is the pulsation of light, $f_{n,\vec{k}}$ and $\varepsilon_{n,\vec{k}}$ are the occupation and energy of the orbital $\psi_{n,\vec{k}}$. The light-matter interaction Hamiltonian can be described by dipolar approximation as :

$$\hat{W} = -\frac{q_e}{m_e}\|A\|\hat{p}\cdot u \tag{1.54}$$

Where $\|A\|$ and u are the potential and polarization vector of light respectively, $\hat{p}$ is the momentum operator acting on the wave function of electrons. The presence of spin-orbit coupling allows $\hat{W}$ to couple states with different magnetization[110]. Meanwhile, from Boltzmann's equation, the rate of variation of occupation factors $f_{n,\vec{k}}$ of electronic states can be calculated through :

$$\frac{\partial f_{n,\vec{k}}}{\partial t} = \sum_{n'}(\Gamma_{n'\vec{k}\to n\vec{k}} - \Gamma_{n\vec{k}\to n'\vec{k}}) \tag{1.55}$$

Finally, the dynamics of magnetization revolution is :

$$\frac{\partial M}{\partial t} = \mu_B\sum_n \frac{1}{\Omega_{BZ}}\int_{BZ}\langle\, \psi_{nk}|\hat{\sigma}|\psi_{nk}\rangle\frac{\partial f_{nk}}{\partial t}d\vec{k} \tag{1.56}$$

Figure 1.20 shows the rate of change of magnetization $\frac{\partial M^{\sigma\pm}}{\partial t}$ induced by σ^+ or σ^- light. It can be seen that the induced magnetization is always opposite to the exsting one for both helicities in various materials. Meanwhile, the difference of magnetization variation $\frac{\partial M^{\sigma^+}}{\partial t} - \frac{\partial M^{\sigma^-}}{\partial t}$ between two helicities is shown in the figure, it indicates that the favored magnetization orientation depends on the materials, as well as the photon energy in some cases such as in $\mathrm{L1_0}$ FePt. Besides, the effect is significantly weakened as the photon energy increases. Overall, this effect could be an essential origin of AO-HDS.

Even though the theory from Scheid *et al.* has been used to study the helicity-dependent light-induced demagnetization[110;112], no mechanism has been built to explain how the switching is accomplished under the effect of MILA so far. Additionally, no experimental approach has been attempted to verify the presence of MILA and its role in AO-HDS. Therefore, considering our lack of konwledge about MILA effect, only the impact of IFE and MCD on AO-HDS will be discussed in this thesis.

The extraordinary interest in AO-HDS during the last two decades has spurred a vast number of experimental and theoretical investigations that have taught us the following valuable lessons. First and foremost, AO-HDS might occur whenever the interaction of circularly polarized light with magnetic matter depends on the light helicity and should

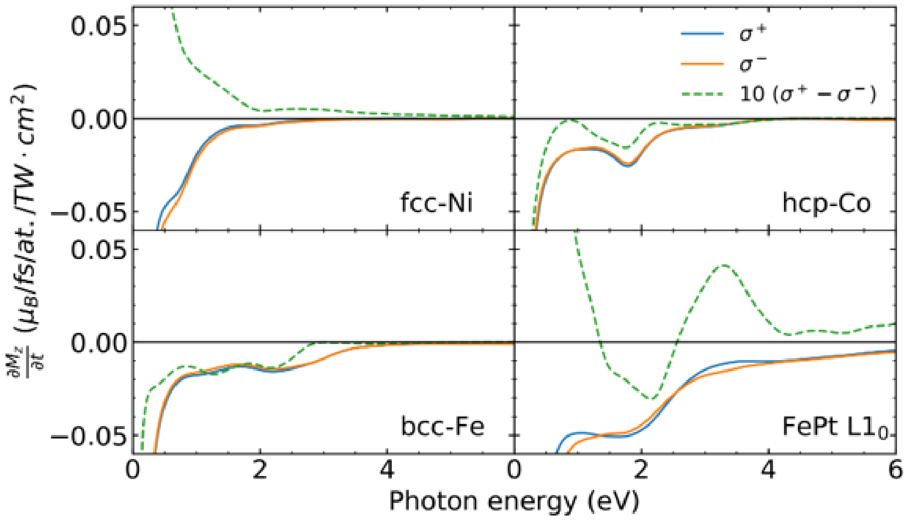

FIGURE 1.20 – Solid lines : the magnetization variation with respect to time induced by optical transitions in fcc Ni, hcp Co, bcc Fe, and L1_0 FePt for σ^- and σ^+ polarized light. Dashed lines : Difference of magnetization variation with respect to time induced by σ^- and $\sigma 2^+$ polarized light scaled by a factor of 10.[110]

therefore be a general phenomenon, and it indeed has been demonstrated for a large variety of magnetic materials[26]. Second, the two most important consequences of excitations of magnetic matter by circularly polarized light are the creation of optically induced magnetizations and that the amount of absorbed energy depends on the mutual orientation between the magnetization and helicity. While the helicity-dependence of absorption is solely ascribed to MCD, optically induced magnetizations are commonly attributed to IFE or MILA. Third, MCD makes heating of a ferromagnetic medium by laser pulses of a particular helicity subject to the magnetic state of the medium. The resulting differences between the temperatures of oppositely oriented domains can lead to AO-HDS via the acceleration of magnetization fluctuations with increasing local temperature or the movement of DW driven by non-local temperature gradients. Thermally activated magnetization fluctuations is initially proposed to explain AO-HDS in granular FePt based recording media[80;96–98], then, another mechanism based on the all-optical helicity-dependent domain wall motion is came up to explain AO-HDS from a different aspect[99–107;113]. In Chapter 3, the physics of AO-HDS from our point view will be exhaustively discussed, a complete mechanism will be proposed and some results will be demonstrated to support this mechanism.

1.5 Conclusion

In this chapter, we first reviewed the discovery of two phenomena of AOS : AO-HIS which is a single-shot toggle switching phenomenon and usually happens in Gd-based RE-TM systems, AO-HDS in which the final magnetization direction is defined by the helicity of light after the exposure and is a general phenomenon happens in numerous materials. Then we introduced some useful concepts and tools for understanding the rest of this manuscript, as well a few basic effects that occur when the magnetic system is induced by a laser pulse. In the following two sections, the material systems, recent progress and theories on AO-HIS and AO-HDS are discussed respectively, allowing us to determine the following path when investigating their mechanism. Even if it has been many years since these two phenomena were initially discovered, we saw that the underlying physics remains an open question which will be the main goal of this thesis.

Chapitre 2

Methods and experiments

This chapter is devoted to present the experimental details of the setups that have been used in this thesis. The tools are involved from the growth of magnetic materials, the characterization of the magnetic properties to the measurement of AOS optically and electrically, the presentation of this chapter will follow this order and divided into three sections.

2.1 Magnetic thin film growth

2.1.1 Physical vapor deposition

There are multiple solutions to grow magnetic thin films, such as chemical vapor deposition, molecular beam deposition, pulsed laser deposition and so on. In this thesis, magnetron sputtering, which is a physical vapor deposition (PVD) technique, will be employed. The working principle of a magnetron sputtering includes the ejection of atoms from a pure element material which is called a target, and the condensing of atoms onto the substrate. In a PVD system, for the first step, electrons are accelerated by an electric field and collide with argon atoms to ionize them, the generated argon ions bombard the target with high energy under the acceleration of the electric field, and the target is sputtered and finally deposited. Therefore, the thin film is formed on the substrate.

Sputtering must be done in a high vacuum environment. The internal structure of magnetron sputtering is shown in figure 2.1. First, the inert gas argon is introduced into the vacuum chamber, and in order to generate the plasma, a high voltage is applied between the target and the substrate. The generated Ar^+ plasma is accelerated by the electric field and bombards the cathode target with extremely high energy. Through energy and momentum transfer, the target material is ejected in the form of neutral particles, which can be atoms, clusters of atoms or molecules. These neutral particles travel isotropically in a vacuum. Atoms that reach the substrate begin to condense and bond with each other, gradually forming atomic layers. In addition, since the bombardment of Ar^+ ions will generate secondary electrons, these secondary electrons will further ionize more Ar^+ ions.

However, there are two main problems with such sputtering. First, the deposition rate can be very slow compared to other techniques, mainly due to the low ionization rate at high vacuum. In addition, since some of the electrons will reach the anode, the

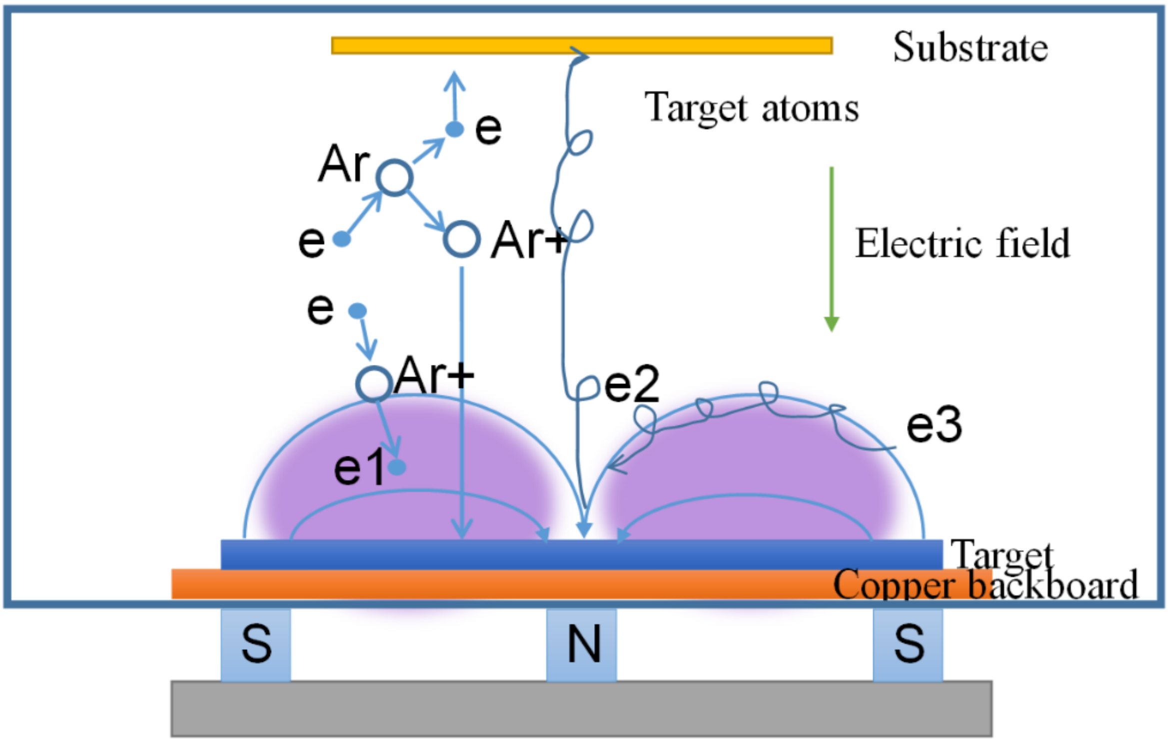

FIGURE 2.1 – Physical principle of a magnetron sputtering.

temperature of substrate will increase, resulting in the growth of porous films. To solve these two problems, a magnetic field is added near the target, as shown in figure 2.1, two magnets with opposite polarities are placed under the target. The resulting magnetic field is parallel to the target surface and perpendicular to the electric field. The combination of the magnetic and electric fields causes the electrons to spiral around the magnetic field lines so that the electrons are bound to areas on the surface of target. In this way, compared to a sputtering without magnetic field, the movement of electrons is greatly extended, which increases the possibility of ionizing collisions with Ar atoms, thereby ionizing a large number of Ar^+ ions. The high density of stable plasma appears near the target surface. Moreover, since a large number of electrons are bound on the surface of the target, fewer electrons reach the anode, the temperature of the substrate can be under control and the quality of film growth will be improved. All samples in this paper were grown with high-quality magnetic films using a magnetron sputtering system from VINCI Corporation.

2.1.2 Growth and magnetic properties of Co/Pt multilayers

In this thesis, Co/Pt multilayers will be grown to study the physics of AO-HDS phenomenon. As introduced in Chapter 1, almost all the material systems, including ferromagnetic material, ferrimagnetic material and antiferromagnetic material, show the AO-HDS phenomenon[26;88;114;115]. There are three reasons can be concluded why we study Co/Pt multilayers in this thesis. Firstly, even in this simplest ferromagnetic system, not much progress has been made to understand the mechanisms of AO-HDS. Secondly, comparing with other material systems like CoTb ferrimagnetic alloys, Co/Pt multilayers shows much better AO-HDS properties, here "properties" refers to those advantages that the material would have for the application of AO-HDS, for instance, Co/Pt multilayers would need less pulses and have a wider switching fluence window acquiring a switching. Thirdly, the ultrathin Co/Pt multilayers can exhibit a strong PMA property thanks to the interfacial anisotropy, crystallographic orientation of buffer layers and the interfacial hybridation of Co and Pt[116–121], and it was evident that the Pt layer would also be polarized by the Co layer[122], therefore, Co/Pt multilayers show large Kerr rotation which will be an advantage for our observation of magnetic domains.

The stack of the sample is : Glass/Ta(3 nm)/Pt(3 nm)/Co(t nm)/Pt(3 nm). We grow the sample under the pressure of $5{\times}10^{-8}$ mbar at room temperature. The glass substrate is used here to make sure we can generate and observe the AO-HDS phenomenon from both sides of the sample simultaneously. The bottom Ta layer improves adhesion of the structure to the glass substrate. Pt layers will introduce a strong PMA as we discussed above and the top Pt layer also prevents sample oxidation.

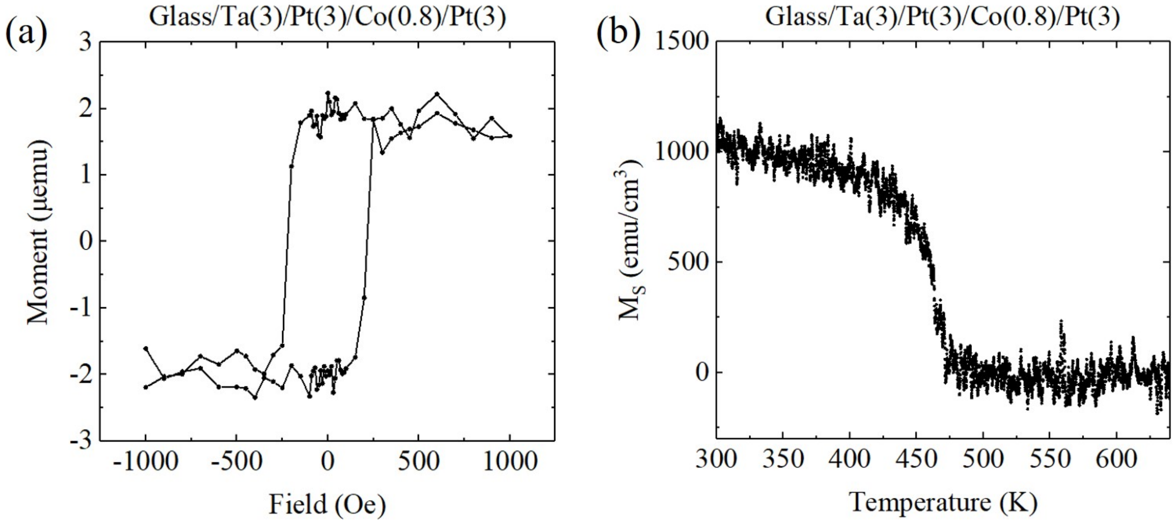

FIGURE 2.2 – (a) The hysteresis MH loop and (b) Curie temperature of Co/Pt multilayer. The H_C of this sample is 250 Oe approximately, the Curie temperature T_C is about 460 K.

We use vibrating sample magnetometry (VSM) technique to characterize the magnetic properties of the samples. VSM is a highly sensitive magnetic moment measuring instrument. It uses the principle of electromagnetic induction to measure the magnetic moment of a sample that vibrates at a fixed frequency and amplitude at the center of a set of detection coils. For a sufficiently small sample, the induced voltage generated by its vibration in the detection coil is proportional to the sample's magnetic moment, amplitude, and vibration frequency. On the basis of ensuring that the amplitude and vibration frequency remain unchanged, by measuring this voltage with a lock-in amplifier, the magnetic moment of the sample to be measured can be calculated.

The hysteresis MH loop and Curie temperature T_C of Co/Pt multilayers with 0.8 nm of Co is shown in the figure 2.2. The sample shows strong PMA and its magnetic moment is in the scale of $\sim\mu$emu, the coercivity H_C of this sample is 250 Oe approximately. Figure 2.2 (b) shows the evolution of magnetization as a function of temperature, T_C is about 460 K which is relatively lower than the value of a bulk Co (T_C = 1400 K as found in handbooks), the reason can be attributed to the intermixing of Co and Pt layers, increasing the Co layer thickness reducing the influence of intermixing can increase T_C.

2.1.3 Growth and magnetic properties of GdRCo alloys

In this section, we will introduce the material system that we used to investigate the mechanism of AO-HIS. As discussed in Chapter 1, AO-HIS was first discovered in GdFeCo alloy which is a RE-TM system in 2007[8], but it was until two years ago that new materials without Gd had been reported to show AO-HIS phenomenon[14–16]. Our study of AO-HIS will still focus on typical Gd-based RE-TM system since its behavior and dynamics has been well studied from previous reports, even though the whole story of AO-HIS is still unclear.

Rare earth is a set of 17 lustrous silvery-white soft heavy metals including Lanthanides, Scandium and Yttrium, however, among all the alloys of these metals and transition metals, only Gd-based RE-TM shows its uniqueness and exhibits AO-HIS. Therefore, in order to study find the most important factor that matters in AO-HIS, especially between Gd and its neighboring elements in periodic table, we doped various amount of Tb, Dy and Ho into GdCo alloys and studied the AO-HIS in these ternary alloys.

The PMA of a RE-TM sample is strongly related to the compensation point where the magnetization of two sublattice is canceled by each other, the coercivity is diverged when the element composition is close to the compensation point. In the figure 2.3 shows the coercivity H_C of DyCo alloys with different concentration of Dy, H_C reaches a maximum value where the magnetizations of Dy and Co are compensated (Dy in 28% for DyCo alloy), when the concentration of RE is far away from the compensation point, the preferred easy axis of magnetization will turn to in-plane.

In contrast to Co/Pt multilayers in which the PMA mostly contributed by interfacial anisotropy, the mechanism of PMA in RE-TM alloys is still under debate. There are many suggestions trying to reveal the origin of PMA in these materials, such as anisotropy pair correlation[123–126], bond-orientation anisotropy[127], dipolar effects[128;129] and magnetostriction[130]. In addition to the concentration and temperature, lots of other factors may also affect the PMA strength. The film thickness is a critical factor for obtaining PMA in RE-TM alloys[131;132], for example, it has been reported that the rare earth may not contribute

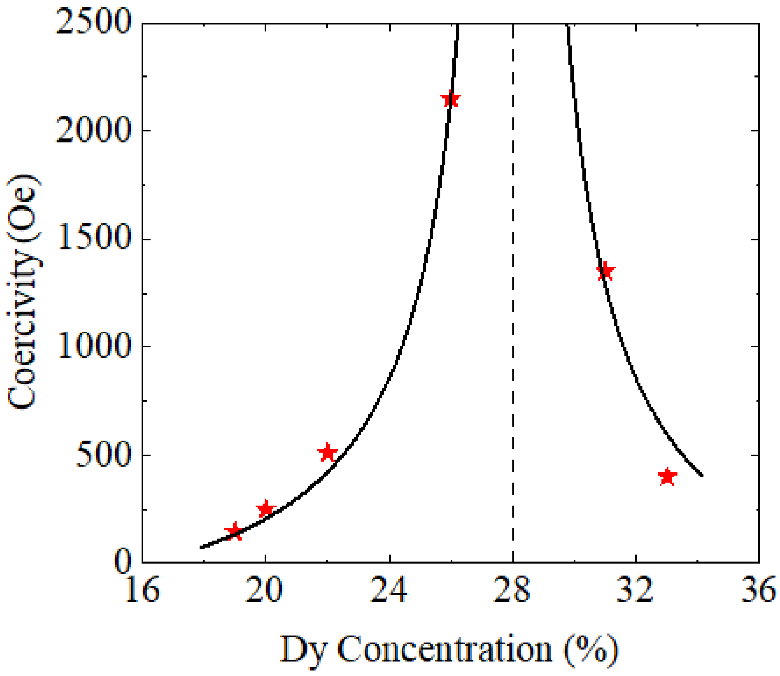

FIGURE 2.3 – The coercivity H_C of DyCo alloys with various composition, the divergence of H_C indicates the compensation point of DyCo alloys is 28% of Dy.

to the magnetization and the magnetization compensation cannot be observed when the film is very thin, while the PMA shows little dependence on the thickness when the film is thicker than 5 nm[133;134]. Past years, lots of studies have shown that the underlayer of RE-TM is important to build PMA[135–137], some material like Ta may decrease the magnetic ordering of rare earth atoms at the interface, resulting in the reduction of PMA. Additionally, the growth condition (including the deposition rate[138], substate[139], vacuum condition, etc.) and annealing procedure[140;141] also play an important role.

Consider all these factors that contributes to the PMA of RE-TM alloys, a complete series of 10-nm-thick $Gd_yR_{1-x-y}Co_x$ (R=Tb, Dy and Ho) alloys are prepared by magnetron sputtering onto a glass substrate according to the following multilayered structure : glass/Ta(5 nm)/Pt(3 nm)/$Gd_yR_{1-x-y}Co_x$(10 nm)/Pt(5 nm). The alloy of GdRCo layer is done through the co-sputtering method, by adjusting the sputtering power of three elements separately, the speed of deposition can be controlled and thus the element concentration is manipulated for obtaining the desired composition of alloys. There is a large range of samples around the compensation point show very strong PMA property. For R = Dy, figure 2.4(a) shows the hysteresis loops at room temperature with a magnetic field applied perpendicular to the film plane for various compositions of Gd when x = 72%. All these square loops with a remanence ratio of about 100%, indicate the well-established PMA of the samples. As is shown in figure 2.4 (b), the polarity of the hysteresis loops reverses in sign at concentration value of x = 74%, suggesting the magnetization compensation point (x = x_{comp}) is between x = 72% and 74% at room temperature. The net magnetization reaches zero and H_C diverges at x_{comp}. In figure 2.4 (c) and (d), we show the coercivity H_C and saturation magnetization M_S mapping of $\mathrm{Gd}_y\mathrm{Dy}_{1-x-y}\mathrm{Co}_x$, respectively, for different concentrations of Co and Gd. The red and blue colors represent the high and low values of H_C and M_S. Obviously, the maximum H_C and minimum M_S occurs around x = 72%, simultaneously.

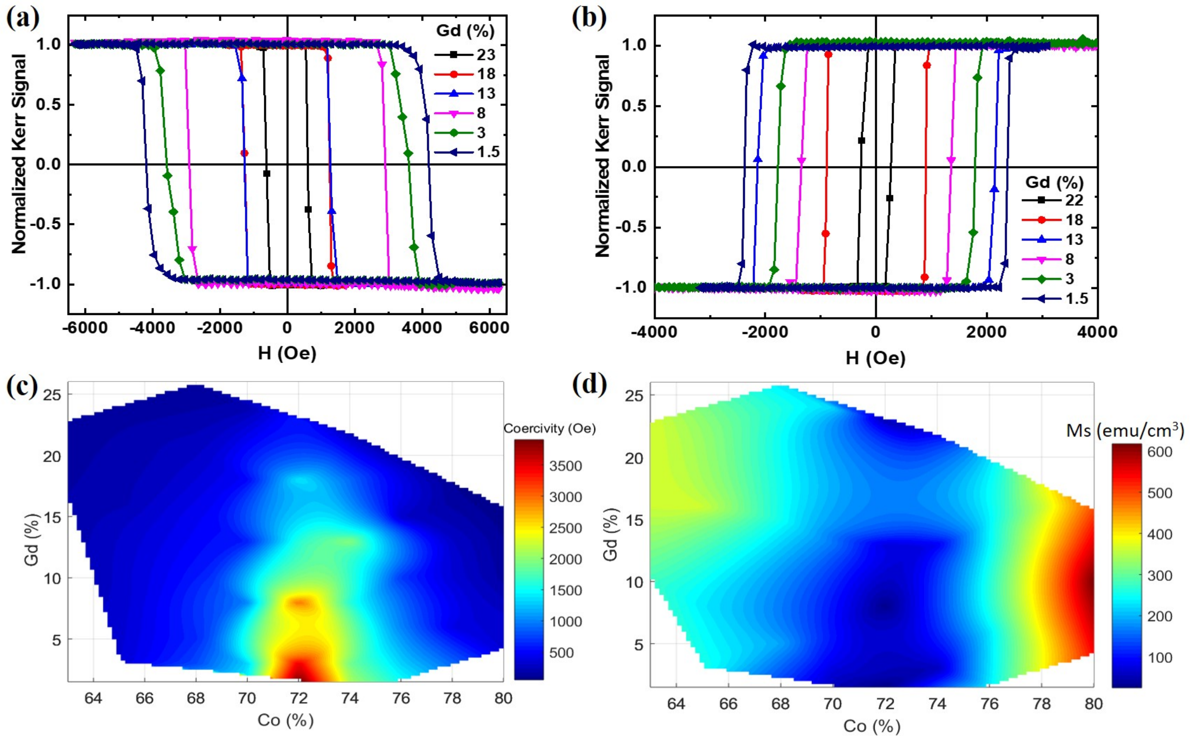

FIGURE 2.4 – Measurements of static magnetic properties of GdDyCo. Magneto-optic Kerr effect loops obtained with the magnetic field applied perpendicular to the film plane, for thin films $\mathrm{Gd}_y\mathrm{Dy}_{1-x-y}\mathrm{Co}_x$, with (a) x = 72% and (b) x = 74%, respectively. They show the opposite sign of the hysteresis loops due to the rich element. The mapping of (c) H_C and (d) M_S with various concentration of Gd and Co elements, from which one can clearly see the compensation point is around 72% of Co.

For R = Tb, x_{comp} is between 74% and 76%, while x_{comp} depends on the concentrations of both Co and Gd when R = Ho since the huge difference of compensation temperature between HoCo and GdCo. All the samples of GdCo doped with Tb and Ho show similar magnetic properties as with Dy. These samples of three series will be used to study the mechanism of AO-HIS in Chapter 4.

2.2 Magneto-optic technology

2.2.1 Magneto-optic Kerr effect

Magneto-optic Kerr effect (MOKE) refers that when the polarized light is incident on the surface of magnetized medium, the polarization characteristics of the reflected light will be changed by the influence of the magnetized medium, from linearly polarized light to elliptically polarized light. The angle between the long axis of elliptically polarized light and the direction of incident linearly polarized light is called the Kerr rotation angle θ_K, and the ellipticity of the elliptically polarized light is called the Kerr ellipticity ε_K. And fundamentally, θ_K and ε_K are proportional to the magnetization of medium.

Early in 1854, Michael Faraday discovered the Magneto-optic effect in a glass between two magnetic poles[90]. He observed that when the magnetic field is parallel to the direction of incident light, the polarization of light will rotate, the rotation angle is related to the magnetic field and the distance the light travels in the medium. Then in 1877, John Kerr also observed similar effect when the light reflects from a polished electromagnet[142;143]. So far, MOKE has been proven to be a very effective and sensitive technique for detecting magnetic properties.

Microscopically, MOKE is a coupling effect that occurs between the electric field component of light and the magnetic moment of sample, which is related by the electric dipole moment related to the spin-orbit interaction. For the linearly polarized light, it can be divided into the combination of left and right circularly polarized light, the electric field of left (E^-) and right (E^+) circularly polarized light can be expressed as :

$$E^{\pm}(r,t) = \frac{E_0}{\sqrt{2}} e^{i(\omega t - rk^{\pm} + \Phi_{\pm})}(x \pm iy) \tag{2.1}$$

Then a linearly (E^L) polarized light can be written as :

$$E^L = \frac{1}{\sqrt{2}}(E^- + E^+) \tag{2.2}$$

Then let's consider a linearly polarized light travels perpendicular to the surface of sample, in z direction. Assuming $\Phi_\pm = 0$ and $z = 0$ at the sample surface, the electric field at a depth δ in the sample can be written as :

$$E(\delta,t) = \frac{E_0}{\sqrt{2}}\left(\left(e^{i(\omega t - k^+\delta)} + e^{i(\omega t - k^-\delta)}\right)x + i\left(e^{i(\omega t - k^+\delta)} - e^{i(\omega t - k^-\delta)}\right)y\right) \tag{2.3}$$

After the light has passed through the magnetic material with a thickness t, because of the difference of k vectors of different helicities and the magnetization of sample, the electric field measured will be :

$$E_y(z,t) = \frac{2E_0}{\sqrt{2}} e^{i(\omega t - kz - \bar{k}\delta)} \sin(\tilde{k}\delta) \tag{2.4}$$

Where $\bar{k} = \frac{k^+ + k^-}{2}$ and $\tilde{k} = \frac{k^+ - k^-}{2}$, we define the complex Faraday rotation $\Phi_F = \tilde{k}\delta$, and it can be expressed as[144] :

$$\Phi_F \approx i \frac{\sqrt{k^+} - \sqrt{k^-}}{\sqrt{\frac{ck^+k^-}{\omega}} - 1} \tag{2.5}$$

There are three working modes of MOKE system : polar, longitudinal and transverse. As shown in the figure 2.5, for polar MOKE, the magnetization is perpendicular to the sample surface and parallel to the plane of incident light, the Kerr rotation reveals the signal of magnetization out of plane ; for longitudinal MOKE, the magnetization is both parallel to the sample surface and plane of incident light, the Kerr rotation reveals the signal of magnetization in plane ; for transverse MOKE, the magnetization lies in the plane of sample and perpendicular to the plane of incident light, in this case, the signal is very weak. Because all the samples studied in this thesis will be of PMA , only the polar MOKE will be used.

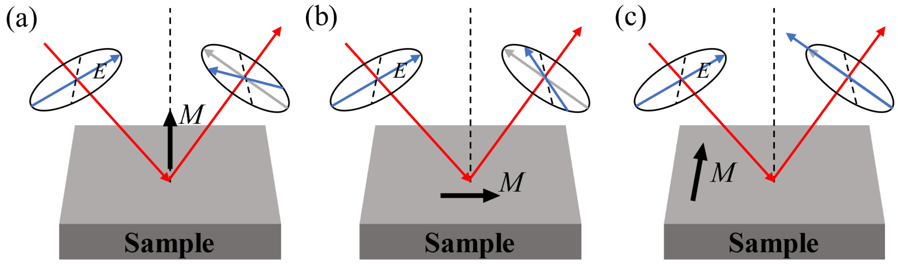

FIGURE 2.5 – Three working modes of MOKE system : (a) polar, (b) longitudinal and (c) transverse.

Besides, two different applications of MOKE will be used in this thesis : MOKE magnetometry and MOKE microscopy. MOKE magnetometry will be performed to measure hysteresis loops because it is field-scannable and has very good signal-noise ratio. MOKE microscopy will be performed to observe the magnetic domains visually by a charge couples device (CCD) camera.

MOKE magnetometry

The schematic of MOKE magnetometry is shown in figure 2.6, it uses a linearly s-polarized helium neon laser as the light source. The reflected light from sample will pass through a photoelastic modulator (PEM) whose vibration axis is parallel to the table, the frequency of PEM is 50 kHz. After passing through a analyzer which is at 45° with respect to the PEM axis, the signal is detected by the photodetector and fed into the lock-in amplifier. By scanning the magnetic field with an electromagnet, the hysteresis loop can be obtained.

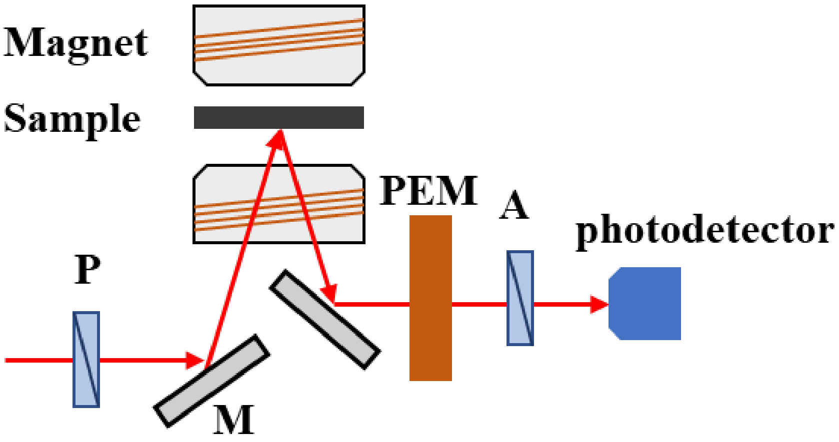

FIGURE 2.6 – MOKE magnetometry setup with following elements : electrical magnet, polarizer (P), analyzer (A), mirror (M), photoelastic modulator (PEM) and photodetector.

The advantage of MOKE magnetometry is that it is a simple, room-temperature and non-destructive instrument, we thus use it to evaluate the magnetic properties of all the samples that we have grown in this thesis preliminarily. Note that for the RE-TM ferrimagnetic alloys, there is no way to decide the output signal (for a given external field) should be positive or negative because only TM magnetization is monitored whereas the net magnetization may be dominated by either TM or RE, the output signals thus will be opposite for TM-rich and RE-rich samples.

MOKE microscopy

The schematic of MOKE microscopy is shown in figure 2.7, the physics of MOKE magnetometry and MOKE microscopy is identical, but different light source and detector are used to enable us to observe the magnetic domain in MOKE microscopy. A light emitting diode (LED) serves as the light source with the wavelength around 630 nm, similarly, the light is linearly polarized and pass through the microscopy objective to the sample. Here, a beam splitter is used and the light reflects on the sample perpendicularly. The Kerr rotation is acquired after the reflection on the sample. Then, the light travels through the beam splitter and analyzer, and focuses on the senor of CCD with the help of lens. The polarization of polarizer and analyzer is almost (not perfectly) crossed, such as to maximize the signal-noise ratio of Kerr rotation.

The resolution of the microscopy reaches to about 2 μm, ensuring the observation of domain structure after the pulse excitation. The MOKE microscopy will be performed with a pulsed laser system to observe the laser-induced magnetization reversal, which will be briefly introduced in Section 2.3.2.

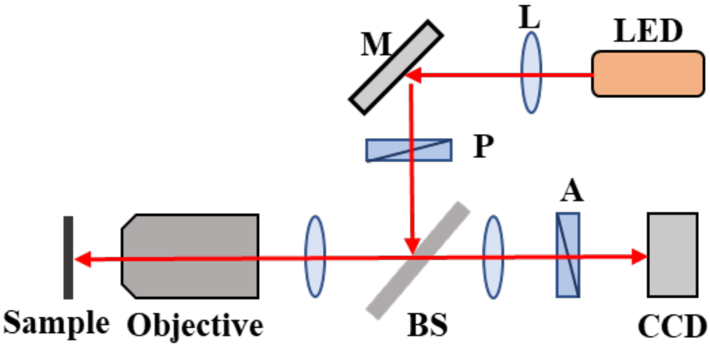

FIGURE 2.7 – Schematic of MOKE microscopy with following elements : LED light source, polarizer (P), analyzer (A), mirror (M), lens (L), objective and CCD camera.

2.2.2 Time resolved MOKE measurement

Time resolved MOKE measurement (TR-MOKE) is based on the pump-probe technique to measure the spin dynamics of the thin film sample. Pump-probe technique was first suggested by G. Porter in 1940s[145]. The illustration of the idea is shown in figure 2.8, using an ultrashort pump laser pulse with high energy to excite the sample from the ground state to the excited state, that is, from the equilibrium state to the non-equilibrium state, then sample relaxes from non-equilibrium state to equilibrium state itself. During this process, using another low energy probe laser pulse, which coincides with the pump pulse in space and time, to detect the optical characteristics in real time. By changing the delay time Δt between the pump pulse and probe pulse, the dynamics of the transformation of equilibrium and non-equilibrium state can be detected.

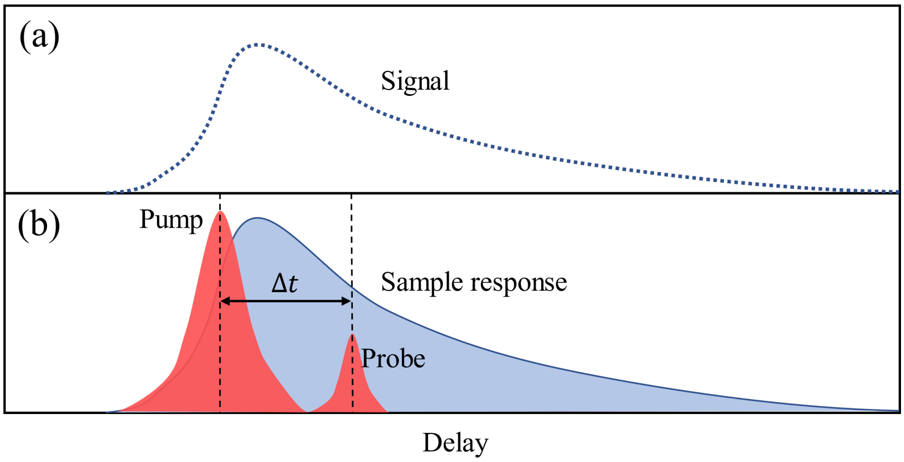

FIGURE 2.8 – The idea of pump-probe technique for TR-MOKE, by changing the delay time Δt between the pump pulse and probe pulse, the magnetization dynamics can be detected.

It is worth mentioning that the laser pulse duration is far shorter than the duration of whole process, and the consistency of laser pulse intensity has to be ensured during the process, because it is important that the pump effect achieved is consistent each time the sample is excited. Besides, the energy density of pump laser has to be much larger than that of probe laser to make sure that the sample is not affected by the probe laser, usually the ratio of the two is 10 : 1. The spot size of pump laser is much larger than that of probe laser and the two spots is concentric, that is to ensure the response of sample in the spot area of probe laser is uniform and better signal-noise ratio.

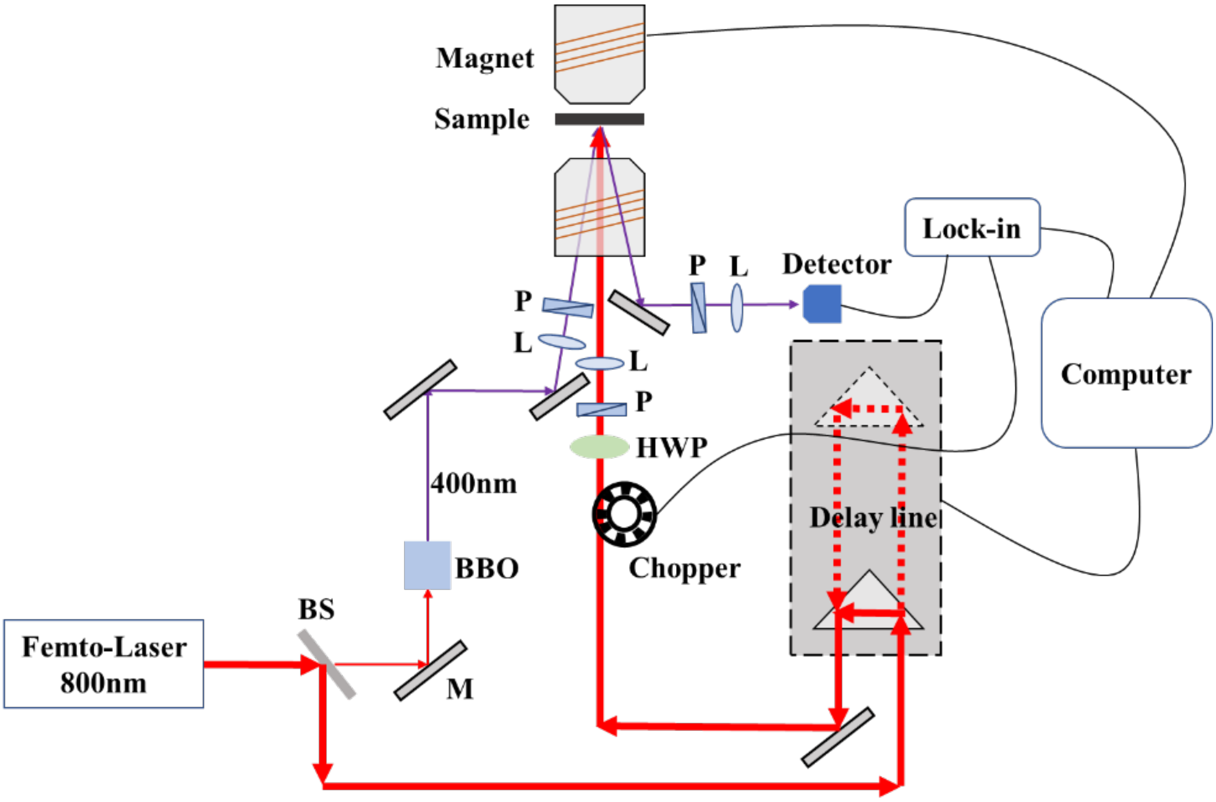

FIGURE 2.9 – Schematic of TR-MOKE setup with following elements : 800 nm femtosecond laser source, beam splitter (BS), mirror (M), barium borate crystal (BBO), lens (L), polarizer (P), electrical magnet, half-wave plate (HWP), chopper, delay line setup, photodiode detector.

TR-MOKE is the combination of a pump-probe technique and a MOKE system, figure 2.9 shows the structure of TR-MOKE in Institut Jean Lamour. The laser is generated by a Ti : sapphire femtosecond laser system from Coherent Inc, and it is continuously sending pulses at a wave length of 800 nm, a pulse duration of 50 fs, and a repetition rate of 5 kHz. Then a beam splitter separates the laser into two beams with the 10 :1 energy ratio. The high-energy pump beam is modulated through a chopper and the delay time will be adjusted by controlling the time of flight of pump laser. After traveling through a lens, a half wave plate and a polarizer, the pump laser is focused on the surface of sample vertically and the out of equilibrium magnetization dynamics is generated, the power of pump laser can be controlled through the half wave plate. The probe system is almost the same to a typical polar MOKE magnetometry. The beam firstly doubles its frequency by a barium borate crystal, that is, the wave length of the probe laser downs to 400 nm. Therefore, the transitions generated by the probe and the pump will be independent and the transitions induced by the probe will be essentially the same as in equilibrium. Then the beam is polarized and focused on the area where the pump spot is through a polarizer and a lens. The angle between the incident probe light and the normal direction of sample surface is less than 10°. After traveling through a polarizer which works as an analyzer and a lens, the reflected probe beam is detected by a balanced photodiode. The output differential signal is transformed to digital signal after the frequency selective filtering of a lock-in amplifier, and collected by the computer in the end.

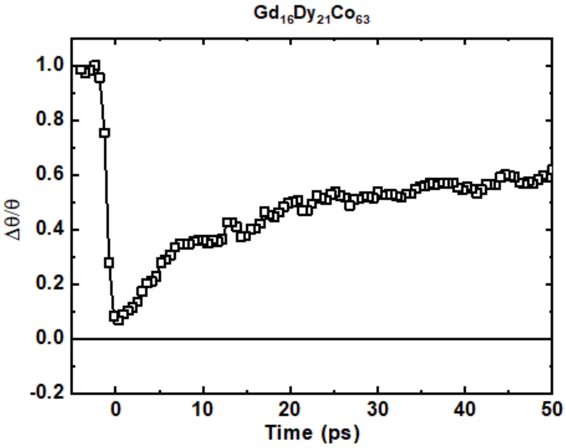

FIGURE 2.10 – Kerr rotation dynamics for a glass/Ta(5 nm)/Pt(3 nm)/$Gd_{16}Dy_{21}Co_{63}$(10 nm)/Pt(5 nm) sample as measured by TR-MOKE setup.

A typical TR-MOKE result of a GdDyCo alloy is shown in figure 2.10, the pump laser fluence is 1.39 mJ/cm^2 which is not sufficient enough to generate a switching, the output Kerr rotation signal $\Delta\theta/\theta$ which is proportional to the variation of magnetization shows the spin dynamics with the pump-probe delay after the laser irradiation in 50 ps.

2.2.3 MCD spectrometer

MCD has been considered as one of the origins of AO-HDS[106;108;146], it indicates the optical absorption difference to the left and right circularly polarized light when passing through a media. In this thesis, a Jasco J-815 MCD spectrometer equipped with a 450 W xenon white light source lamp is used to evaluate the MCD effect of Co/Pt multilayers.

The setup is shown in the figure 2.11, the linearly polarized light with specific energy is obtained by passing through a monochromator and a polarizer, the photoelastic modulator is used to decomposed the linearly polarized light into σ^- and σ^+ light. After traveling through the sample and detected by a photomultiplier, the MCD is calculated by the

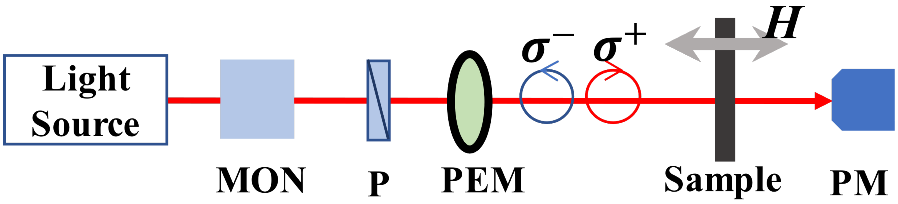

FIGURE 2.11 – Schematic of MCD spectrometer with following elements : xenon white light source, monochromator (MON), polarizer (P), photoelastic modulator (PEM), photomultiplier (PM).

absorption of σ^- light A_L and σ^+ light A_R :

$$MCD = \left| \frac{A_L - A_R}{A_L + A_R} \right| \tag{2.6}$$

The MCD spectra of Co/Pt multilayers with various Co thickness is shown in figure 2.12, the MCD increases with the Co thickness and shows a significant decay after the photon energy reaches 4 eV (corresponding to the wavelength shorter than 310 nm).

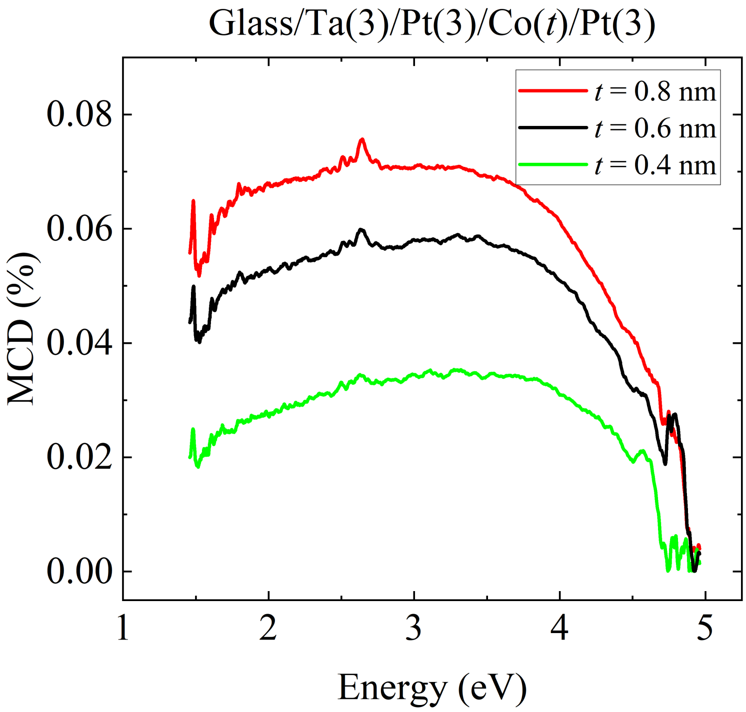

FIGURE 2.12 – The MCD spectra of Co/Pt multilayers with various Co thickness, MCD increases with the Co thickness.

2.3 Observation and characterization of AOS

2.3.1 Fabrication of magnetic devices

In order to perform the electrical measurement to study the domain information with time during AO-HDS, we fabricate the Co/Pt film into a magnetic square on a Hall cross as shown in the figure 2.13 (a). We etch the magnetic Co layer into a square with the width of 10 μm, and etch the bottom Ta and Pt layer into a cross for electrical characterization.

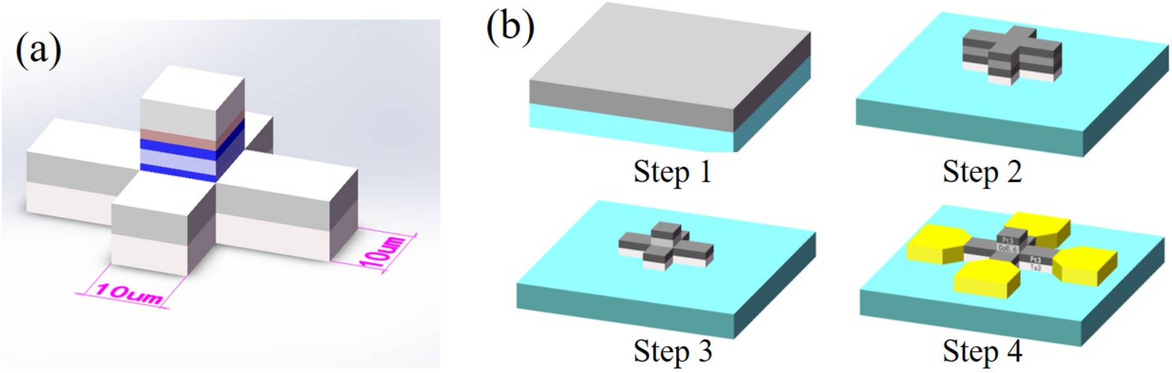

FIGURE 2.13 – (a) schematic illustration of Hall device for AOS and electric transport measurement, the magnetic layer of Co/Pt is etched to a 10 μm wide square. (b) The fabrication process of Hall device.

The process of the fabrication is shown in figure 2.13 (b). The first step of lithography and etching will get a cross channel of 10 μm wide. For the next step, we put a 10×10 μm^2 of photoresist in the center of the cross precisely to protect the top Pt layer and Co layer from the next step of etching. We stop the etching at the bottom Pt layer by controlling the speed and time of etching, thus a four-port Pt/Ta channel with a magnetic Co square in the center can be obtained. It has to be very careful when doing the second step of etching, we use an ion beam etching setup which can distinguish element during the process, once the second layer of Pt has been detected in the chamber, the etching will be stopped immediately. Therefore, a Hall cross structure as shown in step 3 is obtained, only material in the center of Hall cross keeps the complete stack structure. The last step, we deposit the Ti/Au electrodes using a standard electron beam evaporation, lithography and lift-off process. The fabrication of devices is done in the CC-Minalor of Institut Jean Lamour.

2.3.2 The AOS system

We combine the femtosecond laser system, MOKE microscopy and electrical transport measurements to an AOS system which can generate the AOS phenomenon and study the switching optically and electrically simultaneously, as shown in figure 2.14. This system can be divided into three subsystems : ultrafast-laser, electrical transportation and MOKE microscopy.

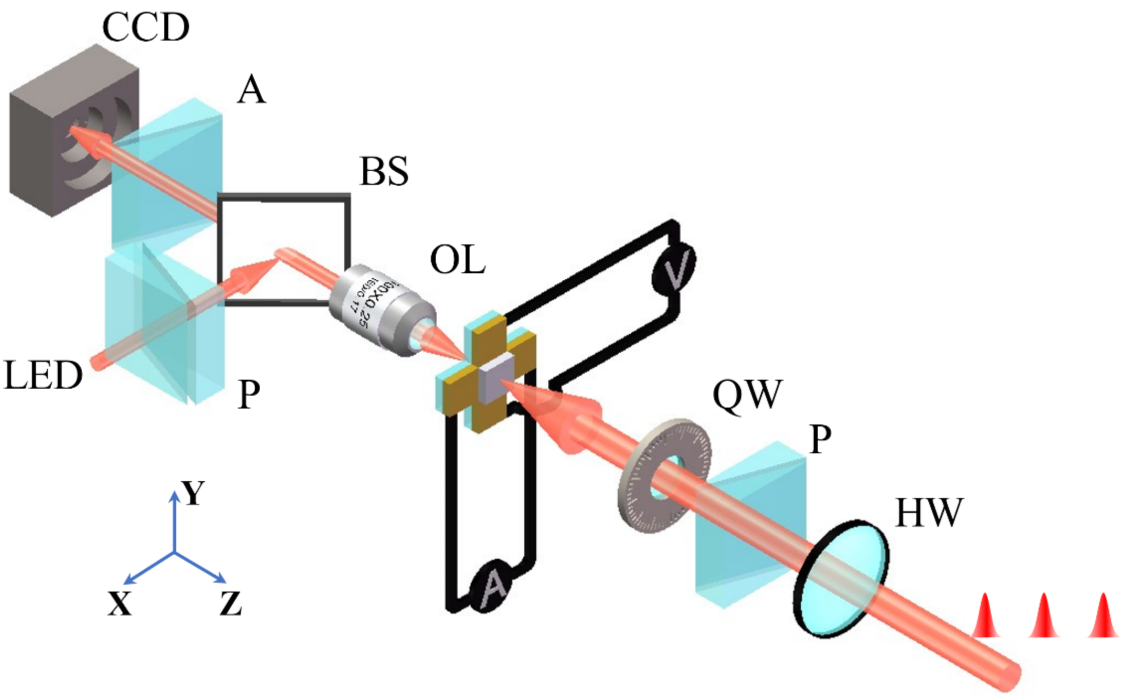

FIGURE 2.14 – Schematic view of the experimental set-up allowing combine Hall resistance measurements and MOKE microscopy on a sample. The helicity of the incident femtosecond laser pulses is controlled thanks to a half wave plate (HW) , a quarter wave plate (QW) followed by a polarizer (P). The laser pulses are focused on a hall cross. The magnetic Co/Pt layer is only present in the central part of the cross (10×10 μm^2 square). The laser pulse width is about 70 μm much larger than the hall cross to ensure a homogenous laser intensity on the sample. The hall resistance is obtained by measuring the current (A) and Voltage (V). The magnetic configuration of the magnetic square is observed using a MOKE microscopy composed of an Objective Lens (OL) a Beam Splitter (BS), a white LED (LED) a polarizer (P), an analyser (A) and a CCD Camera (CCD).

The ultrafast-laser subsystem starts from a Ti : sapphire femtosecond laser system of Coherent Inc. The wave length of laser is 800 nm. The laser system equips with a pulse picker which can adjust the pulse number in multi-shot mode or the repetition rate in continuous mode, the highest repetition rate for this system is 5 kHz. Additionally, the pulse duration can be operated by stretching or compressing the pair of grating in the pulse picker. After traveling through a half wave plate, a polarizer, a quarter wave plate and a convex lens, the laser beam excites on the center of the device or the full film. The half wave plate is used for controlling the power of laser by introducing a phase different of π, while the quarter wave plate combined with a polarizer is used for obtaining a left or right circularly polarized light by introducing a phase difference of $\pi/2$. The convex lens helps to focus the laser beam on the sample surface with a spot size of 70 μm. The spot size can be modified by displacing the lens, for the measurement of Co/Pt device with a width of 10 μm, we make sure that the device is placed in the center of the spot. Considering the spot size of 70 μm is much larger than the size of device, the Gaussian distribution of the laser power from spot center to edge can be ignorable and the fluence on the device can be considered to be uniform.

The electrical transportation subsystem is based on the measurement of anomalous Hall effect (AHE). It was in 1881 that Hall discovered that the Hall effect in ferromagnetic material is ten times larger than in non-magnetic conductors[147], this is then called AHE. Indeed, when applying a longitudinal current in a ferromagnetic material, its transvers Hall resistance ρ_{xy} will include not only the traditional field-dependent item, but the anomalous part which is decided by the magnetization of sample :

$$\rho_{xy} = R_0 B + 4\pi R_S M \tag{2.7}$$

Where R_0 is the Hall coefficient, B is the external field, R_S is the anomalous Hall coefficient, in general, R_S is at least an order of magnitude larger than R_0 and strongly dependent on temperature. Therefore, the transverse Hall voltage can be measured in ferromagnetic devices even without external field. Besides, in our Co/Pt multilayers, because of the strong spin-orbit coupling of Pt, the spin-dependent scattering of conduction electrons is enhanced, leading to a contribution to AHE[148].

Based on AHE, the electrical transportation subsystem is composed of a Keithley 6221 current source and a Keithley 2182 nano-voltage meter. By applying a DC current through the longitudinal channel of Hall cross and measuring the transverse voltage, the Hall resistance ρ_{xy} is obtained.

The MOKE microscopy subsystem will be set up on the opposite side to the laser system, so that we can generate AOS phenomenon and observe it at the same time, that is the reason why we use glass as the substrate. The theory of MOKE microscopy has been introduced in Section 2.2.1, the combination the three subsystems is shown in the figure 2.14. In addition, for the purpose of obtaining a good resolution in MOKE microscopy, the upper sider of the sample will face to the microscopy and the laser pulse will excite the sample from the substrate side.

2.4 Conclusion

In this chapter, all the experimental methods have been explained. We started by introducing the sample configuration and how they are grown by a PVD system. We then presented the technologies that has been used to characterize the magnetic properties of the samples, including MOKE, VSM, MCD and AHE. In order to study the spin dynamics and domain behavior induced by laser pulse, the TR-MOKE and an AOS system are employed based on those magneto-optic effects.

Chapitre 3

AO-HDS in Co/Pt multilayers

In this chapter, we will discuss the behavior and physics of AO-HDS in Co/Pt multilayers. The typical behavior of AO-HDS in full films and devices will be introduced firstly. Some critical factors, including pulse duration, repetition rate, fluence and pulse number, will be studied about how they affect the switching efficiency of sample. Then the domain wall motion (DWM) as a potential driven force of AO-HDS will be discussed, starting from introducing some methods of manipulating the DW. Then, a model to describe the mechanism will be proposed and some experimental results will be presented to support the model. Finally, the mechanism and some future direction of AO-HDS will be suggested.

3.1 Phenomenon of AO-HDS in Co/Pt multilayers

In this section the phenomenon of AO-HDS in Co/Pt multilayers will be demonstrated through two approaches : MOKE microscopy and electrical transportation. The complete stack of the samples is : glass/Ta(3 nm)/Pt(3 nm)/Co(t nm)/Pt(3 nm). All the samples with different thickness of Co show very good switching behavior, in this chapter, unless it is especially mentioned, the plot results are measured from the sample with 0.8 nm Co in which a large Kerr rotation and AHE voltage can be obtained.

3.1.1 AO-HDS in Co/Pt multilayered films and devices

The switching behavior of the Co/Pt full film is shown in figure 3.1, the sample is saturated to M^- with a magnet initially, then a pulse train of 1000 continuous right circularly polarized σ^+ pulses is sent to the sample. In accord with previous studies, AO-HDS is a multiple pulses switching process, to completely switch the magnetization, proper pulse duration and laser fluence are required[149], as well as a certain number of pulses[13]. By selecting the laser fluence of 8 mJ/cm^2, the pulse duration of 1 ps and the repetition rate of 5 kHz, it can be clearly seen that the area that exposed to the light is fully switched to M^+. And by sending another pulse train with opposite helicity σ^- on the same area, the magnetization can be switched back. Therefore, the reproducible AO-HDS phenomenon is obtained in Co/Pt multilayers.

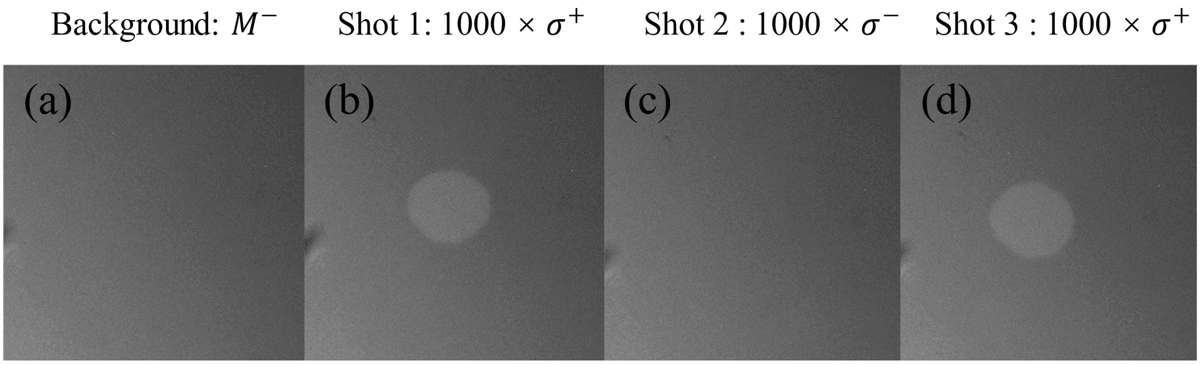

Figure 3.1 – MOKE images obtained : (a) after saturation along the positive z axis with an applied magnetic field $\boldsymbol{M}^-$, (b) under no applied field after 1000 consecutive pulses with a 5 kHz repetition rate, a pulse duration of 1 ps, a fluence of 8 mJ/cm^2 and a circularly right helicity σ^+, (c) under no applied field after 1000 consecutive pulses with a circularly left helicity σ^-, (d) same as (b).

The 10×10 μm^2 magnetic square shows good switching behavior as well. As is presented in the MOKE images (figure 3.2 (a)) and the Hall resistance measurements (figure 3.2 (b)), the magnetization switches to $\boldsymbol{M}^-$ when exposed to 1000 consecutive laser pulses with σ^- polarization and can be switched back using 1000 σ^+ pulses. The applied transverse current for electrical measurement is 0.5 mA, such that no obvious DWM or thermal effect would be induced to the device. Figure 3.2 (c) shows the shape of domain after each pulse. Since it is hard to take the pictures under a frame rate as high as the laser frequency, we shine on the sample pulse by pulse manually and take the picture after each pulse, so the time interval between each pulse is approximately 10 s. The spin dynamics in the initial short timescale is identical between such experiment and a standard high frequency multi-shots all-optical switching, but the former presents the domain revolution in equilibrium after long timescale between each pulse, while the system may be still under a non-equilibrium in a high frequency experiment. But considering the DWM, which is the main domain behavior in longer timescale, is very slow, we believe that figure 3.2 (c) can reveal an approximative behavior during each pulse in AO-HDS. Some important information can be obtained from the images after each pulse. Firstly, the complete switching can be realized after 12 pulses in a small magnetic square, which is much less than that in a full film, indicating that the pulse number is highly related to the area size that need to be switched, thence studying the size effect of AO-HDS could be a direction for the engineering application of AO-HDS. Secondly, during the first few pulses, some random switched domains are created, afterwards these switched domains grow and unit until the switching is accomplished. This indicates that the AO-HDS phenomenon could be described in two-step regime. First, the multi-domain state is formed by helicity independent thermal demagnetization, then, the growth and formation of domains due to a helicity-dependent mechanism accomplish the switching.

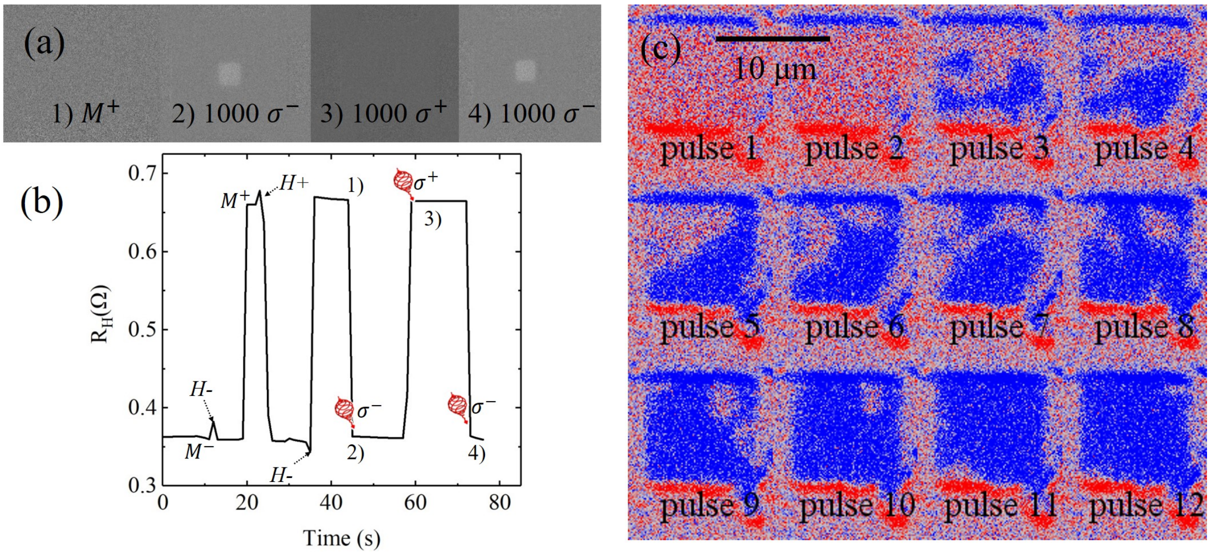

FIGURE 3.2 – AO-HDS using 2 ps circularly polarized laser pulses on a 10×10 μm^2 Co/Pt square. (a) MOKE images obtained : 1) after saturation along the positive z axis with an applied magnetic field (M^+), 2) under no applied field after 1000 consecutive pulses with a 5 kHz repetition rate, a fluence of 2.1 mJ/cm^2 and a circularly right helicity σ^-, 3) under no applied field after 1000 consecutive pulses with a circularly left helicity σ^+ the Co/Pt, 4) same as 2). (b) Hall resistance measurements as a function of time starting from a saturated state along the negative z direction then applying a positive a field along z followed by a negative field further on 1000 σ^- laser pulses, then 1000 σ^+ laser pulses and finally 1000 σ^- laser pulses are applied, the laser fluence is 2.1 mJ/cm^2 . (c) Magnetic configuration obtained after 12 σ^- consecutive pulses. the delay between two pulses is approximately 10s to allow time to take the presented images, hence the fluence is slightly higher than the case of 5 kHz repetition rate (2.5 mJ/cm^2).

3.1.2 The switching properties under various parameters

There are four key parameters that are related to the behavior of AO-HDS : pulse number, repetition rate, fluence and pulse duration. Trying to realize a switching with multiple pulses, proper parameters should be selected. The pulse number and repetition rate are general parameters about the whole pulse train and they constrain each other, fluence and pulse duration are the internal parameters of a single pulse and they are interconnected as well.

Pulse number and repetition rate

Simply put, AO-HDS is a multi-pulse phenomenon and more pulses will produce a more complete switching. Hence, researchers usually use a continuous pulse train and sweep the sample to obtain a switching[8;26;32]. However, the pulse number is a key factor for future potential applications, a small number of pulses needed indicates less time and energy consumed for the writing operation of a magnetic memory device. Besides, the sweeping method increase the complicity and instability of a system design. Fortunately, very good switching performance is shown in the Co/Pt multilayers, we are able to switch the magnetization with a pulse train of only several pulses on a static laser setup. Figure 3.3 shows the relationship between the least pulse number and repetition rate in the samples with different Co thickness. The least pulse number indicates that our magnetic square device can be fully switched in this configuration by choosing a proper fluence, no such proper fluence can be found if the pulse number is less than the least pulse number, lower fluence would not fully switch the whole square while higher fluence would end up with a multi-domain state. For a sample with certain Co thickness, the least pulse number decrease with increasing the repetition rate. For a certain repetition rate, the sample with thicker Co can be switched with less pulses, the sample of 0.8 nm Co shows that it can be switched with only 6 pulses under the repetition of 5 kHz. We will try to explain how the repetition rate and Co thickness impacts the least pulse number after introducing the mechanism of AO-HDS. But it is clear that a higher repetition rate in sample with thicker Co can help decreasing the number of pulses needed.

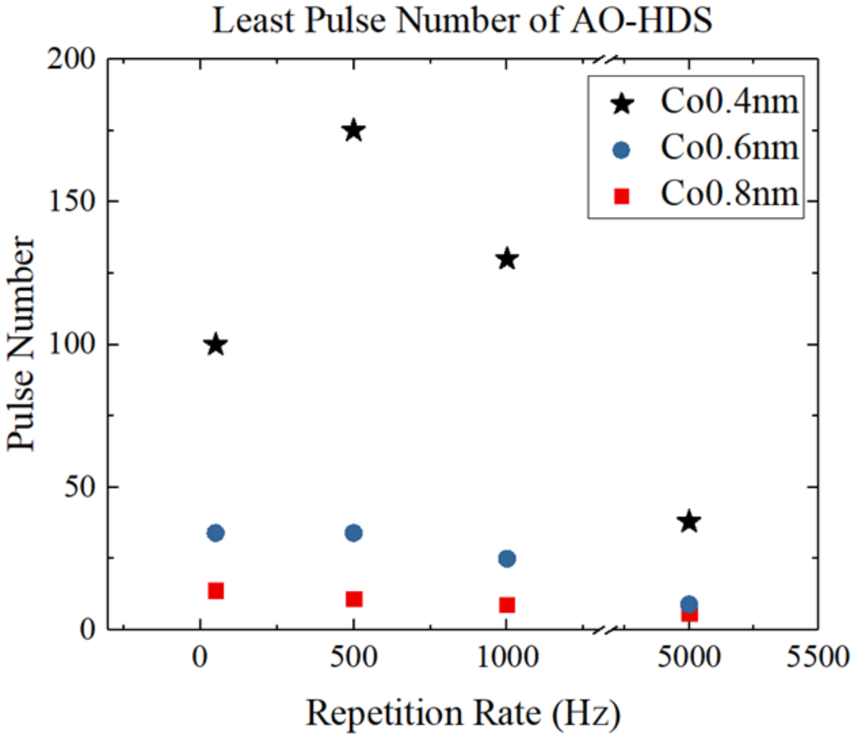

FIGURE 3.3 – The least pulse number needed to obtain a compete switching under different repetition rate for samples with different Co thickness.

Considering the high uncertainty of AO-HDS, especially when the pulse number is small, it is not a good idea to use only several pulses to study the mechanism of AO-HDS, in this thesis, we will mostly use 1000 pulses with the repetition rate at 5 kHz to ensure a stable and complete switching for each excitation.

Fluence and pulse duration

A common assumption is that AO-HDS happens within a fluence range[109], no switching would be observed when the fluence is below a certain threshold while a multi-domain would be brought when the fluence is higher than a certain value. Figure 3.4 shows four different typical AHE response to 1000 pulses with different helicities depending on the laser fluence. Note that we keep measuring the hall resistance as a function of time after the 1000 pulses. The measured hall resistance is normalized such that +1 correspond to positive saturated magnetization M^+, -1 to M^- and 0 to magnetic state whose average component along z is zero, the later is a multi-domain state. The initial magnetization is M^- obtained under a large negative field, then the hall resistance is measured as a function of the number of σ^-, σ^+ and L polarized pulses under four different fluences.

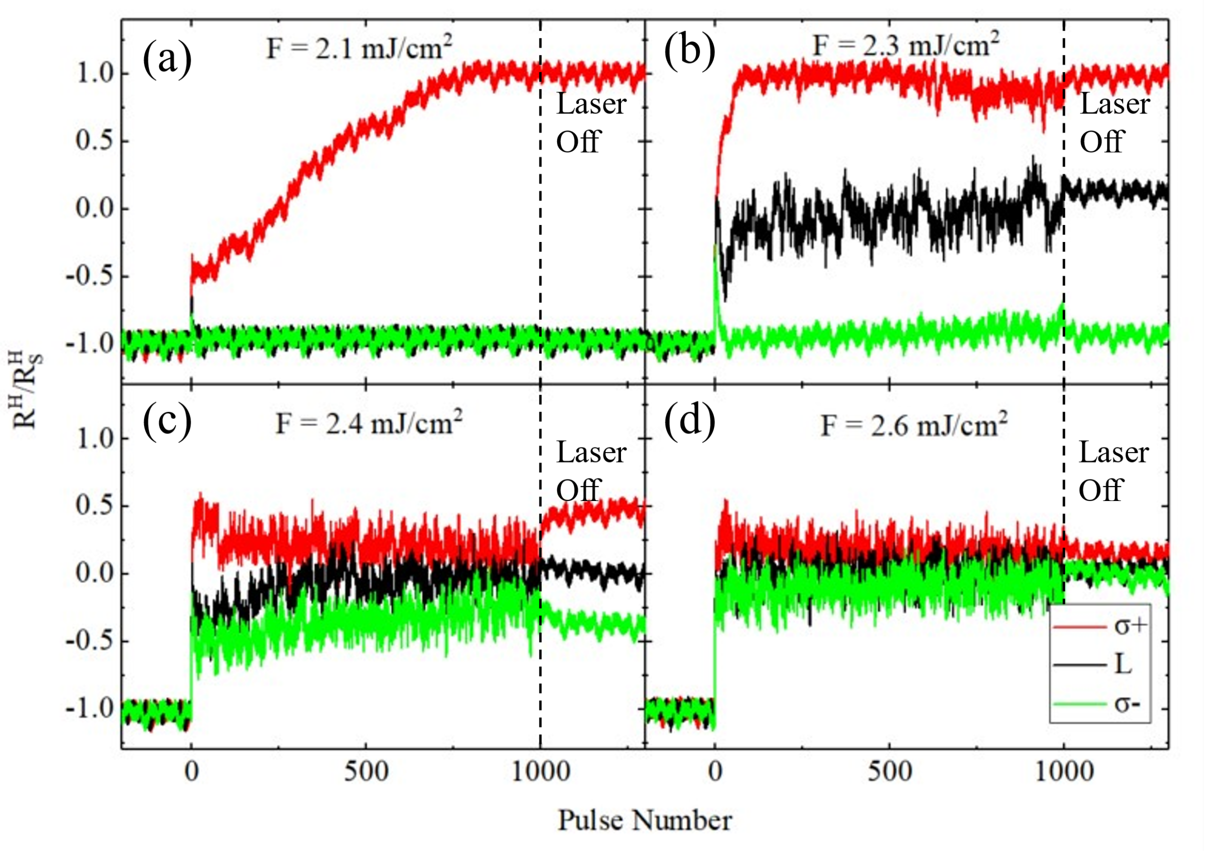

FIGURE 3.4 – Normalized Hall Resistance (R^H/R^H_S) as a function of the number of laser pulses starting from a sample saturated in the negative z direction (M^- with R^H/R^H_S=-1). 1000 laser pulses linearly polarized (L) and circularly polarized left and right (σ^- and σ^+) are shined on the hall cross (a) for a fluence F = 2.1 mJ/cm^2, (b) for a fluence F = 2.3 mJ/cm^2, (c) for a fluence F = 2.4 mJ/cm^2 and (d) for a fluence F = 2.6 mJ/cm^2.

Five different cases is defined and described as follows. For a given pulse duration (here 2 ps) and for a fluence lower than a threshold value (here 2 mJ/cm^2), the laser has no effect on the magnetization switching whatever the laser polarity, we will refer it as Case 0, and above a certain threshold, the laser fluence is too high and for all light helicities a multi-domain state is reached, this will be Case 4. For intermediate fluence we can define :

Case 1 : For 2 mJ/cm^2 < F < 2.2 mJ/cm^2, only σ^+ can switch the magnetic square completely, while L and σ^- laser have almost no impact on the hall resistance.

Case 2 : For 2.2 mJ/cm^2 < F < 2.4 mJ/cm^2, not only σ^+ pulse train leads to the switching as in case 1, but L pulse train also affects the magnetization and bring the system to a multi-domain state. However, σ^- laser pulse train is not affecting the magnetization.

Case 3 : For F = 2.4 mJ/cm^2, all the three polarizations impact the magnetization, but no full switching is observed. L leads to a fully multi-domain state ($R^H/R^H{}_S = 0$) whereas σ^+ pulse train induceds a multi-domain state slightly magnetized along the positive field direction and symmetrically σ^- pulse train creates a multi-domain state slightly magnetized along the negative field direction, after the 1000 pulses for σ^+ and σ^-, the system tends to relax towards the closer saturated state.

Case 4 : For F > 2.5 mJ/cm^2, the fluence is high enough, all three helicities will lead to a demagnetization state in the end.

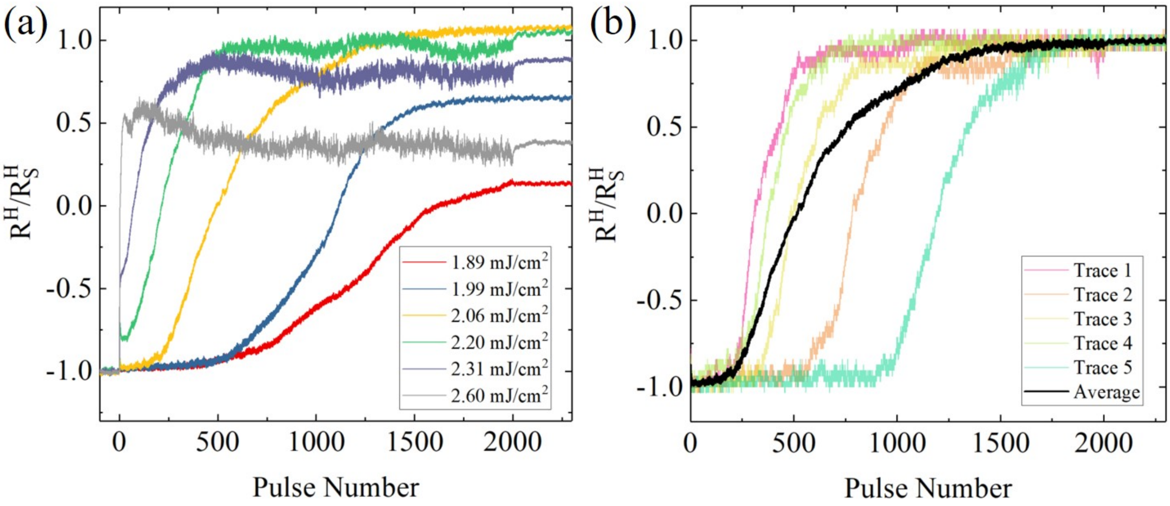

FIGURE 3.5 – Normalized Hall Resistance (R^H/R^H_S) as a function of the number of pulses. (a) Average over 10 measurements for various laser fluence. (b) For fluence F = 2.06 mJ/cm^2, which pulse will wake up the switching process can be very stochastic.

Hall resistance measurements have shown that Stochastic effect plays an important role since for a given laser fluence and pulse duration the measurements can be quantitively different as presented in figure 3.5 (b). For further analysis we have decided to repeat the measurements 10 times and average them as shown in figure 3.5 (a). As the fluence increases to 2.06 mJ/cm^2, the switching ratio increases to 100% after 2000 pulses. And for higher fluence, the pulse number needed for reaching a "mostly switched" state will be reduced. But since more heat is brought to the system, some multi-domain area is created end up with an incomplete switching, the higher the fluence, the larger the area. This result is consistent with the simulation as shown in figure 3.6. By taking both thermal effect and induced opto-magnetic field into consideration, Xiao *et al.* calculated the switching probability of $L1_0$-FePt nanoparticles for a circularly polarized laser pulse with different opto-magnetic fields by atomistic-level simulation[98;150]. Then, they use an accumulative model to simulate the net magnetization after multiple laser pulses with various fluences. Similar rule as in experiment can be found in this model, indicating that the mechanism behind AO-HDS could be a combination of pure thermal effect and non-thermal opto-magnetic interaction.

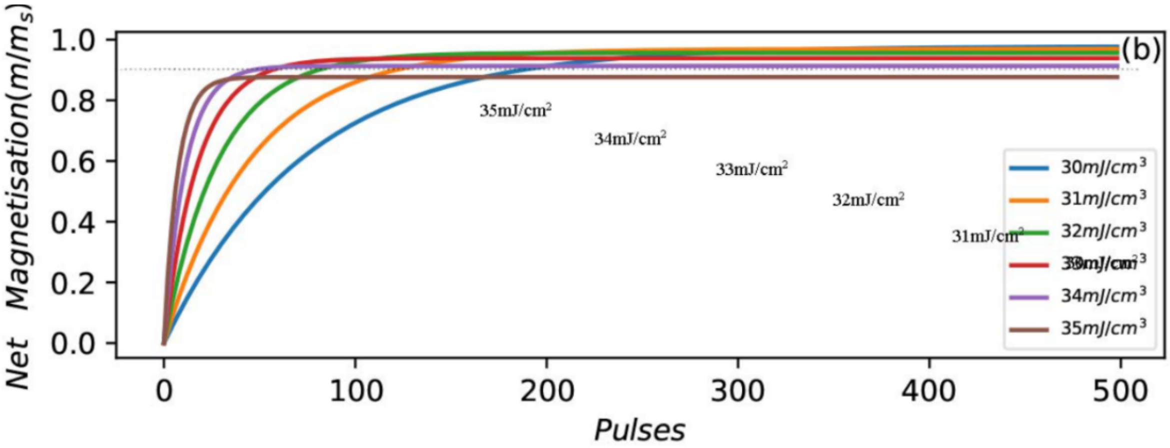

FIGURE 3.6 – Magnetization evolution with the increasing number of laser pulses at various laser fluence.[98]

Fluence is a critical factor, as well as the pulse duration, the measurement of the pulse duration is done precisely through an autocorrelator developed by A.P.E Berlin. We use the full-width at half-maximum (FWHM) of the Gaussian pulse to represent the pulse duration of a laser pulse. The pulse duration shows very significant impact on the fluence window in both AO-HIS and AO-HDS. It has been demonstrated that the switching window of fluence will decrease with increasing the pulse duration in AO-HIS of GdFeCo[13]. However, the AO-HDS in ferromagnetic materials shows completely different relationship between pulse duration and fluence window, the state diagram to show their relationship with static or sweeping laser mode is figure 3.7. An obvious switching window can be achieved only for a pulse duration longer than 600 fs in both two cases, the fluence window becomes wide as the pulse duration increases. Importantly, two new findings are demonstrated in the state diagram. First, the switching regions obtained in two laser configurations are adjacent to each other, the minimum fluence for demagnetization in static laser configuration is close to the critical fluence for switching in sweeping case. Second, the state diagram shows that full reversal is observed only in a narrow range of laser fluence when the laser is static, while a wider switching window could be obtained in sweeping mode. That is the reason why AO-HDS can be easily observed with longer pulse duration and sweeping mode in previous demonstrations[8;88].

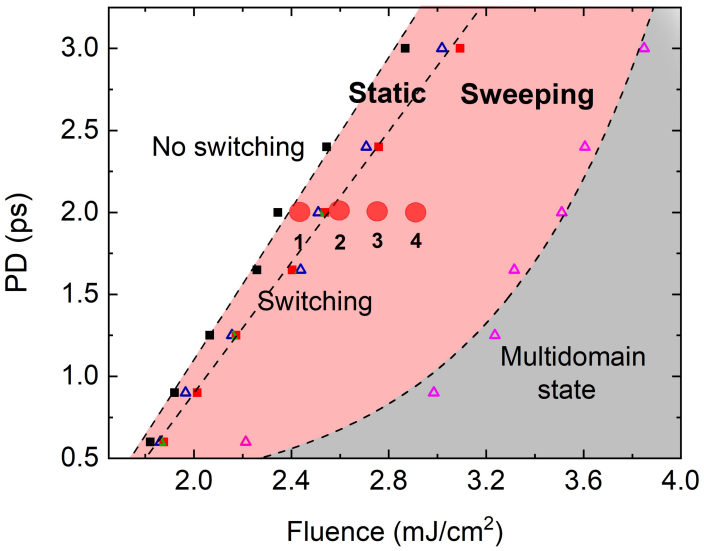

FIGURE 3.7 – Magnetization state diagram as a function of the laser fluence and the pulse duration (PD), obtained with left circularly polarized σ^- laser in both static and sweeping mode. For a given pulse duration, the black and red solid squares indicate, respectively, the critical fluence for switching and minimum fluence required for multidomain-formation in static mode. In the case of sweeping mode, two fluences are indicated by blue and pink hollow triangle, respectively.

So far, it is clear how does the AO-HDS performance of a Co/Pt film related to its four key parameters : pulse number, repetition rate, fluence and pulse duration. If not considering the industrial application of this technology, we are able to conclude the best configuration to observe a perfect switching phenomenon is to use larger number of pulses, higher repetition rate, longer pulse duration and proper fluence related to this pulse duration.

3.1.3 Magnetization dynamics pulse by pulse

Using an oscilloscope allowing measurements every 50 ns helps to study the effect of laser pulses with different helicities on the magnetization dynamics of the 10×10 μm^2 Co/Pt square initially saturated in the M^- direction, as shown in figure 3.8 (a). From those measurements we could observe that after the laser pulse a fast jump (within 2 μs) takes place followed by a slower relaxation until the next pulse is sent, this is a fairly typical behavior that happens after the laser excitation, And the direction of the jumps and the relaxations shows different behavior between the first several pulses and lateral pulses in figure 3.8 (b-c). In this thesis, the jumps and the relaxations will be the core focus to help understanding the mechanism of AO-HDS.

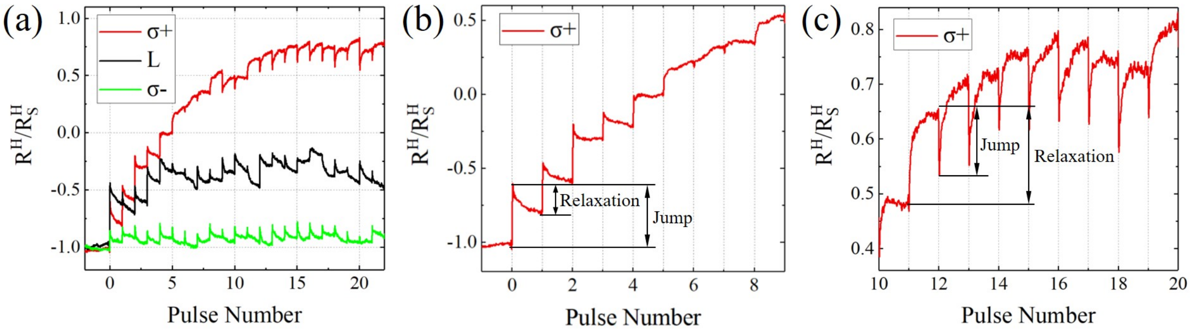

FIGURE 3.8 – (a) The high-resolution dynamics after each pulse under three helicities for a fluence F = 2.3 mJ/cm^2. (b) Zoom on the first part of the magnetization reversal (R^H/R^H_S from -1 to 0) after each laser pulse we can observe a fast positive jump and a slow negative relaxation). (c) Zoom on the second part of the magnetization reversal (R^H/R^H_S from 0 to +1) after each laser pulse we can observe a fast negative jump and a slow positive relaxation.

In the following chapter we will divide all the process into two stages, stage 1 where the net magnetization switches from -1 to 0, and stage 2 where the net magnetization switches from 0 to +1. During stage 1 where the first several pulses bring the normalized resistance R^H/R^H_S from -1 to 0, after each pulse, the fast jump is positive and brings R^H/R^H_S toward 0 whereas the slow relaxation is negative and tends to bring R^H/R^H_S back toward -1. As the jump amplitude is larger than the relaxation, after several pulses, the system reaches a zero-net-magnetization state ($R^H/R^H_S = 0$). After reaching this state, when R^H/R^H_S varies from 0 to +1, the situation is inverted : jumps are negative and tend to bring the system toward the zero-net-magnetization state whereas relaxation tend to bring the system to a positive saturation. In the latter case the amplitude of the relaxations is larger than the jumps and tend to bring the system toward a positive saturation.

In summary, the jumps always lead towards a zero-net-magnetization state and the relaxation always towards the "closer" saturated state. It can be simply concluded that the switching is accomplished through the jump in the early stage and the relaxation in the later stage. The change of Hall resistance is the behavior of Co magnetic moment dynamics, in the following sections, we will focus on the jumps and the relaxations and try to reveal the microspin mechanism behind these two processes.

3.2 Manipulation of DW

It has been widely discussed that the AO-HDS is based on IFE, MCD or the recently suggested MILA effect[95;106–108;110;112;146;151], but weather a laser pulse is introducing a non-thermal magnetic field or a pure thermal effect, the magnetization behaviors driven from these effects are both DWM. In following part, the DWM and some of its driven force will be introduced.

3.2.1 Methods of DW manipulation

Magnetic field driven DWM

In 1998, Ono *et al.* demonstrated that a DW can be pushed by an external field in a NiFe submicron magnetic wire[152], and they studied the DW velocity and showed that the DW velocity is linearly related to the external field in a following work[153]. Atkinson *et al.* briefly measured the DW velocity under the external field and showed that the DW velocity would be different with the direction and magnitude of the field[154], they found that the DW velocity can reach to a very high value of 1500 m/s when applying a field parallel to the magnetization of sample.

Now, with the development of pulsed magnetic field technique and high-resolution CCD camera in MOKE microscopy, the behavior of DWM under the magnetic field has been well studied[155;156]. As shown in figure 3.9, the DW velocity as a function of external field can be divided into different regimes : creep regime, depinning transition regime and flow regime[156].

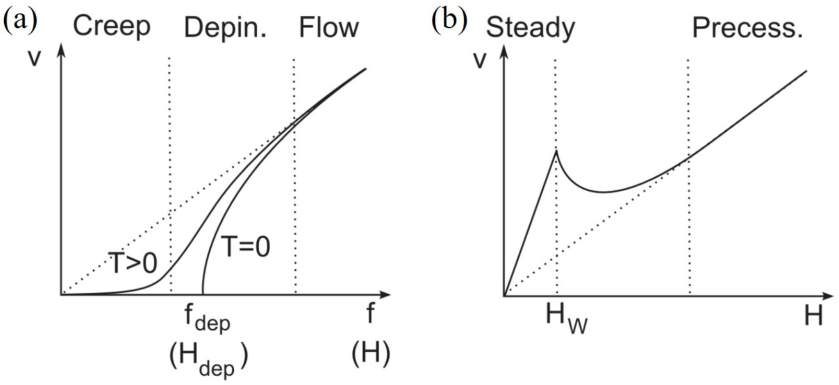

FIGURE 3.9 – (a) Theoretical variation of the velocity v of a DW in a 2D weakly disordered medium submitted to magnetic field at zero and finite temperature T. The creep, depinning and flow regimes are labeled. (b) Regimes of DW flow motion in an ideal ferromagnetic film without pinning. The steady and precessional linear flow regimes are separated by an intermediate regime which begins at the Walker field H_W.[156]

Because of the structure asymmetry of the sample (lattice boundaries, interfacial roughness, interfacial mixing etc.), the existence of a spatial distribution of magnetism in the film leads to a spatial distribution of energy in magnetic DWs, resulting in the pinning effect. At 0 K, a depinning field H_{dep} is usually needed to move the DW, when $T > 0$ K, the DW can be pushed through thermal activating even when the external field is smaller than the depinning field. The thermal activated creep regime under small field can be described as :

$$v = v_0 exp\left(-\left(\frac{U_c}{k_B T}\right)\left(\frac{H_{dep}}{H_{ext}}\right)^{\mu}\right) \tag{3.1}$$

Where U_c is the depinning energy barrier, v_0 is the initial DW velocity and $\mu = 1/4$.

When $H_{dep} \geq H_{ext}$, the DWM can be described as the depinning transition regime. Especially when $H_{dep} = H_{ext}$, the DW velocity as the function of temperature is :

$$v\left(H_{dep}, T\right) = v_T\left(\frac{T}{T_d}\right)^{\psi} \tag{3.2}$$

When T = 0 K, the DW velocity as the function of external field can be expressed as :

$$v\left(H_{ext}, T \ll T_d\right) = v_H\left(\frac{H_{ext} - H_{dep}}{H_{dep}}\right)^{\beta} \tag{3.3}$$

Where v_T and v_H is called depinning velocity, T_d is the temperature related to the pinning strength, ψ and β are constants.

When $H_{ext} \geq H_{dep}$, the DWM goes into the flow regime, and it displaces another three different regimes as shown in figure 3.9 (b). Steady regime where the DWM is dominated by the first term of LLG equation, the DW velocity is given by a linear relation : $v_1 = \mu H_{ext}$, μ represents the DW mobility and $\mu = \gamma\Delta/\alpha$, where γ is the gyromagnetic ratio, Δ is the DW width, and α is the damping constant. When the magnetic field increases to a certain value, the DW periodically changes its structure between Bloch wall and Néel wall, this phenomenon is called the Walker breakdown[157;158]. It can be described through a canting angle ψ that characterizes the out-of-plane vector direction of spins within the DW, when the filed exceeds Walker field, the originally stationary value of ψ is replaced by precession $d\psi/dt \neq 0$. Therefore, in the second region, a nonlinear negative mobility is obtained and lead to the decrease of DW velocity with increasing field. In third region, the positive linear mobility leads to the similar behavior as in the steady regime but with much lower mobility.

Spin transfer torque driven DWM

Berger *et al.* firstly suggested that the DW can be pushed by polarized spin current based on the physics of STT[159]. When the polarized spin current passing through the DW, the spin angular moment of the conduction electrons would be transferred to the magnetization of DW, leading to the DWM. STT driven DWM can be understood from the extended LLG equation :

$$\frac{\partial\vec{m}}{\partial t} = \gamma\mu_0\vec{m} \times \vec{H}_{eff} - \frac{\lambda}{\left|\vec{m}\right|}\vec{m} \times \frac{\partial\vec{m}}{\partial t} + \left(\vec{u} \cdot \vec{\nabla}\right)\vec{m} - \beta\vec{m} \times \left[\left(\vec{u} \cdot \vec{\nabla}\right)\vec{m}\right] \tag{3.4}$$

Where β is the degree of the non-adiabaticity factor for STT. And,

$$u = \frac{JPg\mu_B}{2eM_S} \tag{3.5}$$

Where J, P, g and μ_B denote the current density, the polarization of spin current, the Landé g-factor and the Bohr magneton respectively. In the extended LLG equation, two extra terms are added, the first term, written as $\left(\vec{u}\cdot\vec{\nabla}\right)\vec{m}$, is the adiabatic torque, while the second term, written as $\beta\vec{m}\times\left[\left(\vec{u}\cdot\vec{\nabla}\right)\vec{m}\right]$, is the non-adiabatic torque. The adiabatic torque describes the mutual spin angular moment transfer between spins of conduction electrons and the magnetization of DW and it rotates the spin direction to the majority. On the other hand, the non-adiabatic torque is in the orthogonal direction to the adiabatic torque, so that it acts as an effective field that drives the DW.

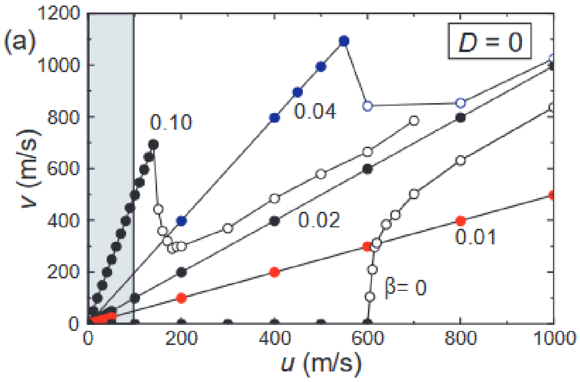

FIGURE 3.10 – Steady velocity computed for a transverse DW by micro-magnetics in a 120×5 nm^2 wire as a function of the velocity u which represents the spin-polarized current density, with the relative weight of the exchange field term as a parameter. Open symbols denote vortices nucleation. The shaded area indicates the available experimental range for u.[160]

When the applied current is large enough that adiabatic torque is able to overcome the torque of the effective field, the DWM with continuous spin precession is generated. Theoretically, the dependence of STT driven DW velocity on the current density is very similar to the result observed in field driven DWM. When the current density is relatively low, the DW velocity follows a linear relation as : $v = \frac{\beta u}{\alpha}$. After a critical current density, the DW cannot maintain its structure and periodically changes like in the field driven model, the DW experiences a Walker breakdown and a precessional propagation as shown in figure 3.10[160]. However, because of the significant thermal effect from the electrical current, only the creep regime under low current has been demonstrated in experiments[161–163].

Spin orbit torque driven DWM

In comparison to STT, DWM driven by SOT, which is a very popular topic in recent years, is a much more energy efficient technique for DW memory devices. In 2008, Moore *et al.* reported the current driven DW motion at the velocity of ∼130 m/s in the direction of the current in Pt/Co/AlO$_x$ heterostructure[164], this result is very surprising because the direction of DWM should be opposite to the direction of current if only consider the exist of STT. Then in the same material, a DW velocity of 400 m/s at the current density of 3×10^{12} A/m^{2}has been reported[165] and they suggested that it is due to the appearance of field-like torque due to the Rashba effect[166]. On the other hand, the magnetization switching by current pulse has been observed in Pt/Co/AlO$_x$ heterostructure by another group, but they concluded the origin to the SOT origin from spin hall effect (SHE) in the heavy metal layer[6;7]. Later, Haazen *et al.* demonstrated the DWM in Pt/Co/Pt multilayers and proved that the SHE plays a decisive role when explaining the fast DWM in perpendicular materials[167].

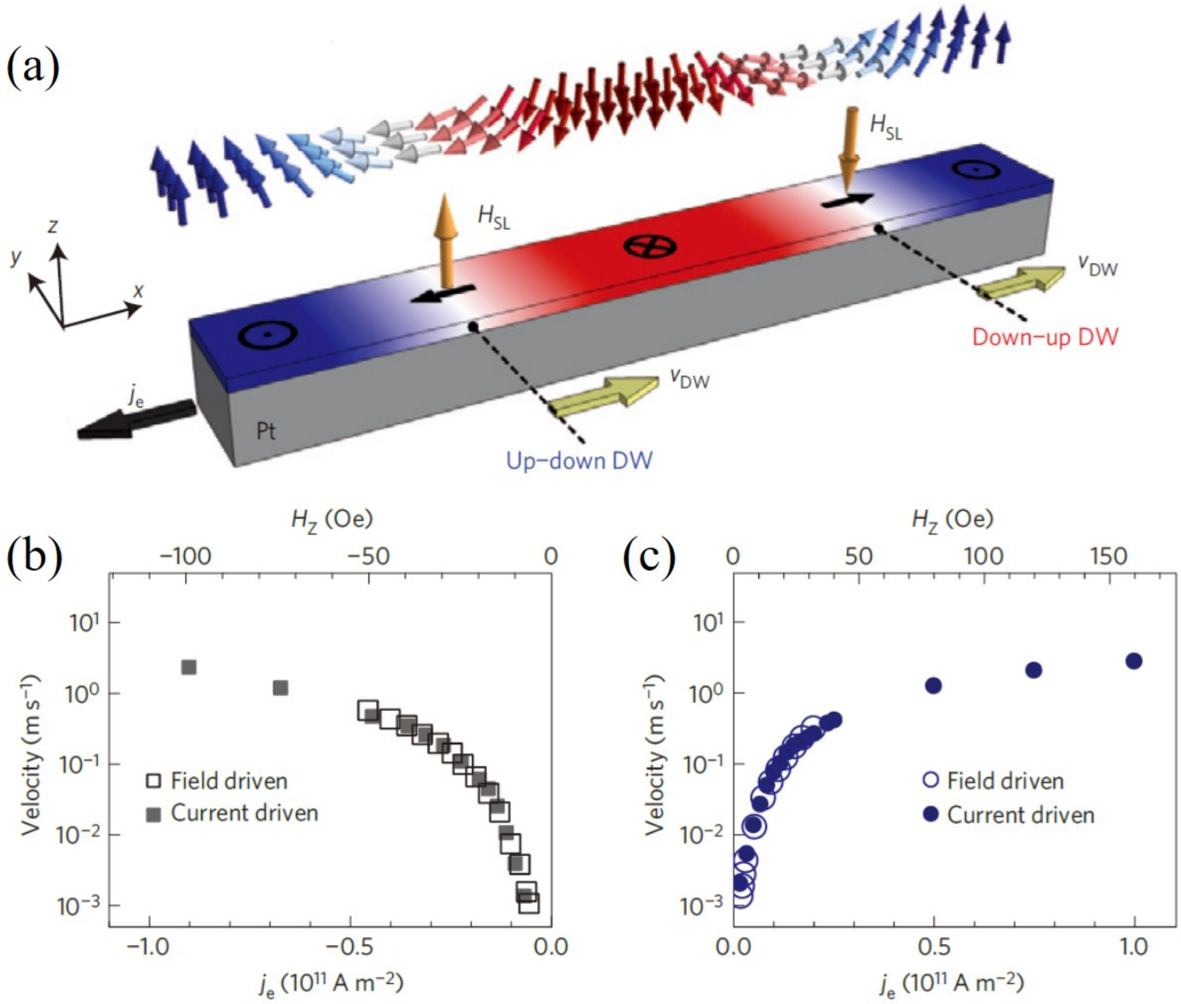

FIGURE 3.11 – the DWM driven by SOT in Pt/CoFe/MgO and Ta/CoFe/MgO magnetic wire : (a) the illustration of DWM in Pt/CoFe/MgO wire, DW moves at a velocity of v_{DW} in the opposite direction of injected current j_e under the effective field H_{SL}. (b-c) the DW velocity as a function of j_e and H_{SL} (b) in Pt/CoFe/MgO and (c) in Ta/CoFe/MgO.[168]

In 2013, Emori *et al.* suggested that the Sloncezewski-like spin torque from SHE could be the origin of DWM by studying the current driven DWM in Pt/CoFe/MgO and Ta/CoFe/MgO as shown in figure 3.11[168]. The Dzyaloshinskii–Moriya interaction (DMI) at the interface of Pt/CoFe results in the formation of Néel wall with left-hand chirality, when a current is applied along x direction, the strong SHE in Pt layer leads to the spin accumulation in y direction at the interface to CoFe layer, the torque from SHE applied to the left-hand chiral Néel wall pushes the DW moves towards the direction of current, which is opposite to the DWM direction driven by STT. On the other hand, for CoFe interfaced with Ta, because Ta has the opposite spin hall angle to Pt[169], the SHE effective field by Ta is contrary. Therefore, the DWM direction observed in Ta/CoFe/MgO is opposite to the direction of current. Because of this kind of rigid and stable formation of Néel wall and its fixed chirality from the DMI of heterostructure, the DW can be high-efficiently driven by SOT.

Thermal gradient driven DWM

The study of DWM driven by thermal gradient TG is based on the theory of spin Seebeck effect[170], which refers to the occurrence of spin current due to a temperature gradient in a ferromagnetic material. The presence of spin Seebeck effect was first demonstrated in 2008[105], Uchida *et al.* showed that the spin-up and spin-down electrons would diffuse to opposite direction in the sample under a temperature gradient. Afterwards some theoretic work has been done to predict the DWM driven by TG[100–103], but it was in 2013 that Jiang *et al.* reported the DWM by TG in magnetic insulators in experiment for the first time[104]. In this work, they thermally excited a magnonic current to transfer its spin angular momentum to the local magnetization inside the DW, leads to the DWM, this observation indicates that insulating magnetic materials could enable thermal STT devices in spin caloritronics[171] as a potential application.

There are two possible mechanisms to explain the physics behind the DWM by TG. The first one is based on the magnonic STT, there is little debates on if magnonic STT can move the DW since it is very similar to the DWM driven by electric current STT. Based on the model from current driven DWM, the DW velocity below the Walker breakdown can be written as[113] :

$$v_D = \frac{\gamma k_B}{\alpha M_S 6\pi^2 \lambda_m} \frac{\partial T}{\partial z} \tag{3.6}$$

Where λ_m is the wavelength of the excited magnons. But it has to be very careful when it comes to the direction of DWM in this case. By far, all the experimental results showed that the DW propagates to the hotter region under a TG[104;107], which means the direction of DWM is opposite to the magnon propagation direction. But indeed, the direction of DWM is strongly dependent on whether the magnons pass through the DW or are reflected by the wall[172]. When the magnons pass through the DW, the magnonic STT between the magnons and the DW makes the wall move in the opposite direction to the magnons. When they are reflected by the DW, the direction of DWM is in the same direction to that of the magnons.

Another approach to explain the DWM by TG is from the point view of entropy[101]. A DW can be consider as a thermodynamic object whose free energy $\Delta F\,(T)$ is minimized, the free energy can be expressed by the internal energy ΔU of the wall and its entropy ΔS as[113] :

$$\Delta F\,(T) = \Delta U - T\Delta S \tag{3.7}$$

Hence, the DW will move to the region with higher temperature to minimize its free energy. Based on the framework of the LLB equation, the DW velocity below the Walker breakdown from a thermodynamic point of view can be written as[101] :

$$v_D = -\frac{2\gamma}{M_S}\frac{1}{\alpha_\perp}\frac{A\,(0)}{T_C}\frac{\partial T}{\partial z} \tag{3.8}$$

For $T \leq T_C$, the temperature dependent transverse damping parameter $\alpha_\perp$ is connected to the atomistic damping parameter λ via $\alpha_\perp = \lambda\,[1 - T/\,(3T_C)]$, Both magnonic STT and entropic torque can be used to explain the DWM by TG, there are still lots of debates which effect is dominant.

3.2.2 DWM by laser

Using laser to manipulate the DW was demonstrated by Quessab *et al.* in 2018[107], in this work, they used a linearly polarized laser pulse train to shine on the DW and its two sides as shown in figure 3.12 (a-c). Because the laser profile follows a Gaussian distribution from center to edge, then a thermal gradient can be created follows the same rule. When the center of spot is right on the DW, no DWM is observed, whereas when the laser center is shifted a little bit to the left or right, the DW will move towards the center of the laser beam until the laser center is right on the DW and no specific DWM direction is preferred. This result proves that laser can create a TG which acts as an effective field, and when the effective field is great enough to overcome an energy barrier of unpinning a DW, the DW is moved.

They also reproduce the same work using pulse trains with helicity as shown in figure 3.12 (d)[106]. In this case, the TG created by the Gaussian distribution of laser is no more dominant, instead of the absorption of the magnetization to different helicities. The DWM direction can be manipulated by changing the helicity of laser. But as we introduced in the previous section, both IFE and MCD can be used to explain the phenomenon of laser induced DWM, IFE acts as a field-driven DWM while MCD acts as a TG driven DWM, it has been widely discussed about the dominant effct when the laser is moving the DW[80;95;99;106;108;146;151].

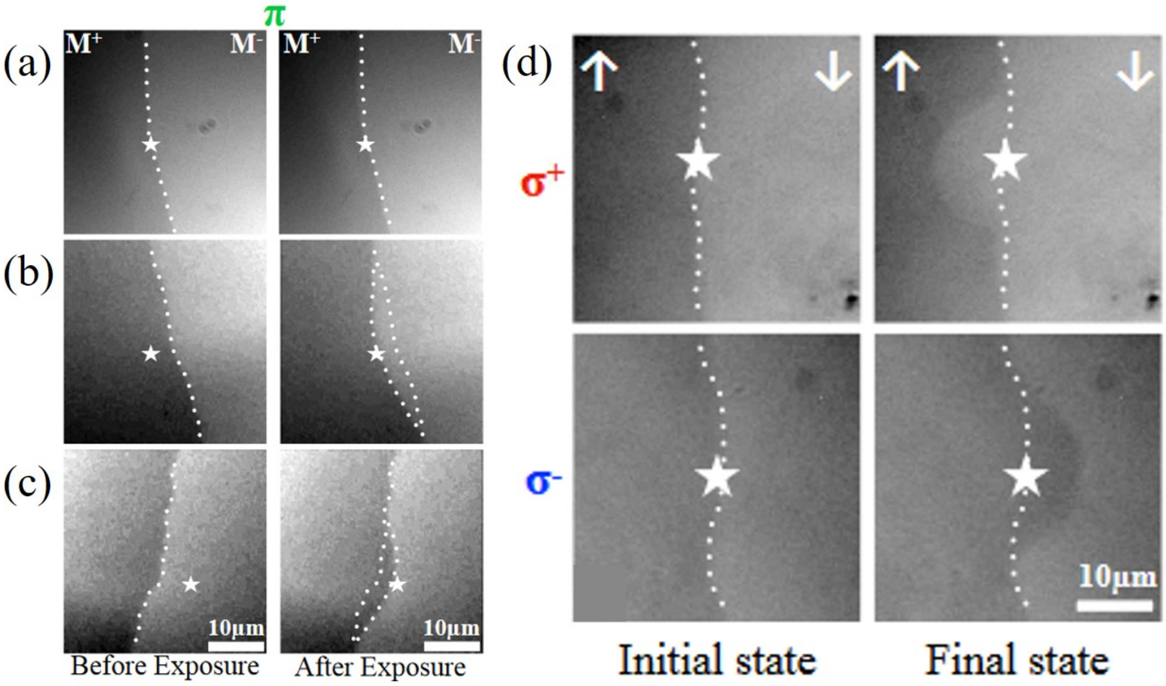

FIGURE 3.12 – (a) and (b) MOKE images of a DW in Co/Pt multilayers exposed to 40-fs linearly polarized (L) laser pulses with a fluence of 7 mJ/cm^2. The laser beam spot (star) is (a) on the DW and off-centered in (b) and (c). The DW moves towards the center of the beam which is the hottest regions[107]. (d) MOKE images taken before and after exposure centered on DW and with a fluence below the switching threshold[106].

We reproduced the phenomenon of laser induced DWM in a channel device of Co/Pt multilayers as shown in figure 3.13. We fabricated a channel whose width is 10 μm and send a pulse train of 3000 pulses on the DW to move it as shown in figure 3.13 (a), because the HWFM in space is about 50 μm which is larger than the channel width, we assume that the Gaussian distribution of laser fluence in space is not significant. With this configuration, the DWM can be observed and its direction is dependent on the helicity of light, the DW will move from M^- to M^+ (resp. M^+ to M^-) when it is exposed to σ^- (resp. σ^+) light. And this rule does not fail when the laser center is a little bit shifted to the DW, it indicates that there is an effective field, weather it is origin from TG or IFE, generated within the range covered by the laser.

We also calcuted the DW velocity under different laser fluence as shown in figure 3.14. Because the laser induced DWM is limited in creep regime where the motion by each pulse is too small to be resolved by our MOKE microscopy. In order to obtain the displacement of domain after each pulse, we send 50 consecutive pulses to get an accumulation of displacement, the duration of each pulse is 2 ps, and the interval of each pulse is 200 μs to make sure that everything has recovered when next pulse arrives. We consider 50×2 ps as the duration of DWM and measure the distance the DW moved after 50 pulses, then

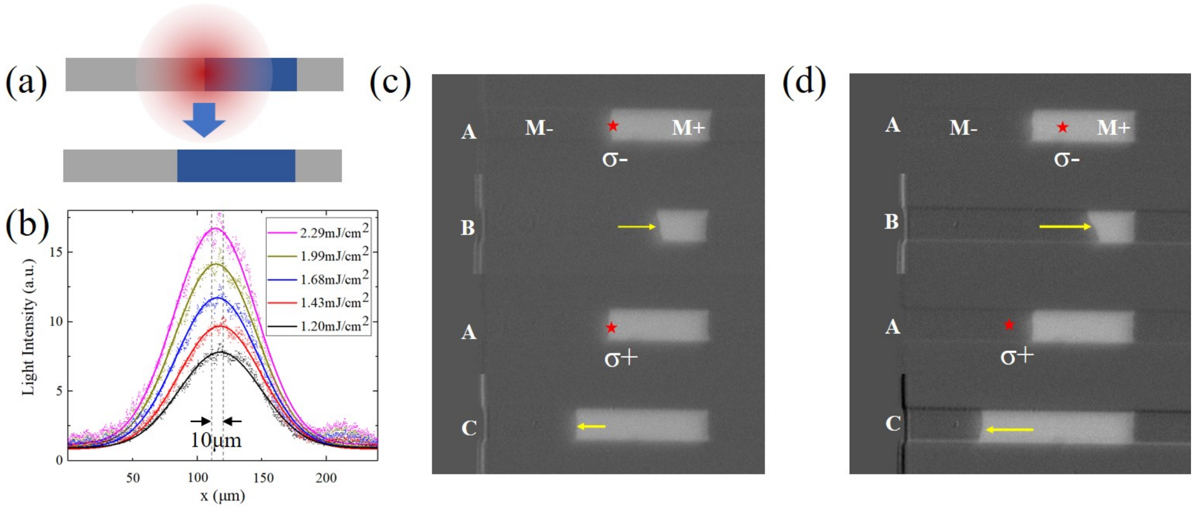

FIGURE 3.13 – (a) A Co/Pt channel with 10 μm width exposed to 3000 consecutive pulses to obtain a displacement of domain. (b) the laser profile of fluence and position, the HWHM of laser sopt in space is about 50 μm which is larger than the channel width. (c-d) MOKE images demonstrates the manupulation of DW using circularly polarized pulse train (c) on the DW and (d) off-centered to the DW.

the DW velocity as the function of laser fluence in creep regime is obtained as shown in figure 3.14 (b).

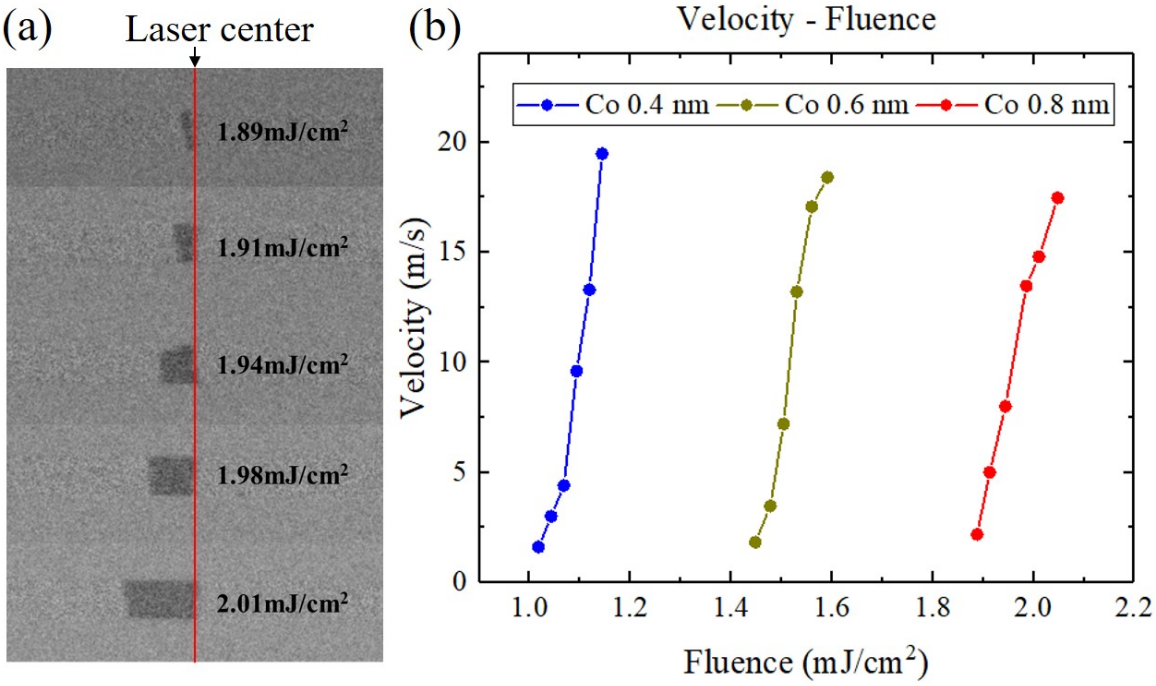

FIGURE 3.14 – (a) Differential MOKE images of after and before the excitation to 50 consecutive pulses of 2 ps pulse duration on the DW with various fluence. (b) The relationship between the DW velocity and laser fluence for samples with different Co thickness in creep regime.

There is two information indicated in this result. First, The DW velocity follows a linear relationship with the laser fluence for three samples with different Co thickness and the slope of linear relationship is almost the same between different thickness, it agrees with two models on the TG driven DWM we introduced before where the DW velocity is also linearly related to the temperature gradient. Second, a higher fluence threshold is needed to generate a DWM for sample with thicker Co, meaning the sample with thicker Co has a higher depinning threshold to overcome. We use the effective depinning field $\boldsymbol{H_{dep}}$ to describe the depinning barrier in TG driven DWM. In fact, $\boldsymbol{H_{dep}}$ itself is difficult to estimate because of the thermal smearing of the depinning transition[156], besides, $\boldsymbol{H_{dep}}$ is related to the PMA which is itself temperature dependent[173], Gorchon *et al.* reported the temperature dependence of DW velocity and external field[174], $\boldsymbol{H_{dep}}$ is decreased with rising temperature as shown in figure 3.15 (b). But it can be easily understood that $\boldsymbol{H_{dep}}$ increase with the Co thickness in ultrathin Pt/Co/Pt films. Similar rules have been reported when the DW is driven by the magnetic field. As shown in figure 3.15 (a), depinning field is obviously larger in sample with thicker Co in creep regime[175].

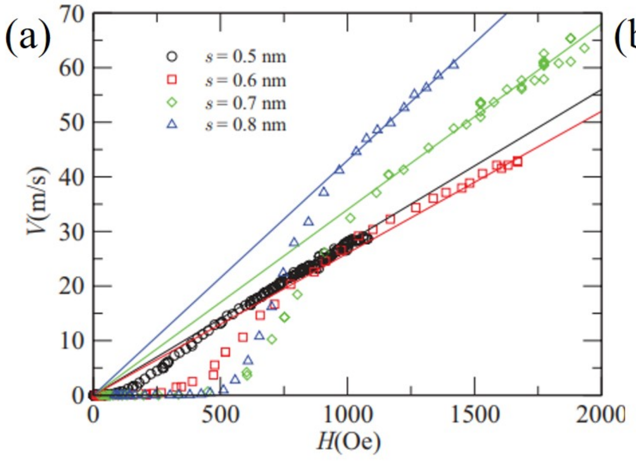

FIGURE 3.15 – (a) Experimental velocity-field curves for DWM in Co/Pt multilayers with PMA. Each curve corresponds to a different thickness for the Co layer, as indicated. Continuous lines represent linear fits to the fast-flow regime at large fields[175]. (b) Variation of DW velocity in Co/Pt multilayers with field for different temperatures with different regimes. Inset : Domain wall displacement (in black) from a nucleus (in red) produced by a 1 μs field pulse of H = 865 Oe at 150 K[174].

3.3 Mechanism of AO-HDS

In Section 3.1.3 we introduced the typical AHE behavior of AO-HDS, it is general that a fast jump followed by a slow relaxation in opposite direction happens to the Hall resistance when a pulse sent to the device. In this section, we will study the spin dynamics behind the AHE behavior, first, all the effects that exist from ultrafast demagnetization in femtosecond timescale to DWM in microsecond timescale will be concluded. Then we will try to resolve what are the dominant effects of the jumps and relaxations in different stages of switching.

3.3.1 Spin dynamics in different timescale

Figure 3.16 shows various dynamics occurring after a femtosecond laser pulse has excited on a ferromagnetic material in different timescale. First the photon field interacts with the electronics charges and spins, the angular momentum of light is been modified nonlinearly during the interaction in the first tens of femtoseconds. Then the dynamics of electrons and spins to thermalized populations takes place, leading to the fast demagnetization. All the mechanisms including electron-photon interactions[176], exchange interactions, spin-orbit interaction[177;178] and spin-flips[179] occur from the timescale of femto- to picosecond. From pico- to nanosecond timescale, the magnetization precession and damping or the propagation of magnons can be used to explain the dynamics with the help of LLG equation we have discussed in Section 1.2.

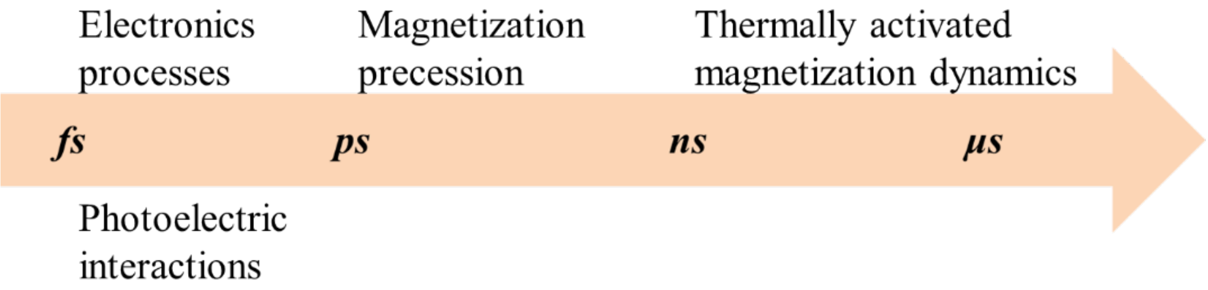

FIGURE 3.16 – The dynamics occurring after a femtosecond laser pulse has excited on a ferromagnetic material in different timescale.

In longer timescale, thermally activated magnetization process leads to different magnetization behavior like relaxation, DW nucleation and DW propagation, the dynamics considering the presence of temperature can be studied with the Kinetic Monte Carlo method, energy barrier calculations and the Arrhenius-Néel law. For the value of thermal energy comparable to the energy barrier, the magnetic system will become unstable and oscillate randomly, showing superparamagnetic properties. For the value of thermal energy smaller than the energy barrier, the magnetization will stay in a local minimum during precession and will surmount the energy crest which separates the two energy minima, appearing in the valley of another minimum eventually. This is then called thermally activated magnetization process or thermal activation, the study of thermal activation is very important because it is related to the thermal stability of a system in the application of magnetic technologies such as HDD[180], STT-MRAM[181] and racetrack memory[182]. The average time between two magnetization flips can be calculated by Arrhenius-Néel law :

$$\tau = \tau_0 \exp\left(\Delta E / k_B T\right) \tag{3.9}$$

Where ΔE is the energy barrier, and it is $\Delta E = KV$ in a Stoner-Wohlfarth particle with the uniaxial magnetic anisotropy constant K and the volume V. τ_0 is a constant and has a value between 10^{-9} s and 10^{-11} s in general. Taking Co particle at room temperature as an example, $K = 45\times10^4$ J/m^3, $\tau_0 = 10^{-9}$ s, $V = 2\times2\times2$ nm^3, a flip time of $\tau = 2.4$ ns is obtained. Some experimental results shows that the domain nucleation time is in the timescale of nanosecond[183–185].

Table 3.1 – Dynamics in different timescale after sending a σ^+ pulse to a M^- film.

Timescale	Effect	Behavior	Direction	R_H
0 - 10 ps	Ultrafast demag	Domain nucleation	M^- to 0	Jump
0 - 100 ps	IFE	DWM	M^- to M^+	Jump
100 ps - 20 μs	MCD	DWM	M^- to M^+	Relaxation
100 ps - 200 μs	Domain pressure	DWM	0 to M^-	Relaxation

In this work, we will focus on the domain nucleation and DWM by thermal activation in longer timescale, which could be the origin of AO-HDS. Table 3.1 lists the possible effects and their influence on the magnetization after a σ^+ circularly polarized pulse exciting on a M^- film. During the jumps, it can be easily understood that an ultrafast demagnetization occurs firstly in femtoseconds, followed by spin-lattice relaxation in picoseconds, it reaches to a quasi-equilibrium after several picoseconds, this process is no different to the typical ultrafast demagnetization phenomenon[42]. Meanwhile, owing to an effective magnetic field induced by the circularly polarized laser, the precession of the magnetization vector occurs under the IFE field in hundreds of picoseconds. To the best of our knowledge, there is no direct estimation for the lifetime of IFE field so far, Vahaplar *et al.* shows that the IFE field can persist in a magnetic metal longer than the laser duration by studying the THz yield of the metallic film excited by laser[94], Cornelissen el al. calculated the minimum duration of IFE field that needed to reproduce AO-HDS in Co/Pt multilayers based on the model of IFE[95]. Additionally, there is no evidence to prove that DWM generated by IFE field will stop as soon as the field disappears. But we have reason to believe that the DWM induced by IFE field has stopped in 2 μs after the excitation, otherwise the switching can be accomplished with only one pulse if assuming a filed-driven DWM of 1 m/s, however no helicity-dependent single-shot switching has been reported in Co/Pt multilayers yet. Hence, two effects are involved in the jumps, ultrafast demagnetization, ending up with random domain nucleation in the timescale of 10 ps, leads to a change of Hall resistance from -1 to 0, and of course, the demagnetization is helicity-dependent because of MCD. Also, IFE will introduce an effective field to nucleate some domains and push the DWs, the change of Hall resistance by this effect is from -1 to +1.

At longer timescale from nanosecond to microsecond, the relaxation is the DWM origin from three different effects : TG by MCD, TG by laser Gaussian distribution, and the domain pressure.

We have introduced the DWM driven by TG in the previous sections, we have verified that the DW will move to hotter region in our Co/Pt multilayers. In the relaxations, TG by the laser Gaussian distribution is pushing the DW to the center where it is the hottest, but this effect has actually no impact on the behavior of Hall resistance. First, because of the random nucleation of the jumps, the total magnetization would not change in average by pushing these random DWs to center. Second, our device is indeed very small compare to the size of laser beam, and no obvious TG is created especially when the laser is centered on the device.

On the other hand, the effect of MCD will create a temperature gradient across the DW because of the different absorption of two magnetization orientations, the $\boldsymbol{M}^{+}$ domain will have more absorption from σ^{-} light due to MCD, leading to higher temperature than the $\boldsymbol{M}^{-}$ domain. Thence the $\boldsymbol{M}^{+}$ domain will shrink brcause their DWs tend to move to the domain center where has the highest temperature, therefore, the Hall resistance is changing from -1 to +1 under such TG.

A magnetic bubble will shrink to smaller size spontaneously due to the DW surface tension[186]. According to the Laplace-Young equation[187], A pressure is introduced on the domain in order to minimize its surface energy, this pressure is given by $P_{\gamma} = \gamma / R$, Where γ is the energy per unit of the DW, R is the radius of domain. Hence, the smaller of the domain, the larger of the domain pressure. In our case, the laser nucleates lots of small domains in first several picoseconds, then these domains shrink and even disappear in the end spontaneously. This phenomenon is especially obvious in the early stage where more small domains are created due to MCD.

The Hall resistance response to the laser pulse shows very stochastic behavior even under an unchanging laser fluence because of the thermal fluctuation of the spin system, moreover, we are not able to keep the pulse energy exactly identical between pulses in the real measuring platform. In order to eliminate the error caused by this randomness and study the general rule of jumps and relaxations with magnetization, we repeat the switching measurement for 10 times for various fluence, the repetition rate is 5 kHz and the pulse number is 2000. Because each pulse will generate a jump follows by a relaxation, we extract the value of the jumps ΔM_{jump}, the relaxations $\Delta M_{relaxation}$ and note the initial magnetization of each pulse. The relationship between the jumps or the relaxations and their initial net magnetization under a typical fluence is displayed in figure 3.17, those smaller scatters present the behavior of each pulse and the larger scatters are the average of numerous tests, all the results are normalized.

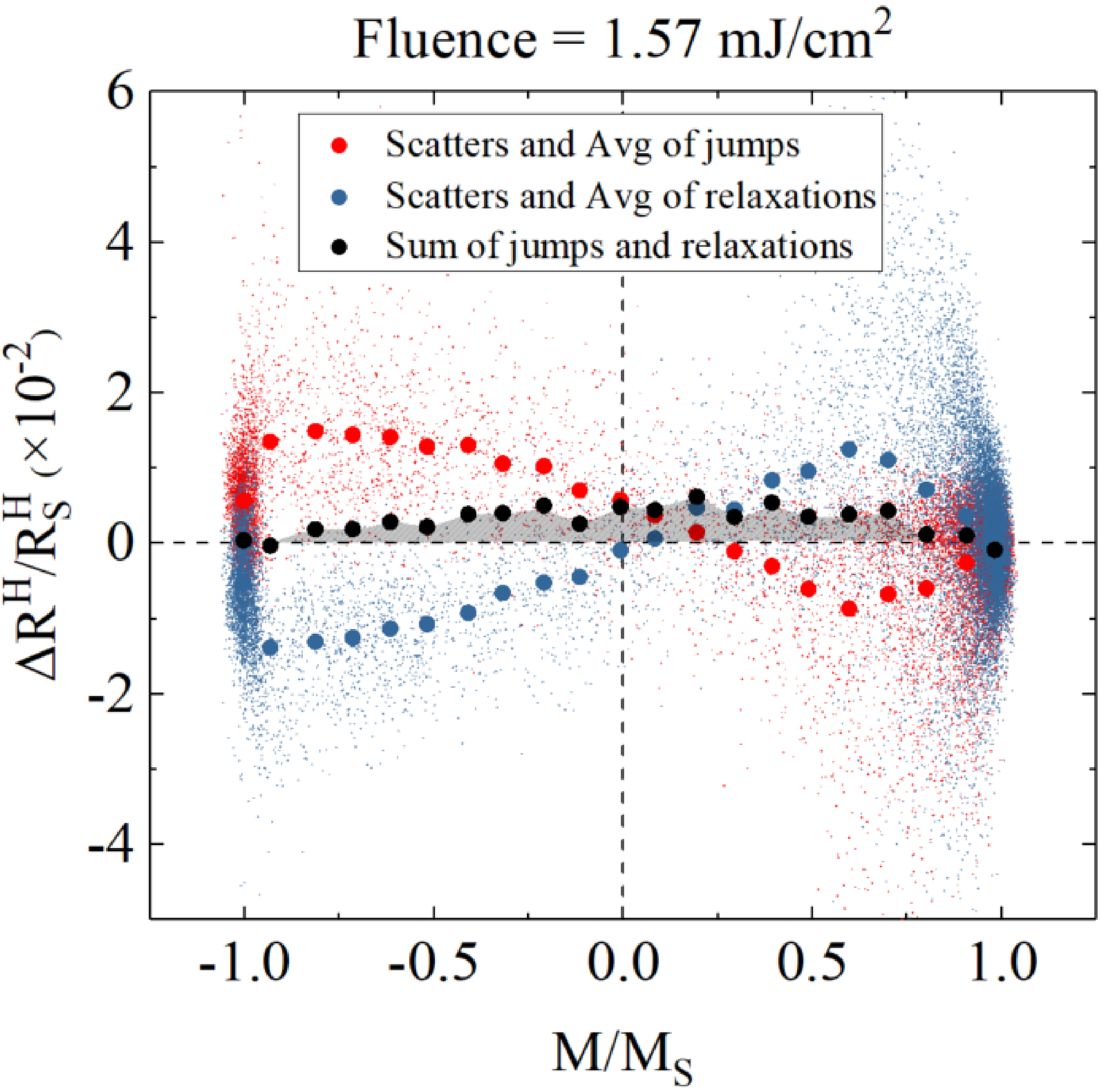

FIGURE 3.17 – The magnitude of jumps ΔM_{jump} and relaxations $\Delta M_{relaxation}$ varies with normalized net magnetization, the small scatters are the results of numerous tests and the large solid dots (red and blue) are the average of these measurements which are $\overline{\Delta M_{jump}}$ and $\overline{\Delta M_{relaxation}}$. The black dots are the sum of averaged jumps and relaxations $(\overline{\Delta M_{jump}} + \overline{\Delta M_{relaxation}})$, the shadow area indicates that the total contribution of jumps and relaxations accomplish the switching, the fluence for this measurement is 1.57 mJ/cm^2.

ΔM_{jump} are mostly positive at the beginning while the relaxations are negative, when about 50% of the magnetization is switched, the jumps contribute negative to the switching and $\Delta M_{relaxation}$ are positive. This result from extensive replicated tests confirms that what we observe from the trace in figure 3.8 is a general behavior, and we are able to conclude that the magnetization reversal is accomplished by the competition of these two contributions.

In the next sections, we will separately study the relationship of the jumps or the relaxations and the magnetization in different stage of switching, the dominant effects behind the jumps and the relaxation will be inferred and explained.

3.3.2 General mechanism

In this section, we will try to build a general mechanism about the involution of a magnetic system after exposed to a circularly polarized pulse in 200 μs, we will consider two different initial state : $\boldsymbol{M}^-$ state where the system is saturated to $\boldsymbol{M}^-$ direction and the net magnetization is -1, which is the typical state in stage 1, and multi-domain state where the some $\boldsymbol{M}^+$ domains are generated and the net magnetization is above 0, which is the typical state of stage 2.

In stage 1

The mechanism is schematically drawn in figure 3.18, when a $\boldsymbol{M}^-$ magnetic square is exposed to a laser pulse with different helicities, the magnetization response will experience two stages according to what has been observed in AHE measurement : the jumps which lasts for 2 μs approximately and the relaxations which lasts until the coming of next pulse, the timescale is read out from what we measured from the oscilloscope which cannot reveal the timescale of the laser induced spin dynamics precisely, but we will consider all the direct laser-induced effect only exists in the first 2 μs.

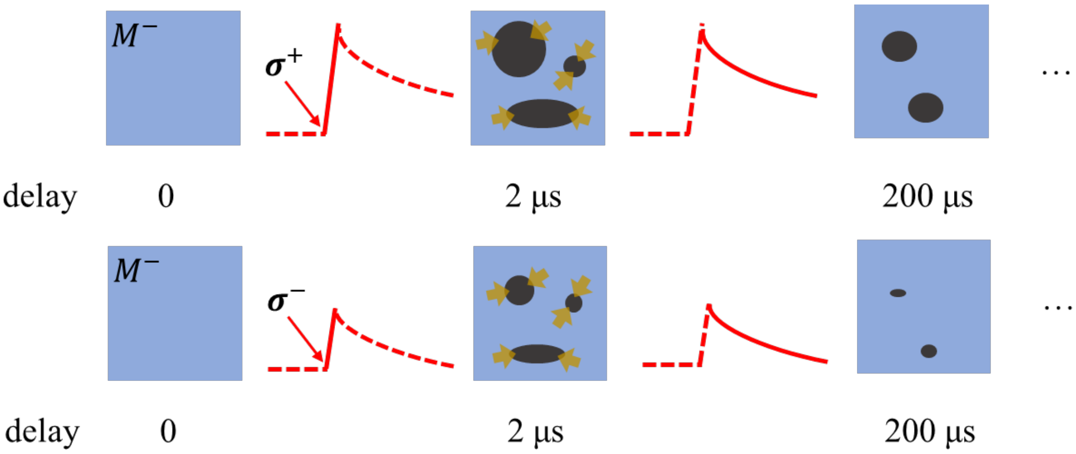

FIGURE 3.18 – Schematic representation of the nucleation and motion of DW in a $\boldsymbol{M}^-$ (blue) saturated film after exposing to a σ^+ or σ^- pulse, the generated $\boldsymbol{M}^+$ domain is in black, the red curve is the behavior of Hall resistance.

The ultrafast demagnetization ends up with the domain nucleation is mainly attributed to laser-induced transient heating in picosecond timescale, in this process, the MCD effect will result in the absorption difference between σ^+ and σ^- light, more domains will be generated from σ^+ pulse since the sample will elevate to higher temperature. After the domains are generated by σ^+ pulse, an effective filed due to IFE can generate the DWM which tends to expand those domains, whereas direction of the effective field by σ^- is opposite and the domains favor to shrink to $\boldsymbol{M}^-$. By considering all these effects contributing the net magnetization, it can be concluded that a σ^+ pulse will introduce a very fast and huge jump of net magnetization, while a σ^- pulse will introduce a relatively smaller one, as what we observed in Hall measurement. Additionally, it is reasonable that the IFE induced DWM disappears after 2 μs, otherwise AO-HDS can be easily realized with single pulse considering the DW velocity and lifetime of IFE. Therefore, $\Delta \boldsymbol{M}_{jump}$ is determined by the combination of pure thermal nucleation and its subsequent DWM by IFE, the helicity intervenes in the magnetic dynamics through a pure thermal and a non-thermal aspect respectively.

After 2 μs, lots of small and isolating domains are created, and the DWM with different origin leads to the relaxation. The first origin is TG by MCD, according to the 3TM mode, the spin, electron and lattice temperature will reach a quasi-equilibrium in picosecond timescale, but there is no evidence to prove how long the system temperature will relax to the room temperature, the temperature difference between two opposite domains may last for very long time. The $\boldsymbol{M}^-$ domain which absorbs more heat from σ^+ pulse becomes hotter, the DWM direction will be from $\boldsymbol{M}^+$ to $\boldsymbol{M}^-$ since the DW will move to hotter region in our sample, leading the expansion of $\boldsymbol{M}^+$ domain. The net magnetization changes by the TG driven DWM is opposite to the relaxation that we observed, because there is another driven force to generate a contrary DWM which is domain pressure. The domain shrinkage due to DW surface tension is very strong when the domain radius is small, leading to the relaxation of net magnetization. Besides, the shrinking effect exists in the whole lifetime of a domain, which is the origin of relaxation in 200 μs. In conclusion, $\Delta \boldsymbol{M}_{relaxation}$ is joint contributed by TG driven DWM and domain shrinkage, the latter is dominant to relaxation in stage 1 in our theory.

In stage 2

Now we consider the situation starts with multi-domain state exposed to σ^+ pulse in figure 3.19, assuming the net magnetization is above 0. Similarly, the jumps are initially resulted from the ultrafast demagnetization and domain nucleation by the laser-induced heating effect. Subsequently, IFE will try to move the DW in longer timescale after the domain nucleation. The direction of $\Delta \boldsymbol{M}_{jump}$ is determined by the total contribution of nucleation in $\boldsymbol{M}^+$ and $\boldsymbol{M}^-$ domains and the IFE driven DWM. The Hall resistance changes bring from IFE and nucleation in $\boldsymbol{M}^-$ domain is positive and that from nucleation in $\boldsymbol{M}^+$ domain is negative, therefore, $\Delta \boldsymbol{M}_{jump}$ is strongly related to the ratio of $\boldsymbol{M}^+$ and $\boldsymbol{M}^-$ area, which is net magnetization.

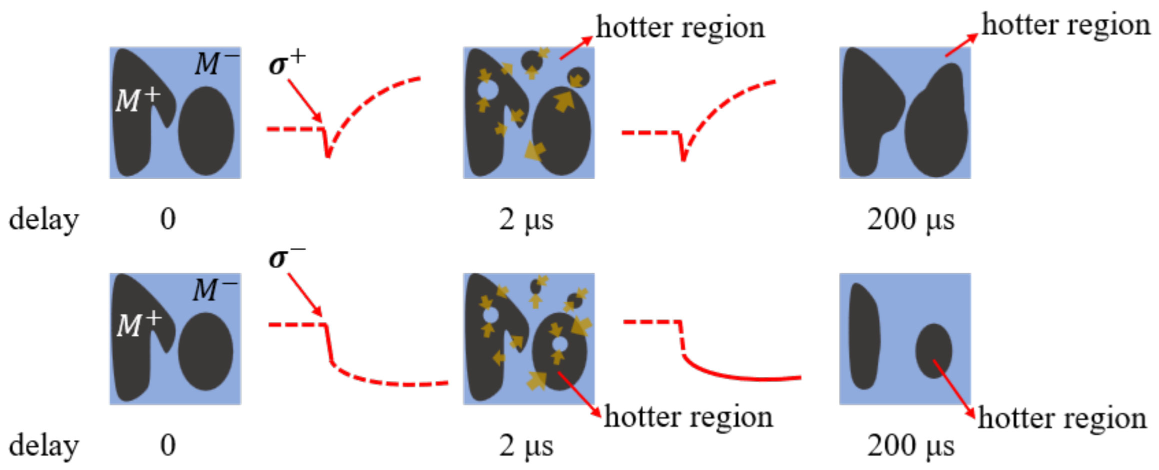

FIGURE 3.19 – Schematic representation of the nucleation and motion of DW in a film of multi-domain state after exposing to a σ^+ or σ^- pulse.

Figure 3.20 shows the relationship between ΔM_{jump} and net magnetization in stage 2, ΔM_{jump} is positive even when the magnetization is compensated because of the absorption difference by MCD, then the jumps of two magnetization with opposite direction are offset when the ratio of M^+ domains is slightly larger than that of M^- domains, and the magnitude of jumps will reach a maximum value when M/M$_S$ is 0.7 approximately. Further discussion to calculate the contributions to ΔM_{jump} will be presented in next section.

Likewise, after all the effects directly induced by laser pulse disappear in 2 μs, the DWM driven by domain pressure and TG is the origin of magnetization relaxation. Because both small M^+ and M^- domains are generated after the excitation in this case, the relaxation due to domain shrinking is compensated, besides, the domain pressure of those initial large domains contributes little to the relaxation considering their large domain radius or irregular shapes. Therefore, the domain pressure is not the origin of the directional relaxation in this stage. TG by MCD now takes the place, leading an obvious growth of M^+ domain and completing the switching after several pulses.

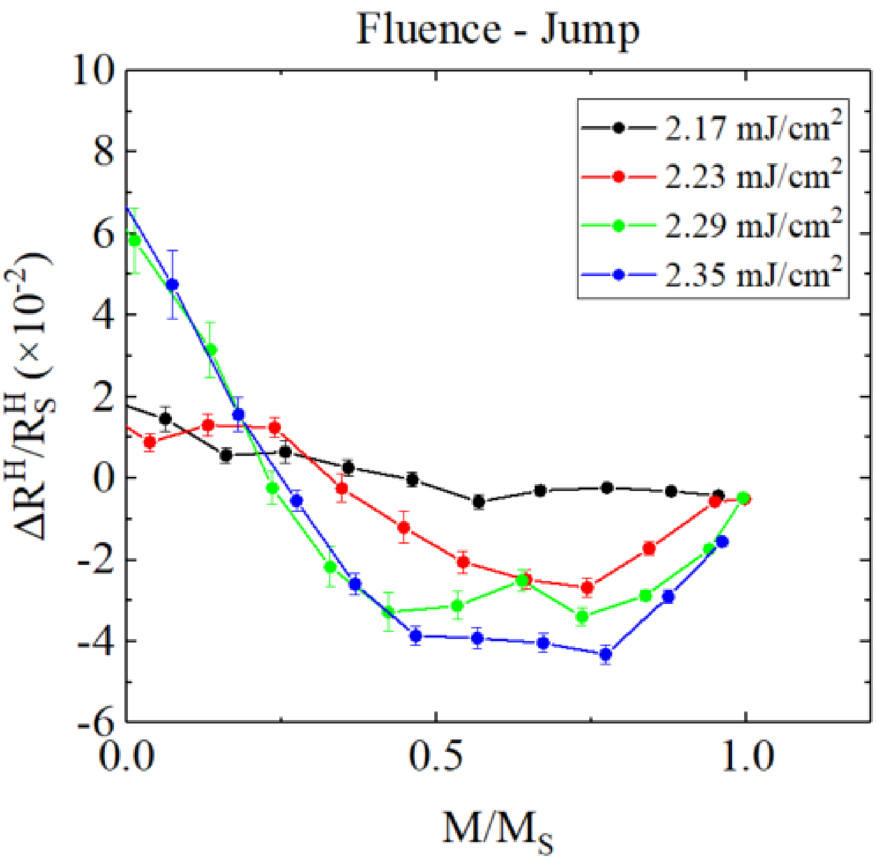

FIGURE 3.20 – ΔM_{jump} as a function of normalized net magnetization under various fluence in stage 2.

In this section, we came up with a model to explain the possible mechanism of AO-HDS, the dominant effects that leads to the behavior of net magnetization in different stages are suggested. In the following section, some experiment results will be shown to support the theory.

3.3.3 Resolving the jumps and the relaxations

Our model proposes that AO-HDS is accomplished by two steps : the domain nucleation leads to a multi-domain state in the stage 1, and the DWM leads to the domain growth in the stage 2. In this regime, the DWM also exists in the first stage but is not dominant, as well as the nucleation in stage 2. The Hall measurements indicate that the path to a complete reversal is the result of competition between jumps and relaxations.

The jumps

A jump of magnetization is the combination of domain nucleation and subsequent DWM by IFE in very short timescale, it can be described as :

$$\Delta M_{jump}^{(\sigma^+,M^-)} = \Delta M_{nuc}^{(\sigma^+,M^-)} + \Delta M_{IFE}^{(\sigma^+,M^-)} \tag{3.10}$$

$$\Delta M_{jump}^{(\sigma^-,M^-)} = \Delta M_{nuc}^{(\sigma^-,M^-)} - \Delta M_{IFE}^{(\sigma^-,M^-)} \tag{3.11}$$

ΔM_{nuc} refers to the magnetization change after nucleation and is helicity-dependent, considering M^- will absorb more heat from σ^+ light due to MCD, $\Delta M_{nuc}^{(\sigma^+,M^-)}$ is larger than $\Delta M_{nuc}^{(\sigma^-,M^-)}$. ΔM_{IFE} indicates the DWM by IFE which is also helicity-dependent, and light with opposite helicity will contribute to the net magnetization in the opposite direction.

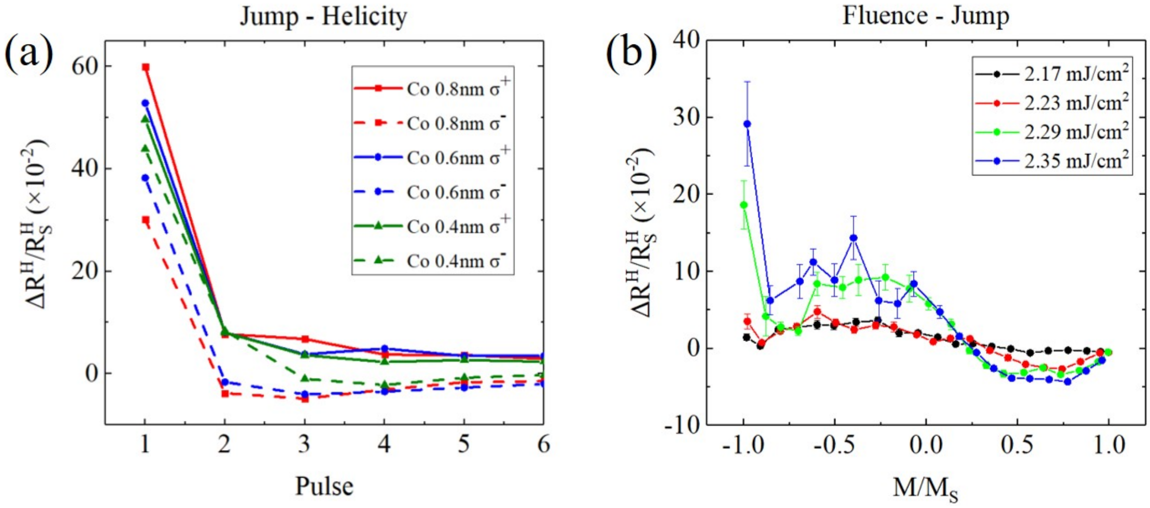

FIGURE 3.21 – (a) Changes of Hall resistance for the jumps at the first 6 pulses for samples with different Co thickness under the excitation of σ^+ and σ^- pulses, the fluences for three samples are different which is the one at their own least pulse number. (b) Evolution of the jumps with the net magnetization for various fluence.

Figure 3.21 (a) shows the magnitude of jumps ΔM_{jump} after each pulse for three samples with different Co thickness, the fluences used here are different for three samples and are corresponding to the least pulse number of each sample as we introduced in Section 3.1.2. ΔM_{jump} shows a huge difference for two helicities at the first pulse and $\left(\Delta M_{jump}^{(\sigma^+,M^-)} - \Delta M_{jump}^{(\sigma^-,M^-)}\right)$ increases with the Co thickness.

In order to resolve the contribution of MCD related nucleation and IFE induced DWM, we first measured the MCD of the three samples as shown in table 3.2 using a MCD spectrometer as introduced in Section 2.2.3, the calculation of MCD value refers from equation 2.6. MCD increases with the Co thickness but the value of MCD/t is almost the same for various thickness, indicating that the contribution of MCD related nucleation does not change much for different Co thickness. However, the role of IFE is significant different in the jumps, because the magnitude of IFE filed is independent to the sample, whereas the DW velocity by IFE is different for various samples under the same field. As reported by Bustingorry *et al.* in figure 3.15 : (a), the DW velocity is faster for the sample with thicker Co in a flow regime[175]. Considering the magnitude of IFE field (The effect of a 500 mJ/cm^2 and 200 fs laser pulse was found to be equivalent to an effective field of about 5 T[93]) and the temperature of sample in the jumps, the IFE induced DWM will work in the flow regime. Therefore, ΔM_{IFE} will be more obvious in the sample with thicker Co and $\left(\Delta M_{jump}^{(\sigma^-,M^-)} - \Delta M_{jump}^{(\sigma^+,M^-)}\right)$ is larger.

TABLE 3.2 – The total and different absorption to the right and left circularly polarized light for three samples. The MCD and MCD/t are calculated.

Co thickness t (nm)	0.4	0.6	0.8
A_{tot}(a.u.)	0.7347	0.7570	0.7549
ΔA (a.u.)	0.0013	0.0024	0.0031
MCD	0.18%	0.32%	0.41%
MCD/t (nm^{-1})	0.0045	0.0053	0.0051

Figure 3.21 (b) presented the relationship between $\Delta M_{jump}^{(\sigma^+,M^-)}$ and net magnetization, for a multi-domain state, it can be described as :

$$\Delta M_{jump}^{(\sigma^+)} = \left(\Delta M_{nuc}^{(\sigma^+,M^-)} + \Delta M_{IFE}^{(\sigma^+,M^-)}\right) - \left(\Delta M_{nuc}^{(\sigma^+,M^+)} - \Delta M_{IFE}^{(\sigma^+,M^+)}\right) \tag{3.12}$$

During the multi-shot induced process where the magnetization changes from M^- to M^+, with the decreasing (increasing) of the ratio of M^- (M^+) domain, $\Delta M_{jump}^{(\sigma^+)}$ is changing from positive to negative, but it does not follow a monotonic reduction from the experiments, because $\Delta M_{IFE}^{(\sigma^+,M^+)}$ is related to the total DW length which is very stochastic in various test.

The relaxations

The relaxation is mainly due to the DWM by different driven force : domain pressure and TG due to MCD. At the very beginning, we will firstly explain that the relaxation is not due to the recovery of the system temperature. In fact, the change of temperature T from 300 K to 350 K does not show significant impact on the Hall resistance of a magnetic square, normally the temperature of the sample has recovered below 350 K after 2 μs. As shown in figure 3.22, the samples still keep good PMA under 350 K, and the Hall resistance decreased by 0.66% which is relatively much smaller than the magnitude of the relaxations.

Therefore, only take the domain pressure and TG driven DWM into consideration, the change of magnetization in relaxation can be described as :

$$\Delta M_{relaxation}^{(\sigma^+,M^-)} = \Delta M_{pressure} + \Delta M_{TG}^{(\sigma^+,M^-)} \tag{3.13}$$

$$\Delta M_{relaxation}^{(\sigma^-,M^-)} = \Delta M_{pressure} - \Delta M_{TG}^{(\sigma^-,M^-)} \tag{3.14}$$

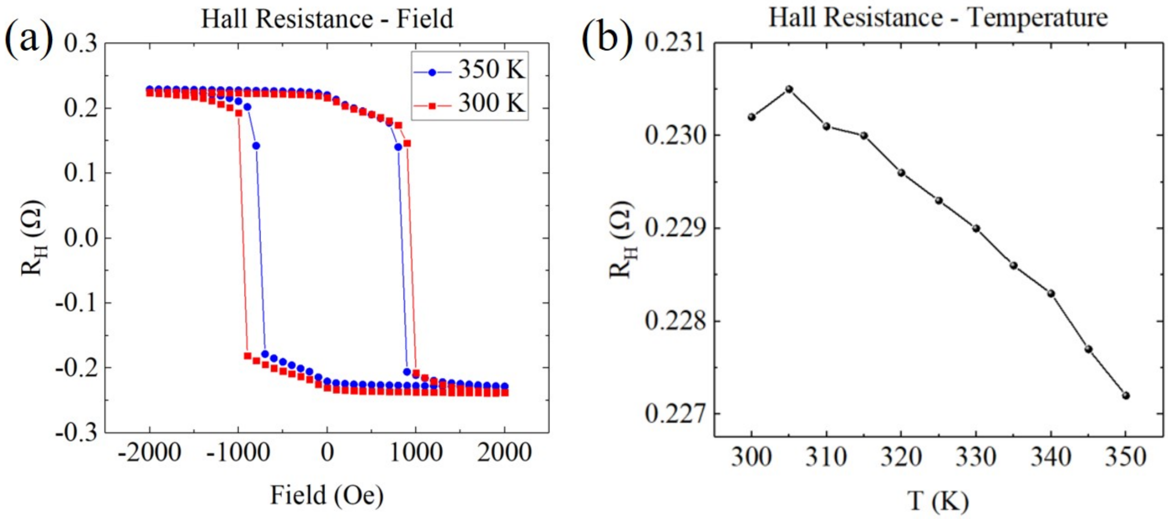

FIGURE 3.22 – (a) Loop of Hall resistance and Field under 300 K and 350 K. (b) Hall resistance decreases 0.66% from 300 K to 350 K which is relatively much smaller than the magnitude of the relaxations.

The domain pressure aways drive the system to the majority of the net magnetization M_{net} and is compensated when $M_{net} = 0$, additionally, $\Delta M_{pressure}$ is independent to the configuration of laser pulse and only related to the domain distribution. $\Delta M_{TG}^{(\sigma^+, M^-)}$ is helicity-dependent and tends to expand M^+ domain when exposed to σ^+ light, besides, $\Delta M_{TG}^{(\sigma^+, M^-)}$ is fluence dependent because different pulse fluence will induce different TG. For a system the magnitude of relaxation $\Delta M_{relaxation}^{(\sigma^+)}$ changes with its M_{net} during the multi-pulse switching process can be written as :

$$\Delta M_{relaxation}^{(\sigma^+)} = \Delta M_{pressure}(M_{net}, L) + \Delta M_{TG}^{(\sigma^+)}(F, M_{net}, L) \tag{3.15}$$

Where L is the DW length. The experimental result shows the relationship between $\Delta M_{relaxation}^{(\sigma^+)}$ and M_{net} under various fluence is plot in figure 3.23. In stage 1, lots of small domains are created and the domain shrinking effect is very strong, the creep regime of DW by domain pressure is dominant, therefore, the magnitude of $\Delta M_{relaxation}^{(\sigma^+)}$ is independent to the pulse fluence and the contribution of $\Delta M_{TG}^{(\sigma^+)}$ is negligible. In stage 2, the effect of TG driven DWM is obvious as shown in figure 3.23 (b), for laser with higher fluence, greater TG will be created leading to larger DW velocity. Hence, relaxation due to domain pressure is no more dominant, but TG driven DWM which is fluence dependent.

From the above results we are now able to conclude that the mechanism behind the AO-HDS is composed of two stages. In stage 1, the jumps are the result of domain nucleation and subsequent IFE driven DWM, the relaxations are the result of domain shrinkage, the jumps defeat the relaxations leading to a multi-domain state with zero net magnetization. In stage 2, domain nucleation and IFE driven DWM contribute the jump in opposite direction, leading to its negative and small magnitude, the relaxations mainly

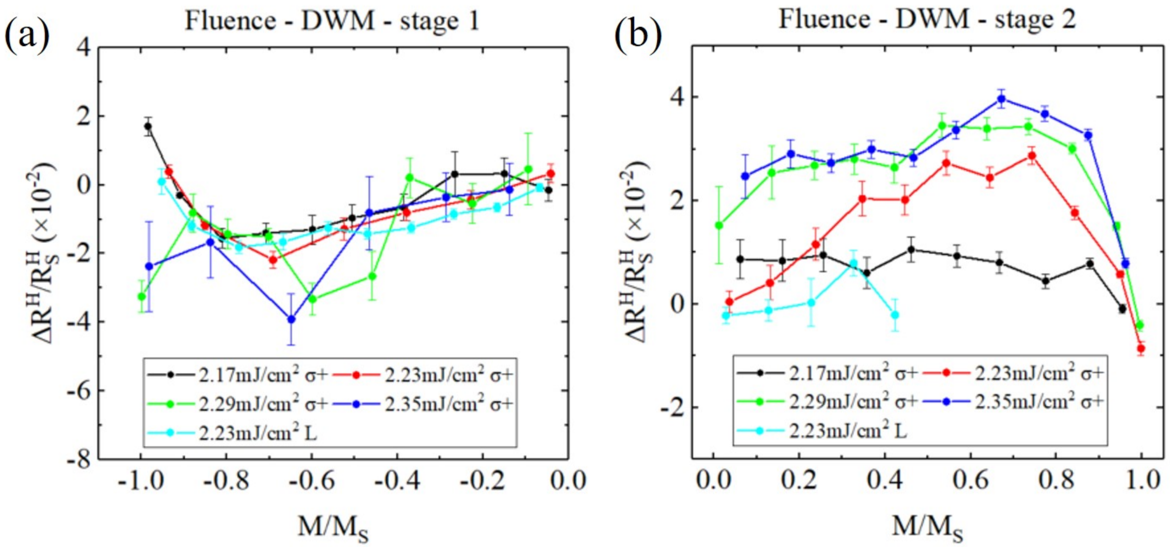

FIGURE 3.23 – Evolution of the relaxations with the net magnetization for various fluence (a) in stage 1 and (b) in stage 2.

contributed by TG driven DWM are greater than the jumps and help accomplishing the switching.

3.4 Conclusion

In this chapter, the phenomenon of AO-HDS has been shown and its properties related to the key parameters has been studied. The switching in a Co/Pt magnetic square is realized to study the spin dynamics during and after each pulse. Before studying the mechanism of AO-HDS, we introduced some methods of DW manipulation and laser induced spin dynamics of different timescale. A model has been suggested to reveal the mechanism, the switching is realized with the competition of the jumps and the relaxations, the jumps in stage 1 lead to a multi-domain state and the relaxations in stage 2 complete the switching. Some experimental results offer information about the dominant effect in the jumps and the relaxations. Firstly, the jump is the combination of laser induced domain nucleation and subsequent IFE induced DWM in short timescale, the behavior of samples with different thickness confirms the presence of both two effects. Then, the relaxation in stage 1 is mostly contributed by the domain shrinkage, whereas the TG driven DWM is the dominant effect in stage 2. As a result, AO-HDS is proceed via a rapid creation of a multi-domain state by the first few pulses that is followed by a much slower remagnetization by the lateral pulses, and accomplished as a result of the domain growth driven by MCD induced TG.

Considering that the jumps contribute negatively in stage 2 and the multi-domain-state can be accomplished through a pure thermal effect, we are able to suggest that TG induced DWM in stage 2 is the driving force of AO-HDS phenomenon. Some perspectives can be concluded after understanding the origin of AO-HDS. First of all, the two-step mechanism suggests that AO-HDS phenomenon is impossible to achieve by a single pulse. Secondly, the TG driven DWM property is important to increase the switching efficiency, a material system with large MCD and the DW can be easily moved under TG are expected to be switched with less pulses and lower laser power. Thirdly, changing the wave length of laser pulse to improve the MCD effect of the material would be another pathway to realize AO-HDS with less energy consumption.

Chapitre 4

AO-HIS in GdRCo alloys

In this chapter, we study the mechanism of AO-HIS in Gd-based RE-TM alloys. We have grown a series of samples according to the following structure : glass/Ta(5 nm)/Pt(3 nm)/$Gd_yR_{1-x-y}Co_x$(10 nm)/Pt(5 nm), where R = Dy, Tb, Ho as introduced in Chapter 2. Toggle magnetization reversal by femtosecond laser pulse has been observed in samples around RE-TM compensation point, even when the Gd concentration y is as low as 1.5%. Then, we will discuss the AO-HIS state diagrams for different elements concentration, by determining the magnetic configuration as a function of laser pulse duration and fluence. In the state diagrams, some key parameters F_{switch}, F_{multi}, τ_{max} are used to define the switching region. By studying the revolution of the parameters with elements concentration, some rule can be revealed to better understanding the mechanism of AO-HIS, as well as to identify the ideal material and beam parameters for AOS devices from the aspect of energy efficiency and system stability.

4.1 Single-shot AO-HIS in $Gd_yR_{1-x-y}Co_x$ alloys

4.1.1 AO-HIS in samples with various elements concentration

Unlike AO-HDS in Co/Pt multilayers discussed in Chapter 3, AO-HIS is a single-shot phenomenon and thus only laser fluence and pulse duration need to be considered to generate a switching. The state diagram showing the magnetic state after laser irradiation under various pulse fluence and duration in GdCo alloy has already been well studied[13]. As shown in in figure 4.1, by defining the magnetic state after the exposure as : "no switching", "switching" and "multi-domain state", a switching window of fluence which decreases with the pulse duration can be obtained. The critical fluence from "no switching" to "switching" is defined as F_{switch} and that from "switching" to "multi-domain state" is F_{multi}. When the laser fluence used is lower than F_{switch}, there is no response for the magnetic state, it corresponds to the white region in figure 4.1. As is indicated by the grey region, the multi-domain state will appear once the laser fluence is above a given value F_{multi}. F_{switch} follows a linear relationship at a slope k when increasing the pulse duration, whereas F_{multi} keeps almost constant. As a result, a triangle area is formed in state diagram (pink area in figure 4.1), the minimum pulse duration τ used in this work is 50 fs, at which the widest laser fluences window allowing for magnetization switching is obtained. When increasing τ until $F_{switch} = F_{multi}$, AO-HIS can no longer be observed at whichever the fluence, we define the pulse duration currently as the maximum pulse duration τ_{max}. In conclusion, three key parameters of F_{switch}, F_{multi}, τ_{max} define the switching area in the state diagram of AO-HIS.

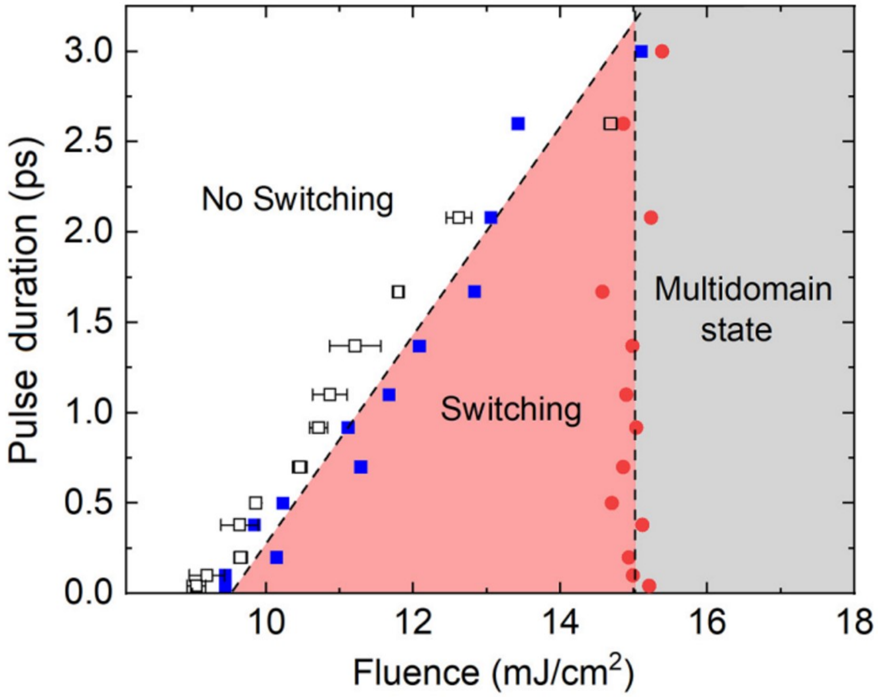

FIGURE 4.1 – AO-HIS state diagram of a 20-nm $Gd_{24}(FeCo)_{76}$ film : switching fluence F_{switch} (open black square and full blue square) and multi-domain fluence F_{multi} (full red dot) as a function of the pulse duration.[13]

The switching behaviors and the state diagrams in GdRCo alloys are not much different from that in GdCo alloys. The AOS system as introduced in Section 2.3.2 is employed to observe the switching phenomenon of these alloys, most of the samples, especially those closing to the RE-TM compensation point, present standard AO-HIS switching phenomenon.

Firstly, we focus on the samples for a certain Co concentration, i.e., $Gd_yTb_{1-x-y}Co_x$ with x = 74%, while y varies from 1.5% to 23%. Figure 4.2 shows the MOKE images after 5-subsequent laser pulses with laser fluence F = 1.7 mJ/cm^2, the film is initially saturated via external field before exposure. The magnetization can be reversed after shining the first laser pulse, and it will be restored after the second one. As a result, the magnetic configurations after an odd (even) number of pulses will be the same as the one after the first (second) pulse. The magnetic moments show deterministic toggle switching upon irradiation with a single laser pulse. Interestingly, the deterministic reversal is achieved even when the concentration of Gd is as low as 1.5% (as much as 24.5% of Tb). Moreover, the toggle magnetization switching is also recorded in $GdDyCo_{72}$ and $GdHoCo_{72}$ alloys.

But of course, no switching can be observed after exposed to femtosecond pulse for samples whose Gd concentration is 0%, apart from thermal demagnetization, leading to a multi-domain state.

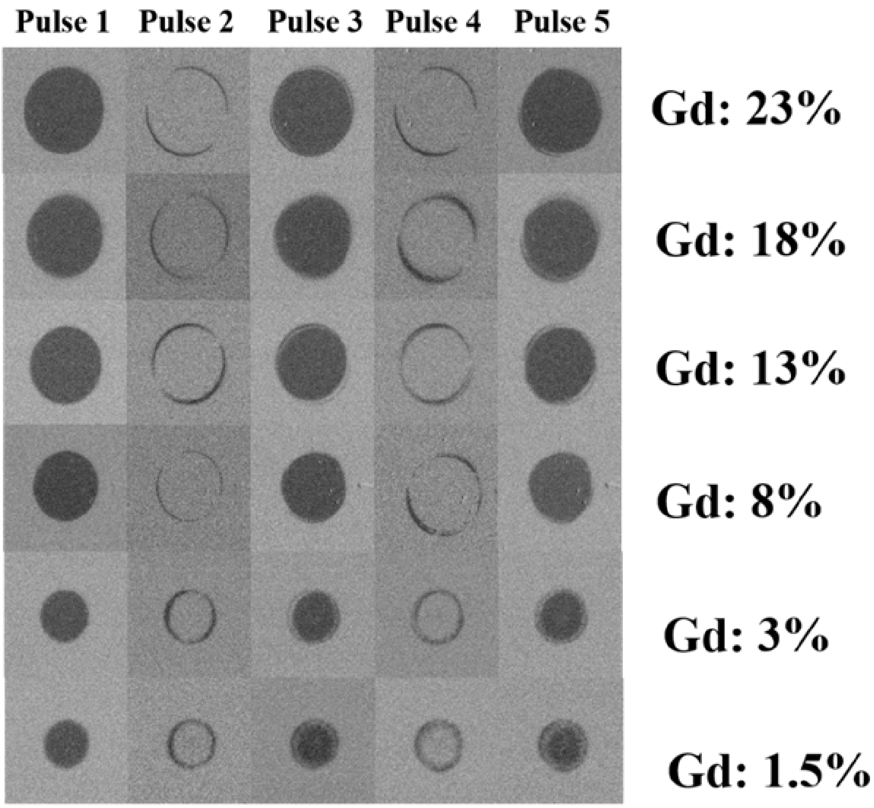

FIGURE 4.2 – MOKE images of $Gd_yTb_{1-x-y}Co_x$ alloys with x = 74%, y varying from 1.5% to 23%, after exposure to a single linearly polarized laser pulse with a pulse duration of 50 fs, the laser fluence is fixed at 1.7 mJ/cm^2.

After evaluating the switching properties of all the samples, the mapping of magnetic state after laser excitation in GdTbCo alloys with various elements concentration is built as shown in figure 4.3, samples who is close to its RE-TM compensation point x_{comp} possess AO-HIS (x_{comp} = 76% in TbCo and x_{comp} = 76.5% in GdCo), and the number of samples exhibiting AO-HIS increases with the Gd concentration y, alternatively, the minimum value of y has to be increased gradually to observe the switching when Co concentration x is far away from x_{comp}. Unfortunately, the composition range for pure GdCo with PMA is so narrow that we are not able to prove that pure GdCo alloys has the widest range of composition showing AO-HIS. The reason why GdCo alloys maintain PMA easier after doping Tb is from the zero spin-orbit coupling of Gd[188], the presence of RE ions with a strong spin-orbit coupling such as Tb, Dy and Ho give rise to much larger uniaxial magnetic anisotropy K_u as compared to Gd.

The similar law of behavior is presented in GdDyCo and GdHoCo alloys as shown in figure 4.4, AO-HIS can be realized in RE-TM alloys even when the Gd concentration is as

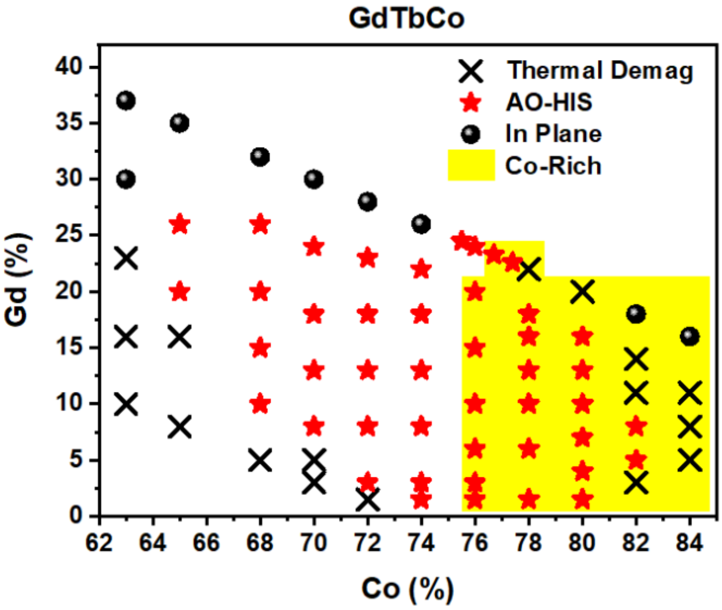

FIGURE 4.3 – The mapping of elements concentration and magnetic states after laser excitation for GdTbCo.

low as 1.5% when the magnetization of RE and TM is almost compensated (Co takes 73% in GdDyCo and 69% in GdHoCo respectively). So, we propose that one GdRCo sample whose concentration is closer to the compensation point is easier to show AO-HIS, and the amount of Gd is less needed.

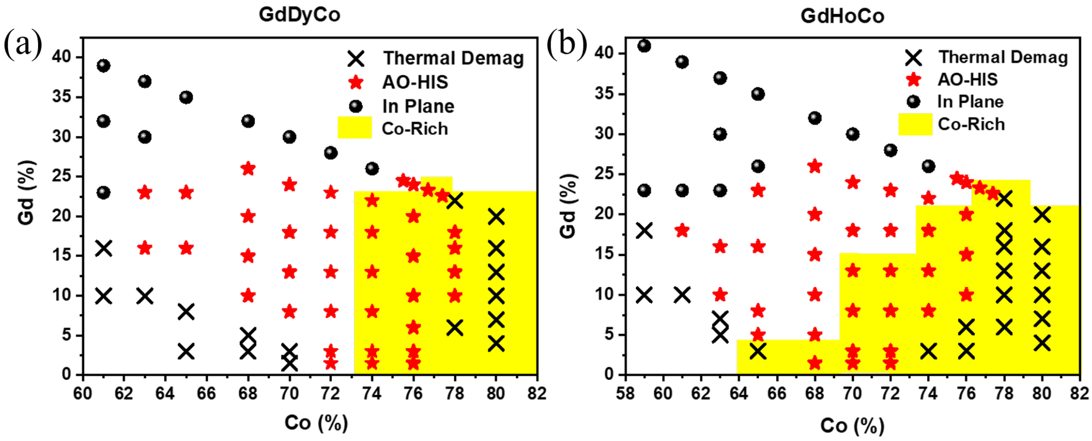

FIGURE 4.4 – The mappings of elements concentration and magnetic states after laser excitation for (a) GdDyCo and (b) GdHoCo.

4.1.2 Possible origins

From what have observed in GdRCo alloys, two general laws can be concluded that AO-HIS can be presented in a RE-TM material : firstly, Gd is indispensable but very low Gd concentration is sufficient ; secondly, the least Gd will be needed for AO-HIS at the compensation point of RE-TM alloys. There have been many discussions what is the particularity of Gd[23;189;190] and why AO-HIS is lost when away from the compensation point[16;19;191].

Gilbert damping

A significant difference between Gd and the rest three elements is that Gd has zero orbital angular momentum, leading to weak PMA and very small magnetic damping in GdCo[192–194]. The Gilbert damping factor in RE-TM alloys can be evaluated by measuring the ultrafast demagnetizing dynamics under various external field through TR-MOKE. The effective damping constant α_{eff}, which is the combination of Gilbert damping and external damping, follows an approximate relation :

$$\alpha_{eff} = 1/\left(2\pi f \tau\right) \tag{4.1}$$

Where f and τ represent the precession frequency and relaxation time respectively. When the external field is strong enough, α_{eff} can be considered as the intrinsic damping constant α_0 as the external damping is relatively small.

But the role of damping parameter in AO-HIS is still under debate[23]. On the one hand, according to previous reports, the Gilbert damping of RE-TM alloys would be diverged near the compensation point[19;23;190–195]. Usually, a larger damping is accompanied by a larger amount of spin angular momentum transfer. Therefore, it will facilitate the reverse of the magnetic moments by exchanging more angular momentum between different sublattices.

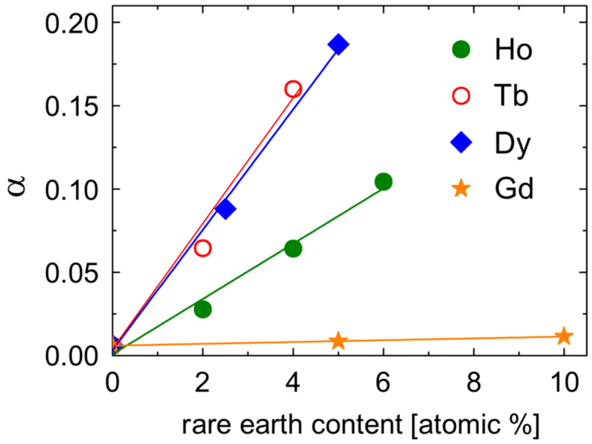

FIGURE 4.5 – Damping parameter α as function of the RE concentration in RE-doped $Ni_{80}Fe_{20}$ films.[194]

On the other hand, α_{eff} is decreased when doping Gd into RCo. Figure 4.5 shows the damping constant α_0 as a function of the RE concentration in RE-doped $Ni_{80}Fe_{20}$ films[194], in this work α_0 increase linearly with the RE content. Dy and Tb have similar slope and increase fastest with increasing the content, because Gd has no orbital angular momentum, the variation of its damping constant is ignorable. Therefore, low damping parameter of Gd could be one of the conditions for AO-HIS.

Based on our observation, two necessary conditions for AO-HIS are the presence of Gd and nearing to the compensation point of RE-TM, but the low damping in Gd-based material and the high damping at the compensation point form a contradiction. More work needed to be done to understand the role of damping and other effects from magnetization dynamics and compensation or Curie temperature in AO-HIS.

Spin-lattice coupling

Another possible reason might be various spin-lattice coupling between Gd and other REs. In an early work of this manuscript[196], we suggested a phenomenological mechanism to understand the role of spin-lattice coupling in the presence of switching. The mechanism is shown in figure 4.6, firstly, the $3d$ and $5d$ delocalized electrons stemming from TM and RE are excited to nonequilibrium, because the $5d$ electrons in RE metals carry only very small magnetic moments (0.55 μ_B in Gd and 0.34 μ_B in Tb for instance), a pronounced variation of ultrafast demagnetization time will not be expected for TbCo and GdCo in this stage. Most of the magnetism in Gd and Tb comes from the deeply buried $4f$ localized electrons which can not be directly excited by photon energy of 1.5 eV. In the following picoseconds, the intersublattice $3d$-$5d6s$-$4f$ exchange coupling serves as a bridge to transfer spin angular momentum between RE and TM sublattices. For Tb, this bridge has to competes with another channel which is the transfer of spin angular momentum from $4f$ electrons to the lattice due to its strong spin-orbit coupling. However, this channel is blocked in Gd due to its zero orbital momentum, therefore, the spin angular momentum transfer between Gd and Co is more efficient and favored. Such mechanism based on the spin-lattice coupling may explain the importance of Gd in AO-HIS.

To explain such mechanism, we engineered $Gd_{1-x-y}Tb_yCo_x$ alloys and investigated the influence of elements concentration on the spin dynamics. The ultrafast demagnetization of GdTbCo alloy taking place in femto-second timescale is found to be independent of Tb concentration, whereas the TR-MOKE signal measured at 10 ps after the excitation decreases with increasing the Tb concentration when AO-HIS occurs. The results agree with the theory that spin angular momentum can be transferred from Gd to Co resulting in the magnetization switching, whereas the angular momentum is dissipated through the lattice its strong spin-orbit coupling for Tb. This work highlights the role of spin-lattice coupling in AO-HIS and the specialty of Gd, but the quantitative estimation on the dissipation from spin to lattice in Gd and Tb is important to support the mechanism, because we are able to observe AO-HIS when Gd concentration is as low as 1.5%, which indicating a huge variation of angular momentum transfer between Gd-Co and Tb-Co.

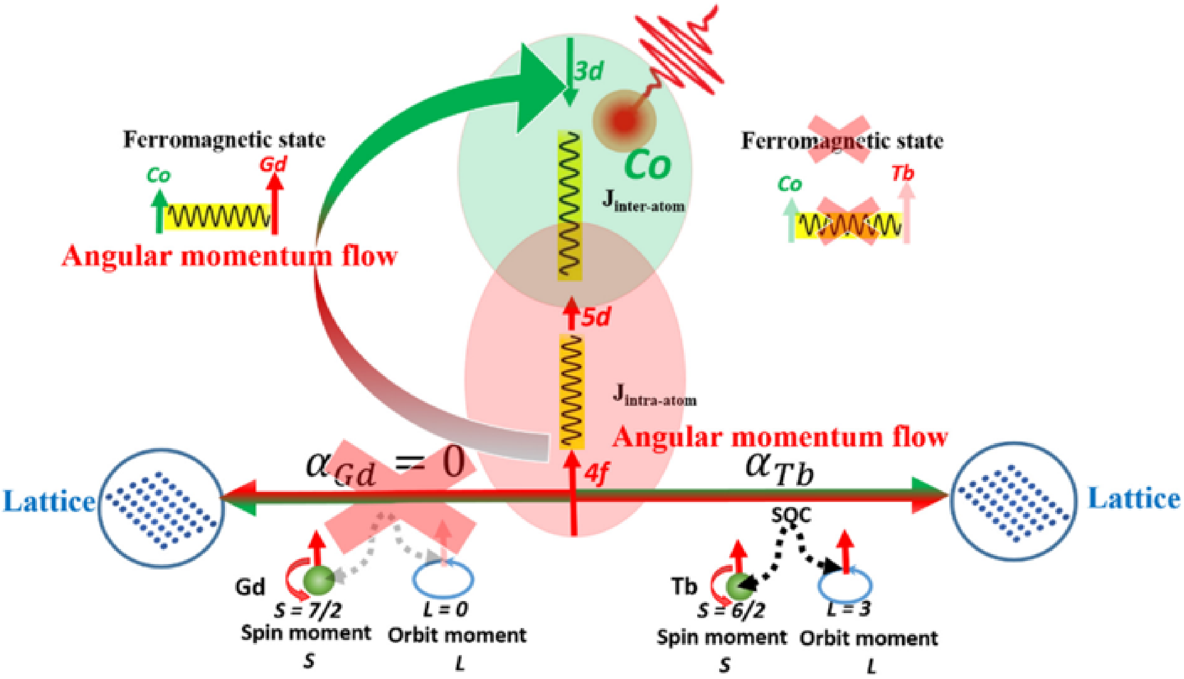

FIGURE 4.6 – Illustration for spin angular momentum dissipation process in GdTbCo alloys after the excitation of laser pulse. The photon interacts with delocalized d electrons directly in the first time. Two processes responsible for spin angular momentum dissipation are categorized. Firstly, spin angular momentum can be dissipated by lattice and strongly related the orbital quantum number L, this channel is almost closed in Gd due to its zero orbit moment, whereas it is very strong in Tb. Secondly, the interaction between RE and TM facilitated by intra-atomic exchange energy provides another channel for spin angular momentum transfer.[196]

4.2 State disgram as a function of elements concentration

4.2.1 General behavior

The state diagram of pulse duration and fluence in GdCo conveys many information on AO-HIS, the switching fluence F_{switch} corresponds the minimum energy needed for angular momentum transfer between RE and TM, while the F_{multi} is related to the Curie temperature T_C of material, the maximum pulse duration τ_{max} which defines the intersection of F_{switch} and F_{multi} is a key parameter for future engineering application of AOS spintronic device. We therefore measure the state diagram in GdRCo to study these parameters change with elements concentration.

Starting from the sample $Gd_{23}Dy_5Co_{72}$ film, in which a large amount of Gd guarantees a relatively large fluence window showing AO-HIS, its state diagram is shown in figure

4.7, the grey triangle area is formed in the state diagram to show AO-HIS, the behavior is similar to that of GdCo alloy. F_{switch} linearly increases with pulse duration at a slope of k while F_{multi} keeps almost constant. The minimum pulse duration is 50 fs, at which the widest fluences window allowing for magnetization switching is obtained. When $F_{switch} = F_{multi}$, τ_{max} above which the AO-HIS cannot be observed is 5 ps.

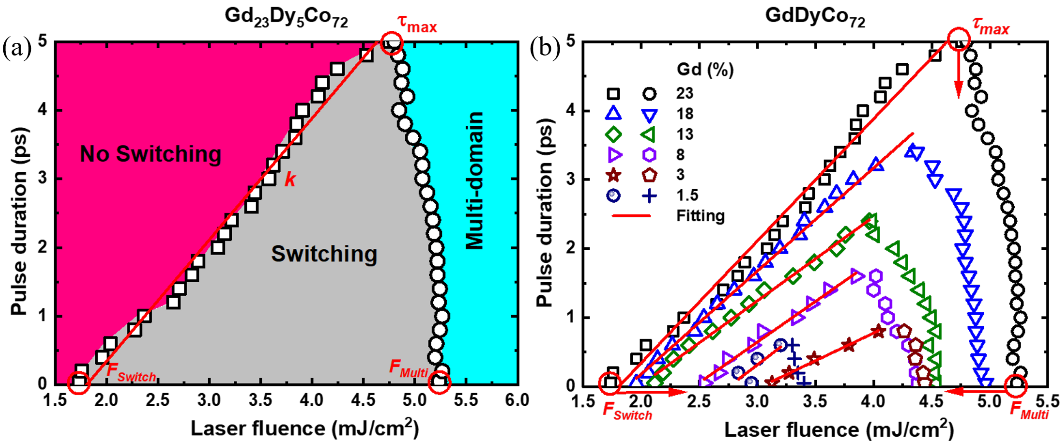

FIGURE 4.7 – (a) The state diagram of $Gd_{23}Dy_5Co_{72}$ alloy : switching fluence F_{switch} (open black square) and multi-domain fluence F_{multi} (open black dot) as a function of the pulse duration. Three regions were divided by F_{switch} and F_{multi} : switching, no switching, and multi-domain states. (b) The evolution of the shape of state diagrams by changing the Gd concentrations in $GdDyCo_{72}$.

Subsequently, the evolution of the state diagram is shown in figure 4.8 (b) by changing the Gd concentration y (as well as the Dy concentration) in GdDyCo, when x is fixed at 72%. It is clearly seen that the area of AO-HIS becomes smaller due to the change of F_{switch}, F_{multi}, τ_{max} and k, although all the samples share the similar behaviors. For the parameters of F_{switch}, F_{multi}, and τ_{max}, the red arrows are used to point the directions where they move because of the reduction of Gd contents.

Figure 4.8 quantitatively present the evolution of the above parameters as a function of the Gd (Dy) concentrations derived from the state diagrams in figure 4.7 (b). For a certain pulse duration, $\tau = 50\ fs$ in figure 4.8, F_{switch} decreases and F_{multi} increases with more Gd. Meanwhile, τ_{max} shown in figure 4.7 (b) increases from 0.6 ps to 5 ps when the concentration of Gd is increased from 1.5% to 23%. The evolution of slope k depends on the other three parameters F_{switch}, F_{multi}, τ_{max}. Due to the triangle shape of the state diagram, k will become larger when τ_{max}, F_{switch} is increased, or F_{multi} is decreased. Here, by doping more Gd, we found that F_{switch} is decreased and F_{multi} is increased. This will lead to a smaller slope k if we do not consider the change of τ_{max}, disagreeing with the fact that figure 4.8 shows a larger k with more Gd. As a result, the increased k with more Gd concentration is mainly ascribed to the increase of τ_{max}.

Meanwhile, in figure 4.9, we plot the evolution of the shape of state diagrams as

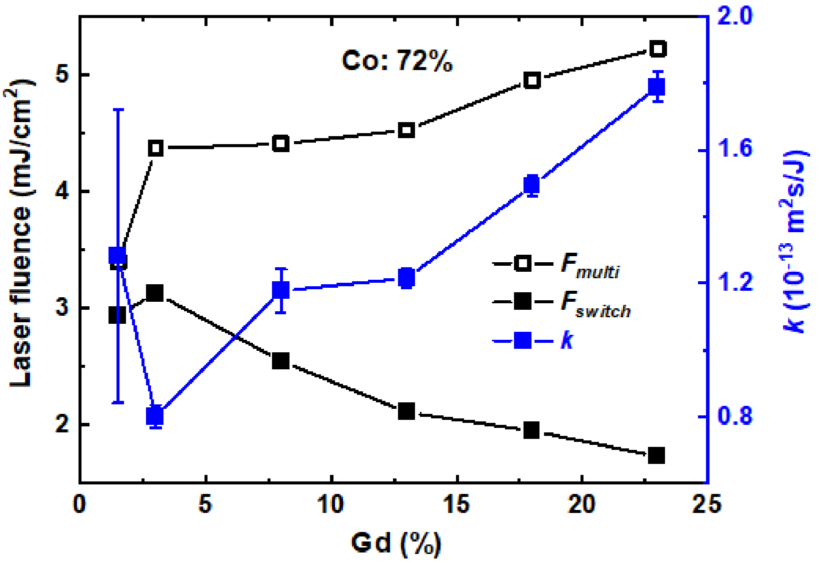

FIGURE 4.8 – The parameters of F_{switch}, F_{multi} and k as a function of Gd concentrations in $GdDyCo_{72}$.

a function of Co concentrations, when Gd and Dy contents are fixed at 18% and 13% respectively, respectively. Co content shows more significant influence on F_{multi} but almost no impact on F_{switch}. Samples with higher Co content possess higher F_{multi} which can be understood from the higher T_C in rich Co samples. F_{switch} increases with the Co content but not significantly, and k decreases with the Co content. In the following section, more results will be discussed to study the relationship between key parameters and elements concentration.

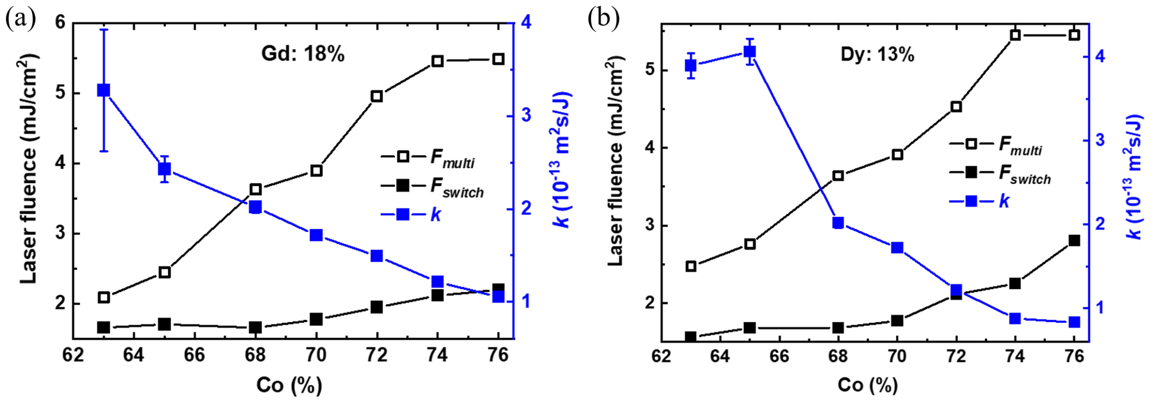

FIGURE 4.9 – The parameters of F_{switch}, F_{multi} and k as a function of Co concentrations in (a) $Gd_{18}DyCo$ and (b) $GdDy_{13}Co$ alloys.

4.2.2 Key parameters

Indeed, the study on parameters of F_{switch}, F_{multi}, τ_{max} helps for the engineering application of AOS devices. F_{switch} is related to the power consumption of the writing operation of a MRAM device, F_{multi} represents the thermal stability of data storage to prevent the magnetization from breaking into magnetic domains, enlarging the gap between F_{switch} and F_{multi} reduces the possibility of error operation and improve the robustness of the system. τ_{max} is the real limitation of the application of AOS, extending τ_{max} to nanosecond timescale helps the AOS device being integrated with a compact semiconductor laser and optical waveguide, rather than a complicate femtosecond laser system using mode locking technology[197;198].

To gain a quantitative insight on the details of the dependence of AO-HIS on elements concentrations, we show the F_{switch}, F_{multi}, τ_{max} and k mapping of $\mathrm{Gd}_y\mathrm{Dy}_{1-x-y}\mathrm{Co}_x$, in figure 4.10, respectively, for different concentrations of Co and Gd (Dy). All the parameters measured from the AO-HIS experiments using 50 fs pulse duration. Rules can be found by fixing one of elements concentration, for the next section, we will discuss the revolution of the four parameters in the mapping respectively.

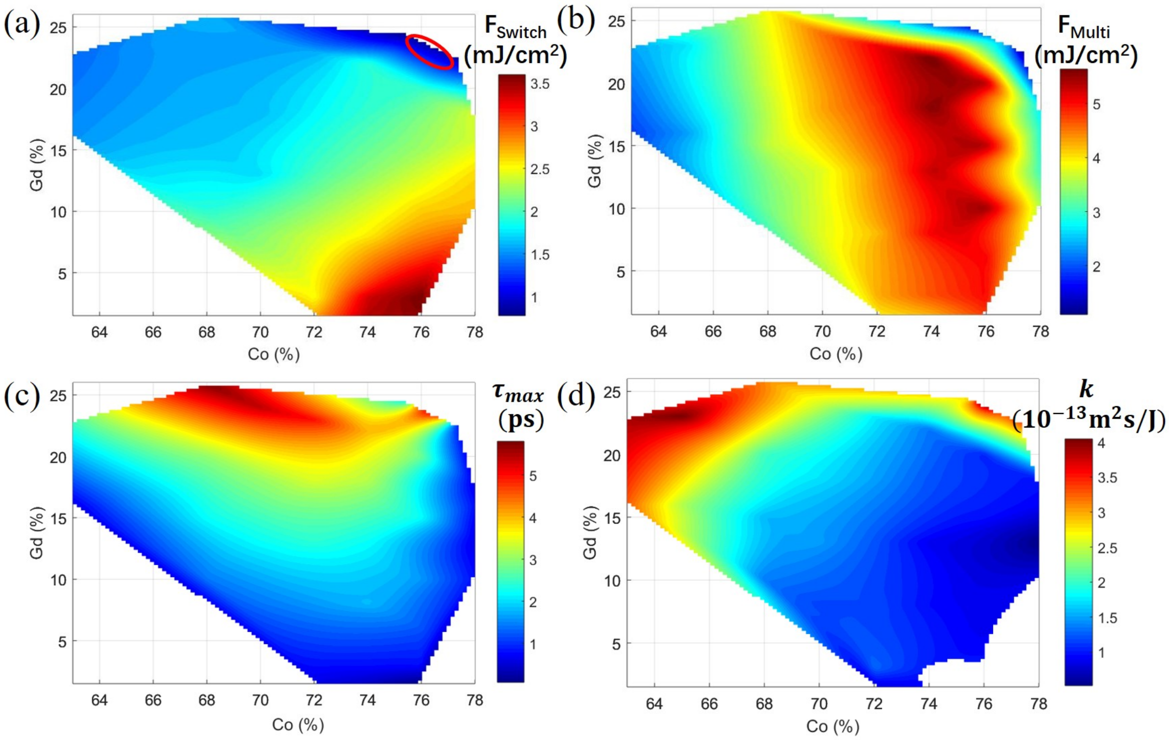

FIGURE 4.10 – Mapping of laser parameters allowing for magnetization switching in GdDyCo alloys, including (a) F_{switch}, (b) F_{multi}, (c) τ_{max} and (d) k, which is defined as threshold laser fluence for switching, multidomain state, the maximum pulse duration to observe AO-HIS and the slope k describing the dependence of F_{switch} on pulse duration, respectively.

Switching fluence

From the mapping of F_{switch} in in figure 4.10 (a), we can see that it depends on both the concentrations of Co and Gd. The trend of F_{switch} of all the samples is shown in figure 4.11, taking GdTbCo as an example, for certain Co content, F_{switch} becomes larger with less Gd (more Tb). Meanwhile, by fixing Gd concentration, it can be seen that more Co leads to larger value of F_{switch}. The results for a few samples without doping Dy are also shown at the highlighted area in figure 4.10 (a), from which one can see these samples own the smallest F_{switch}. It suggests the laser fluence needed to observe the AO-HIS has to be increased once the other rare-earth element is doped into a pure GdCo alloy. For Dy-doping and Ho-doping GdCo, similar behavior of F_{switch} is demonstrated in figure 4.11(b-c). Additionally, among three sample series, F_{switch} of GdTbCo alloys is the largest and that of GdHoCo is the smallest in general (following the order of T$_C$ of three elements), indicating the system T$_C$ could also be a factor impacting F_{switch}. Therefore, a general conclusion to lowing the switching fluence in Gd-based RE-TM is to increase the Gd concentration and decrease the system T_C.

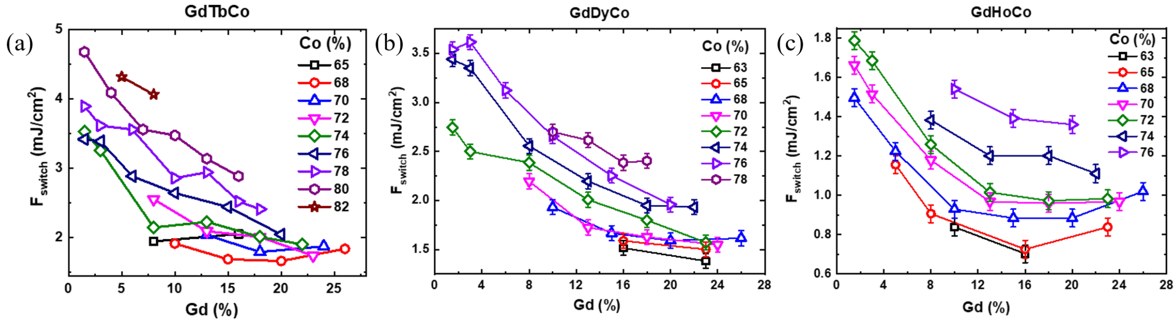

FIGURE 4.11 – F_{switch} as a function of Gd concentration in (a) GdTbCo, (b) GdDyCo and (c) GdHoCo with various Co concentration. Similar trend is shown of three material series, F_{switch} decrease with Gd concentration while increase with Co concentration. The average F_{switch} in GdHoCo is the lowest while in GdTbCo is the highest, the lowest F_{switch} is 0.7 mJ/cm^2 in $Gd_{16}Ho_{21}Co_{63}$ among all the samples that we have grown.

Wei *et al.* reported F_{switch} as a function of Gd concentration in pure GdFeCo as shown in figure 4.12[13], F_{switch} reaches a minimum value when the concentration of Gd is 32%. Because decreasing the Gd concentration reduces F_{switch} while TM concentration has opposite impact, the tradeoff of these two leading to the V-shape function. Some previous works suggested that minimum F_{switch} is shown around the compensation point of GdCo[13;22]. However, for the samples of GdTbCo alloy, because the compensation points of GdCo and TbCo are very close (around 24% of RE) in our sample, the minimum F_{switch} is found at Co 68% as shown in figure 4.11 (a) which is very far away from the compensation point. Therefore, no relationship between the minimum F_{switch} and compensation point can be concluded.

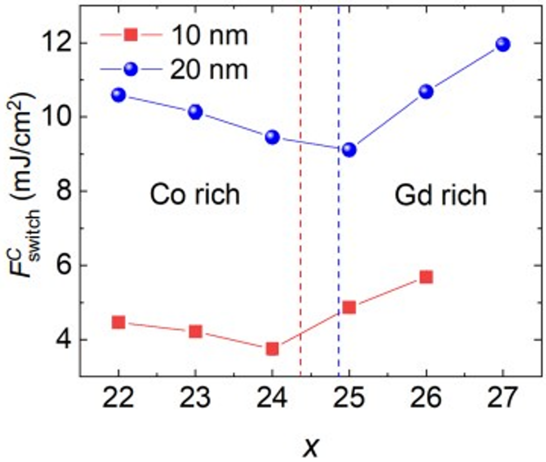

FIGURE 4.12 – F_{switch} of a series of 10- and 20-nm-thick GdFeCo layers with different Gd concentrations ranging from 22 to 27%.[13]

Most of the results described above can be understood by considering the switching as the action of the spin current generated by the demagnetization of Gd sublattice and the transferring of angular momentum to the rest of the system when reaching the ordering temperature of the sample. This hypothesis is based on the experimental results in Gd-based spin-valve[71;72] and the model developed by Remy *et al.*[199]. But why is Gd remains an open question as we discussed in Section 4.1.2. Overall, F_{switch} is then expected to decrease with increasing the Gd concentration and with decreasing the ordering temperature of the alloy.

Multi-domain fluence

The multi-domain fluence is strongly dependent to the Curie temperature T_C of the sample[22;61], because the formation of multi-domain is a thermally activated magnetization process in nanosecond timescale[183–185]. From previous studies[81;200;201], we can argue that starting from a perpendicular magnetized sample one will favor a multi-domains if one can reduce the exchange coupling in the sample and/or increase the demagnetization field in the layer. The ability for a laser pulse to reduce the exchange coupling inside a magnetic layer is given by the Curie temperature T_C and by the amount of energy absorbed by the magnetic layer. In other words, the exchange coupling will reduce faster if the Curie temperature is low and if the temperature increase is large. The temperature increase is given by the laser fluence but also by the percentage of the energy absorbed by the layer. For a given sample stack, a magnetic layer with a higher T_C will require more energy to reach a demagnetization state. That could be an explanation why F_{multi} is almost constant and independent to the pulse duration. The system T_C is related the concentration of the elements, among the elements involved in this work, Co has the highest T_C at 1394 K, Gd has the highest T_C at 292 K among the four REs, and T_C of Tb, Dy and Ho is 222 K, 87 K, 20 K respectively (as found in handbooks).

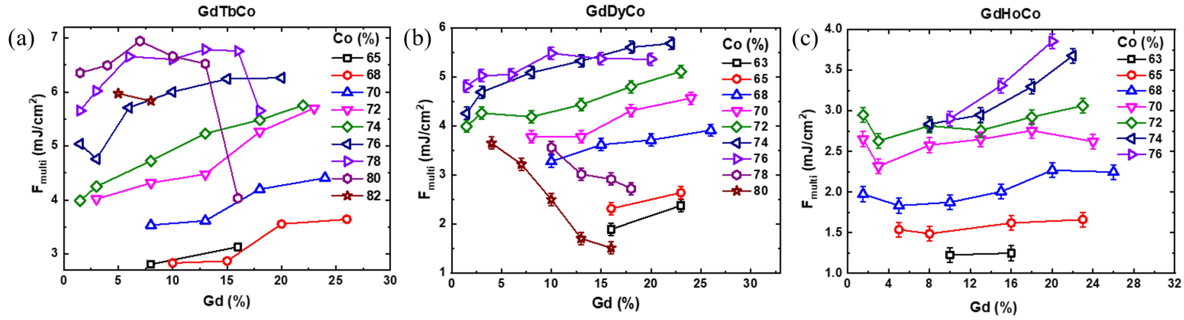

FIGURE 4.13 – F_{multi} as a function of Gd concentration in (a) GdTbCo, (b) GdDyCo and (c) GdHoCo with various Co concentration. Similar trend is shown of three material series, F_{multi} shows weak dependent Gd concentration but strong relationship to Co concentration. The lowest F_{multi} of 1.2 mJ/cm^2 is found in $Gd_{16}Ho_{21}Co_{63}$ which has the lowest Curie temperature among all the samples that we have grown.

Therefore, as shown in figure 4.13, F_{multi} is largely enhanced by increasing the Co concentration x from 64% to 78%, because the T_C of Co shows significant difference to that of REs. Even though Gd has a higher T_C than other REs, the effect of the variation of Gd and Tb (Dy, Ho) contents is marginal to the system T_C and no obvious rule can be found between F_{multi} and Gd concentration. Unfortunately, we are unable to characterize the Curie temperature of our samples because the highest temperature we can reach in our SQUID (superconducting quantum interference device) equipment is around 800 K, which is lower than the Curie temperature of these samples.

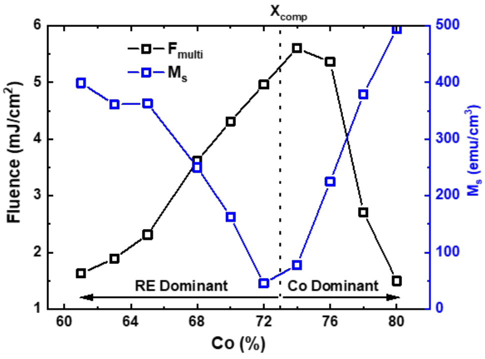

FIGURE 4.14 – F_{multi} and M_S as a function of Co concentration in $Gd_{18}DyCo$, with various Co concentration. A strong dependence of F_{multi} on M_S can be found, where samples closing to the compensation point with smaller M_S obtain higher threshold to a multi-domain state.

One has to remember that the domain formation is also due to the demagnetization field i.e. dipolar field generated by the net magnetization of the sample[81]. This field increases with the magnetization of the sample and with its thickness. This means that moving away from compensation will increase magnetization and favor a multi-domain state. This is the trend that can be observed in figure 4.14. Maximum F_{multi} is obtained around the compensation. However, it is difficult to say when and so at which temperature the demagnetization field and consequently the magnetization has to be considered. The formation of domains are certainly taking place at time much larger than the typical 10 ps, 100 ps switching time observed in AO-HIS, but still the temperature is certainly significantly larger than the initial room temperature. As a consequence, we observed that F_{multi} decrease faster with Co concentration in the Co rich region. We believe that it is caused by the fact that the heating of the laser not only reduce the exchange coupling but increase the magnetization for the Co rich samples, whereas it decreases for the Gd rich samples.

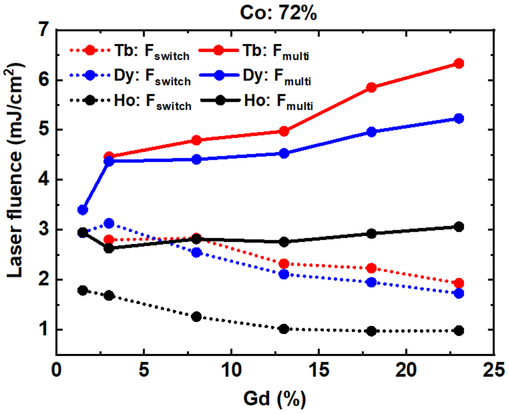

FIGURE 4.15 – F_{switch} and F_{multi} with the Gd concentration for samples of various doping elements, the composition of Co is 72%.

Figure 4.15 shows the function of F_{switch} and F_{multi} with the Gd concentration for samples of various doping elements, the composition of Co is 72%. The two fluences in Tb doped materials are the highest while that in Ho doped GdCo alloys are the lowest, it proves that both F_{switch} and F_{multi} are also T_C dependent to a certain extent. But that effect is less significant for F_{switch}, hence the largest switching window is found in the sample series of GdTbCo in which the F_{multi} is maximized.

Maximum pulse duration

The mapping of τ_{max} is explicitly shown in figure 4.10 (c). Obviously, one can see that a larger τ_{max} appears as the concentration of Gd y is increased when x keeps as constant. Within all the samples showing PMA, it highlights that the largest value of $\tau_{max} = 5.8$ ps is observed for $Gd_{26}Dy_6Co_{68}$ with the highest amount of Gd. This value is slightly larger than that observed in a pure $Gd_{23.3}Co_{76.7}$ alloy with $\tau_{max} = 5$ ps, due to the tiny bit more Gd concentration. When the composition of Co x is less than 68%, there is more space for increasing the concentrations of RE elements. However, the in-plane magnetic anisotropy occurs if the Gd composition y is higher than 23% with x = 63%. On the other hand, its relation with the Co concentration x is relatively weaker when the amount of Gd is the same.

The typical revolution of τ_{max} of three sample series is shown in figure 4.16. By fixing the Gd concentration, one can see that τ_{max} goes up firstly to a peak value, and then it decreases with more Co contents. Interestingly, the peak value occurs at around RE-TM compensation point x_{comp}. This agrees with previous report in pure GdFeCo alloys[13], that the maximum pulse duration is longer around x_{comp}. However, this phenomenon becomes less pronounced once the Gd concentration is higher than a certain value (it is roughly about 23%), wherein the value of τ_{max} is dominant by the contents of Gd. Hence, by introducing other RE elements into GdCo alloys with the PMA maintained, is a practical way to extend the laser pulse durations used to observe AO-HIS. And, we propose that putting more Gd elements and getting closer to the x_{comp} is helpful to achieve a high value of τ_{max}.

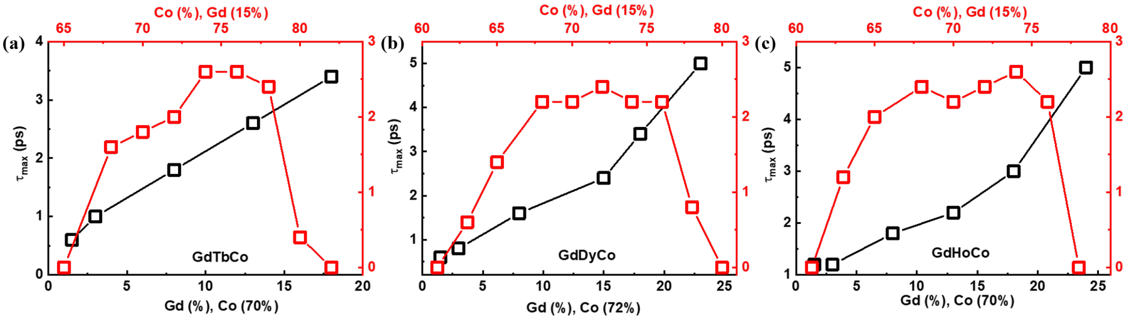

FIGURE 4.16 – The typical revolution of τ_{max} with Gd and Co concentration in (a) GdTbCo, (b) GdDyCo and (c) GdHoCo, τ_{max} can be extended by doping more Gd into samples, the largest τ_{max} in our samples is about 5 ps.

Enlarging τ_{max} is important in the engineering application of AO-HIS actually. The pulse duration of a traditional electric pulse is limited in nanosecond timescale, if τ_{max} can be enlarged to nanosecond, the integration of circuits and storage medium of AO-HIS material will be a promising spintronic device. Yang *et al.* realized ultrafast magnetization reversal by picosecond electrical pulses in GdFeCo films[29], subsequently, Jhuria *et al.* employed similar idea to switch a ferromagnet by spin-orbit torque with picosecond electrical pulses[202], but in both two works, the electrical pulse is generated through a photoconductive switch which still need the present of laser pulses. Now that the origin of AO-HIS in GdFeCo has been widely accepted to be a pure thermal effect, it can be realized by the excitation of both optical pulses[8], electrical pulses[29], and hot-electron pulses[28]. If the pulse duration can be extended to nanosecond timescale and thus be integrated with traditional semiconductor device, it will be a competitive solution for MRAM application.

Slope

The last parameter k describing the dependence of F_{switch} on pulse duration is the consequence of the evolution of the other three ones. It can be increased by weather increasing F_{switch}, τ_{max} or decreasing F_{multi}, when the other two parameters keep constant. According to figure 4.10 (d), the region showing a maximum k with the dark red color is mainly located in the samples with Co concentrations less than x = 68%. In this case, the very low F_{multi} as shown in figure 4.10 (b) is the major contribution to the large value of k. As shown in figure 4.17 , by fixing the composition of Gd or Dy in GdDyCo, k decreases monotonically with increasing Co concentration, as the largest T_C and F_{multi} is found in the sample with the most Co. Interestingly, the maximum of k after doping Dy is almost the same with that in the pure GdCo alloy, however, it can be ascribed to the quite large value of τ_{max}. From the above results one can see that k is a passive parameter that is jointly constrained by F_{multi} and τ_{max}. Unfortunately, we are not able to give a physical reference of k and why is k is constant with the pulse duration based on the results that we have.

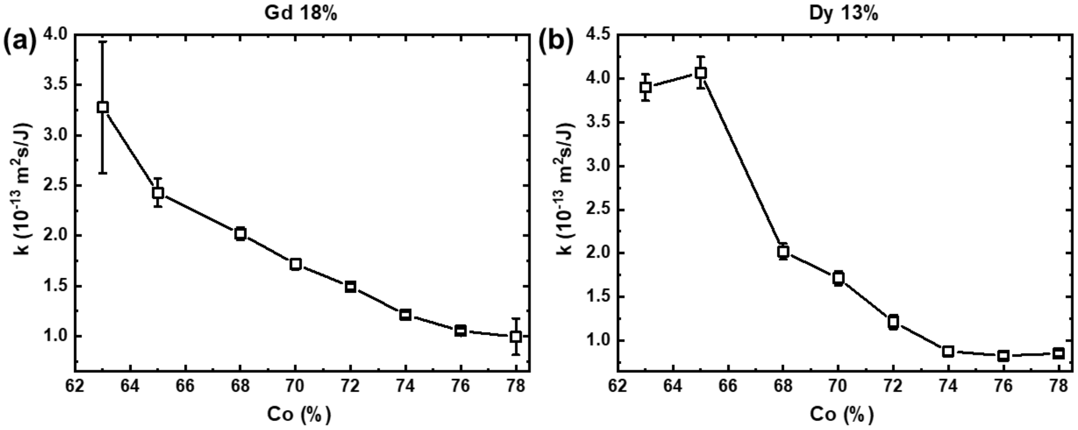

FIGURE 4.17 – The slope k as a function of Co concentration in (a) $Gd_{18}DyCo$ alloys and (b) $GdDy_{13}Co$.

By concluding the dependence of the four key parameters and the elements concentration, we saw some specific rules, also some vague behavior. Overall, the results give some clues on the role of Gd in AO-HIS and pave the way on materials engineering to enlarge the switching fluence window and the maximum pulse duration.

4.3 Spin dynamics of switching

In the static state diagram of AO-HIS, the evolution of four important parameters including F_{switch}, F_{multi}, τ_{max} and k as a function of Gd, R and Co concentrations were systemically investigated. Besides, the timescale at which the magnetization is reversed is another critical concern, since the optical magnetization switching owns unprecedented speeds and high energy efficience. In previous reports, the influence of Tb content on the temporal dynamics of GdTbCo alloys was investigated, in which the different intrinsic damping for Tb and Gd accounts for the vanish of switching when Tb content is too high[23;24]. However, the reports on the various explicit time-resolved dynamics of the switching process in GdRCo alloys for different Co concentrations are still lacking. This raises the question whether the switching speed in RE-TM alloys can be tailored when the samples are crossing the compensation point.

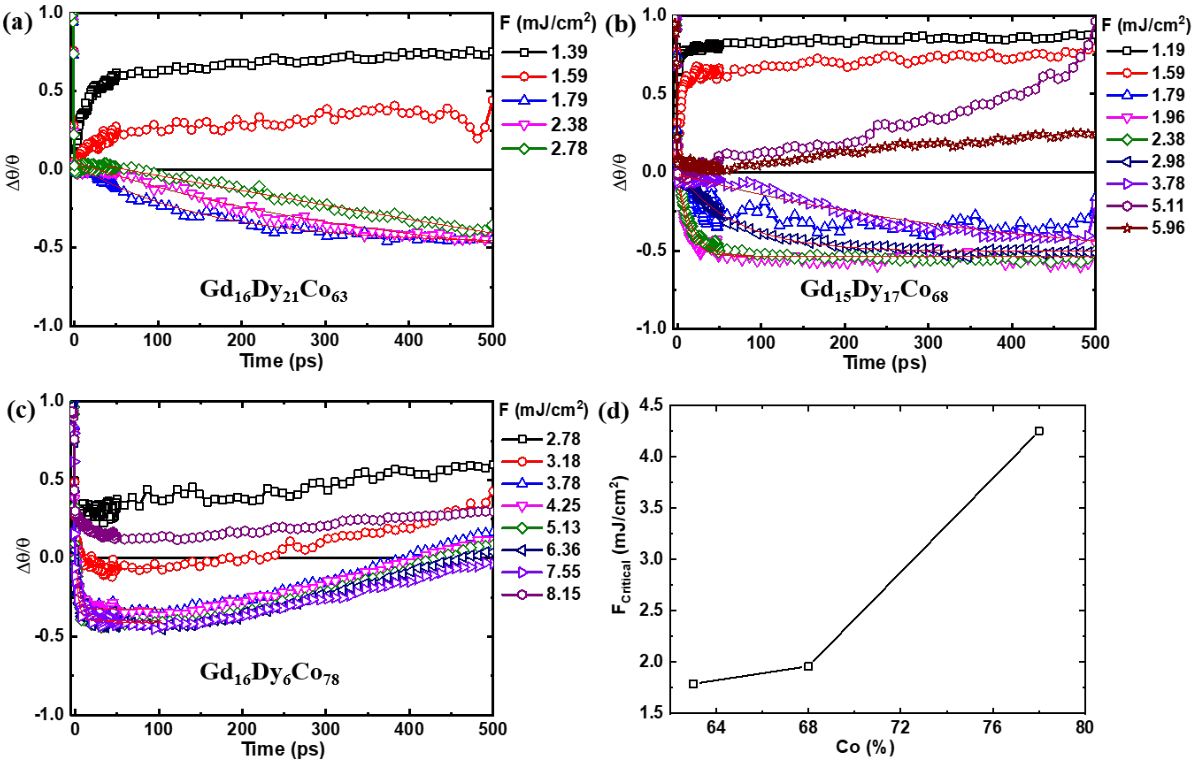

FIGURE 4.18 – TR-MOKE results on laser-fluence-dependent magnetization dynamics for (a) $Gd_{16}Dy_{21}Co_{63}$, (b) $Gd_{15}Dy_{17}Co_{68}$ and (c) $Gd_{16}Dy_{6}Co_{78}$ alloys. (d) $F_{critical}$ of the above three samples, sample with larger Co concentration has larger $F_{critical}$.

Thus, the temporal dynamics for GdRCo alloys with various Co compositions x was measured by TR-MOKE. Figure 4.18 (a-c) shows the laser fluence dependent magnetization dynamics for $Gd_{16}Dy_{21}Co_{63}$, $Gd_{15}Dy_{7}Co_{68}$ and $Gd_{16}Dy_{6}Co_{78}$ samples using TR-MOKE. One can see that, it has one critical fluence $F_{critical}$ allowing for the fastest magnetization switching with the maximum switching amptitude. $F_{critical}$ increases gradually by increasing the content of Co as is shown in figure 4.18 (d). Indeed, we obtained similar rule on F_{switch} with the Co content in last section, proving that $F_{critical}$ is associated with F_{switch}.

We repeat above laser-fluence-dependent measurements for samples of $Gd_yDy_{1-x-y}Co_x$ alloys by varying the Co compositions from 63% to 78% with y around 16%. And then, the magnetization switching dynamics at $F_{critical}$ is extracted and shown in figure 4.19 (a). By changing the concentration of Co, a pronounced difference is observed for the dynamic process after the ultrfast decrease of magnetization. For instance, a long-lived mangeitzation state with $\Delta\theta/\theta \approx 0$ is presented for x = 63% untill t = 20 ps, after that a slow remagnetization in the opposite direction occurs. And the maximum amptitude of switching is reached at about t = 400 ps. With increasing x, the remagnetization is systemsical faster. Interestingly, it becomes fast dramaticaly when the Co composition is approaching x = 72%, which is very close to the compensation point. By increasing Co composition further, the remagnetization dynamics in less than 20 ps is quite similar for the samples with x > 72%. The similar trend is also found for GdTbCo and GdHoCo alloys, whose Co concentration dependent magnetization dynamics is shown in figure 4.19 (b-c).

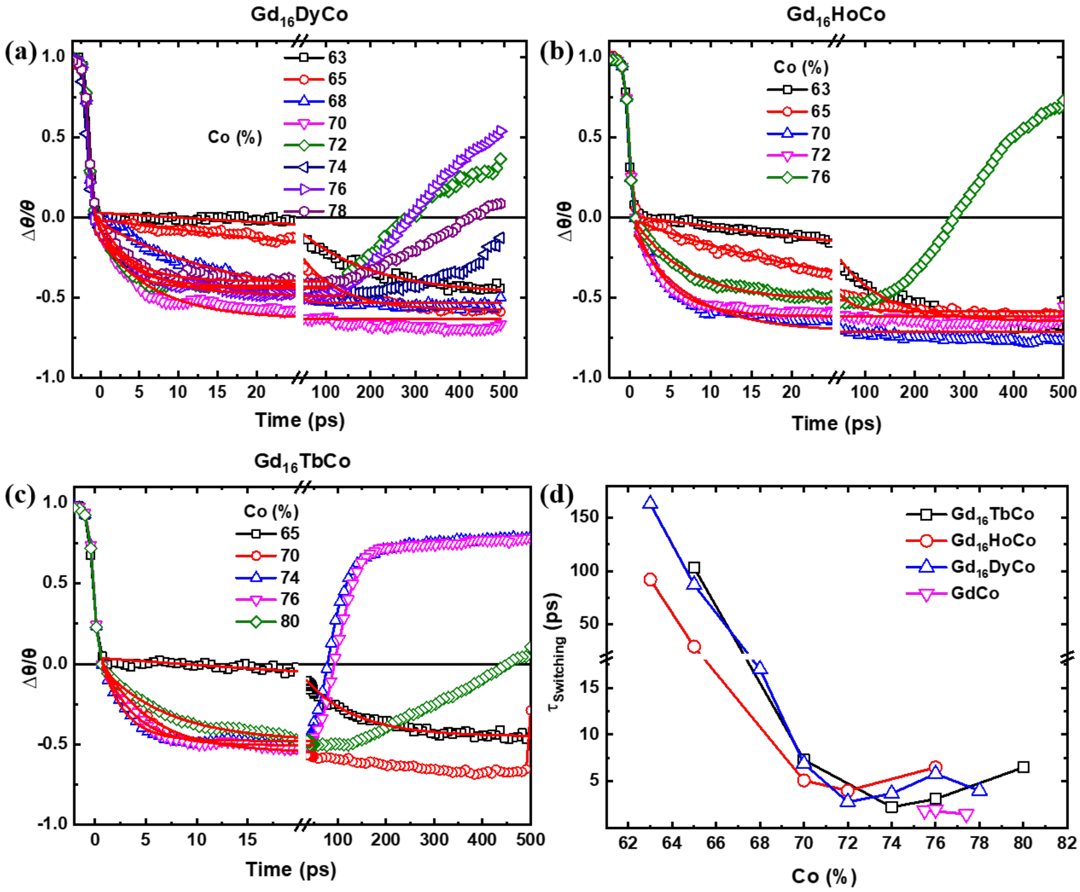

FIGURE 4.19 – TR-MOKE results of samples with various Co concentration when the Gd composition is fixed at 16%, $\Delta\theta/\theta$ as a function of time for (a) $Gd_{16}DyCo$, (b) $Gd_{16}HoCo$ and (c) $Gd_{16}TbCo$ series. (d) $\tau_{switching}$ as a function of Co concentration for GdCo alloys doped by different elements. $\tau_{switching}$ decreases with the Co concentration and reaches a constant value when Co concentration is larger than 70%.

In order to quantitativly understand the speed of magnetization switching, an exponential equation is used to fit the remagnetization process.

$$\Delta\theta/\theta = 2exp\left(-t/\tau_{switching}\right) - 1 \tag{4.2}$$

The fitting parameter $\tau_{switching}$ is used to describe the switching time in alloys. Figure 4.19 (d) clearly shows the extracted $\tau_{switching}$ as a function of Co compositions in $Gd_{16}RCo$. For GdDyCo alloys, one can see a rapid drop of $\tau_{switching}$ with the Co composition increasing to be around the compensation point, while it changes slightly when x is larger than 72%. By replacing Dy with Tb or Ho, same revolution is presented.

The above slow down dynamics of remagnetization taking place at the samples with less Co contents might come from two kinds of contributions. Firstly, the lower Curie temperature with less amount of Co. Based on the micromagnetics simulations[203], the longitudinal relaxation time of magnetization increases rapidly as the temperature is close to Curie temperature. Actually, the slow down effect is quite general if the Curie temperatur of the materials is so low that it close to the ambient temperature[204]. Moreover, the ratio T_c/μ_{at}[54] has been proposed explicitly to be a decisive role in the ultrafast demagnetiation time of magnetic materials, suggesting a lower T_c leads to a slower demagnetization. Secondly, the reduced Gilbert damping when the sample is away from the compensation point. The maximum value of Gilbert damping of RE-TM alloys has been demonstrated to be near the compensation point[189]. According to the theory of Koopmans *et al.*[205], the relaxation time of magnetization is inversely propositional to the value of Gilbert damping. So, when the Co concentration is less, the relaxation time of amgnetization might be longer as the Gilbert damping of RE-TM alloys is decreased.

4.4 Conclusion

In this chapter, we have deposited a series of Gd$_y$R$_{1-x-y}$Co$_x$ alloys, We demonstrated that in all those alloys Gd is required to observe AO-HIS but only a very small amount as low as 1.5% is enough. Besides, doping others REs with higher spin-orbit coupling into GdCo can enlarge the composition range that shows AO-HIS. Then, the single-shot AO-HIS state diagrams for various Gd$_y$R$_{1-x-y}$Co$_x$ alloys are systemically presented, from which we clarified the dependence of laser parameters allowing for switching on the concentrations of Gd, R and Co element, respectively. These state diagrams clearly illustrate : 1), the compositions window allowing for AO-HIS is significantly broaden as compared with a pure GdFeCo alloy ; 2), the maximum pulse duration τ_{max} allowing for AOS is around 6 ps ; 3), the evolution of F_{switch}, F_{multi}, τ_{max} and the slope k as a function of elements concentrations, respectively. Subsequently, the dynamics of magnetization switching as a function of Co compositions are investigated by means of TR-MOKE measurements. Once the Co composition x is approaching the compensation point, we identified that the amount of Gd content is much less needed to observe the AO-HIS, meanwhile, the magnetization switching speed becomes faster. The results in this work provide a practical way to enlarge the switching region of AO-HIS, including both the materials compositions and laser parameters, which will be of great significance for the spintronic applications.

Chapitre 5

Conclusion

In conclusion, this thesis presents two studies which respectively focuses on the mechanism of AO-HDS and AO-HIS.

we demonstrated AO-HDS in a Co/Pt magnetic square within 10 consecutive circularly polarized pulses and studied the spin dynamics during and after each pulse. In this process, the switching is realized by two stages : (1) magnetization from -1 to 0, in this stage, each pulse first brings a thermal induced nucleation, then followed by a domain shrink result from the domain pressure, but the nucleation is dominant and carries out the stage 1 ; (2) magnetization from 0 to +1, in this stage, also, each pulse first induces a thermal nucleation, but this value is much smaller than stage 1 because of MCD, then, the MCD generate a thermal difference between two magnetizations, and this difference drives DW from clod region to hot region and accomplish the switching. It is worth noting that in these two stages, there are lots of other interaction and motivation, for instance the IFE during each exposure and the domain shrink in stage 2. Here we think the thermal induced nucleation and MCD induced DW motion play the key roles to accomplish the AO-HDS.

Since the nucleation in stage 1 is not helicity-dependent, the DW motion in stage 2 is the root of this kind of helicity-dependent phenomenon. So to obtain AO-HDS in magnetic material, it is essential that, MCD can show a great impact and create a great temperature gap between two magnetization, and a quick DW motion can be obtained (or the pinning effect can be overcome) under this temperature gap.

For AO-HIS in GdRCo, the single-shot AO-HIS state diagrams for various $\mathrm{Gd}_y\mathrm{R}_{1-x-y}\mathrm{Co}_x$ (R = Dy, Tb, Ho) alloys are systemically presented, from which we clarified the dependence of laser parameters allowing for switching on the concentrations of Gd, R and Co respectively. Once the Co composition is approaching the compensation point, we identified that the amount of Gd content is much less needed to observe the AO-HIS, meanwhile, the magnetization switching speed becomes faster by measuring the ultrafast spin dynamics of samples. The state diagrams of samples with various elements concentration clearly describe the behavior of AO-HIS and helps understanding its physics and possible origin. Even though we are not able to establish a complete theory to explain the mechanism of AO-HIS so far, our results pave the way to find the best RE-TM exhibiting AO-HIS, which will be of great significance for the spintronic applications.

Résumé étendu

La puce mémoire est un circuit intégré pouvant stocker des données. Dans les systèmes de mémoire basé sur le transistor à semi-conducteurs, il existe un compromis entre sa vitesse de fonctionnement et sa densité, comme indiqué dans la figure 5.1. Au cours de ces 30 dernières années, grace à la découverte de l'effet de Magnétorésistance Géante, des mémoires à base de matériaux magnétiques on pu être réalisé avec succès pour le stockage de l'information. Pour ces systèmes de mémoire basé sur l'électronique de spin (ou spintronique) la densité et la vitesse peuvent être amélioré en même temps.

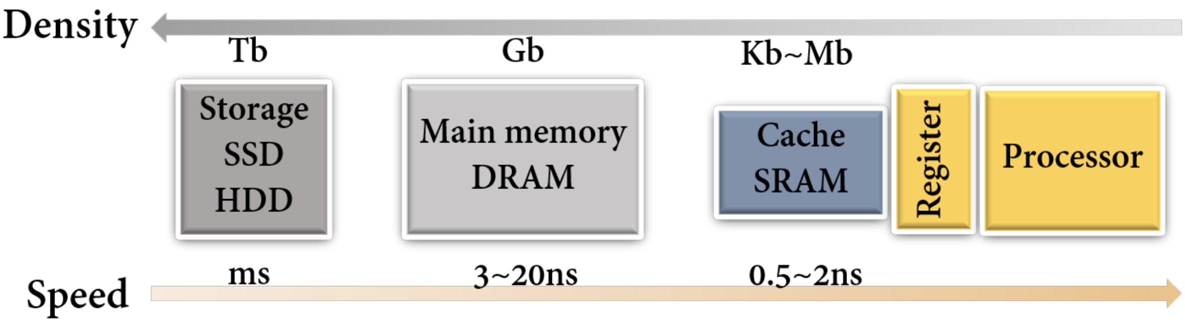

FIGURE 5.1 – Compromis entre la densité et la vitesse de fonctionnement dans les puces mémoire, différents dispositifs ont été appliqués à différentes puces mémoire pour répondre à des exigences spécifiques.

Avec la découverte de l'effet de magnétorésistance géant[2;3], les dispositifs magnétiques, utilisant la spintronique, ont été appliqués avec succès pour le disque dur (HDD pour hard disk drive en anglais) est la mémoire magnétique. Un disque dur traditionnel utilise une tête magnétique pour écrire les informations, qui a une faible vitesse et apporte de l'instabilité au système. Dans ce cas, la spintronique a permis de réaliser des tête de lecture très rapide et avec une sensibilité amélioré.

Ces dernières années, avec la découverte du couple de transfert de spin (STT pour spin transfer torque en anglais)[4;5] et du couple spin-orbite (SOT pour spin orbit torque en anglais)[6;7], il est maintenant possible de manipuler l'aimantation avec du courant électrique. La réalisation d'un dispositif de mémoire magnétique STT ou SOT, avec une vitesse de fonctionnement plus élevée, serait très prometteuse pour les mémoires magnétiques pour les mémoires vives qui nécessite une vitesse de fonctionnement plus élevée. L'idée de base du STT ou SOT est d'utiliser le courant électrique pour générer un courant de spin polarisé afin de commuter l'aimantation. il y a deux problèmes qui limitent la vitesse. Le première est due à la dynamique de l'aimantation, le renversement est obtenu après précession de l'aimantation ce processus prend de quelques centaines picosecondes à quelques nanosecondes. D'autre part, les semi-conducteurs à base de silicium ne permetent pas la génération d'impulsions de courant ultracourtes.

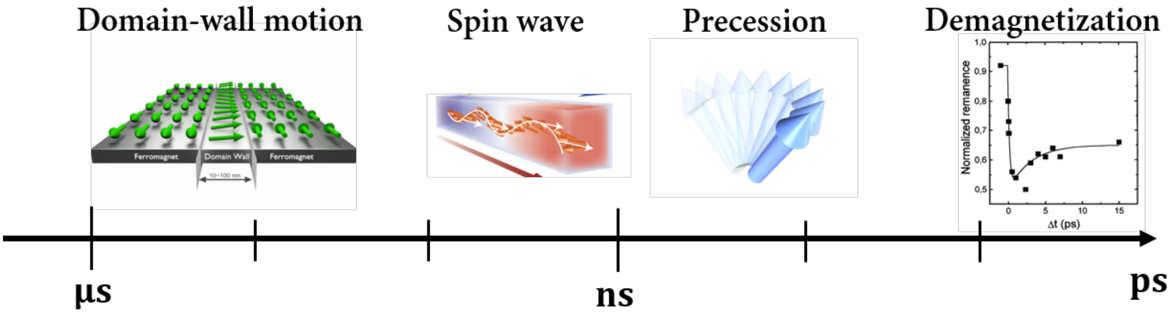

FIGURE 5.2 – La dynamique de spin se produit à différentes échelles de temps et la démagnétisation ultra-rapide est démontrée au niveau de la picoseconde.

L'utilisation de la lumière pour renverser l'aimantation pourrait résoudre ces deux problèmes en même temps. Une impulsion laser ultracourte à l'échelle de temps femtoseconde peut être générée[197;198]. Et il a été observé qu'un film magnétique subit une désaimantation ultrarapide sous l'effet d'une impulsion laser[42], il s'agit d'une diminution de l'amplitude de l'aimantation qui se produit dans un laps de temps beaucoup plus court que la précession comme le montre la figure 5.2. Par conséquent, l'utilisation d'impulsions optiques ultracourtes pour manipuler l'aimantation serait possible pour accélérer l'opération de mémoire magnétique.

En 2007, Stanciu et al. ont démontré la première inversion d'aimantation avec des impulsions laser femtosecondes[8], ils ont utilisé un train d'impulsions polarisé circulairement pour commuter l'aimantation de l'alliage GdFeCo et ont observé que l'état final de l'aimantation peut être manipulé en changeant l'hélicité de la lumière. Parce qu'aucun champ magnétique externe n'est introduit dans le phénomène, une telle inversion de magnétisation est appelée commutation tout optique (AOS pour all-optical switching en anglais). En outre, la direction de l'aimantation n'est déterminée que par l'hélicité de la lumière, d'où ce type de comportement appelé commutation dépendante de l'hélicité optique (AO-HDS pour all-optical helicity-dependent switching en anglais). En 2011, Radu et al. ont observé un autre phénomène fantastique d'AOS dans l'alliage GdFeCo[9]. Ils ont montré que l'alliage ferrimagnétique GdFeCo avec anisotropie magnétique hors plan peut en fait être commuté par une seule impulsion femtoseconde. Chaque excitation d'impulsion déclenche une inversion de, et un tel comportement n'est pas lié à l'hélicité du laser, d'où son nom de commutation indépendante de l'hélicité optique (AO-HIS pour all-optical helicity-independent switching en anglais). La découverte d'AO-HIS a suscité un grand intérêt parmi les chercheurs, car l'utilisation d'impulsions lumineuses ultracourtes pour commuter l'aimantation en quelques picosecondes ou femtosecondes est une méthode prometteuse pour l'écriture ultrarapide de données de mémoires magnétiques et améliore considérablement la vitesse de traitement des données.

Par conséquent, il existe en fait deux types d'AOS : AO-HIS où la commutation peut être accomplie avec un seul coup d'impulsion laser et l'état final de l'aimantation est déterminé par l'état magnétique initial plutôt que par l'hélicité lumineuse, et AO-HDS où il doit être accompli par plusieurs impulsions et l'aimantation finale est déterminée par l'hélicité lumineuse. Au fil des années, de nombreuses questions sont soulevées sur le mécanisme de l'AOS, pour AO-HDS, son origine peut être simplement interprétée comme l'absorption différente du moment angulaire du laser polarisé circulairement, tandis que pour AO-HIS, l'impulsion laser polarisée linéairement n'apporte pas de moment angulaire mais seulement de la chaleur. En conséquence, l'enthousiasme des chercheurs a été grandement stimulé depuis lors, et un grand nombre d'études ont été rapportées sur ces deux phénomènes différents en se concentrant sur les systèmes matériels, les mécanismes et leurs applications.

Dans cette thèse, nous nous concentrerons sur la physique de l'AO-HDS et de l'AO-HIS, en étudiant le comportement et la dynamique du processus induit par laser, nous tenterons de donner des mécanismes possibles derrière eux.

Ce manuscrit sera organisé en 4 chapitres. Dans le chapitre 1, un état de l'art dans le domaine des AOS sera brièvement présenté. Pour comprendre l'inversion magnétique par impulsion laser, la physique de la dynamique de spin induite par laser sera d'abord introduite, y compris quelques concepts de base du magnétisme, de la lumière et de leurs interactions. Ensuite, les comportements, les systèmes matériels et les mécanismes possibles de l'AO-HIS et de l'AO-HDS seront abordés dans les deux sections suivantes. Pour AO-HIS, à l'exception de plusieurs matériaux très uniques, il ne peut être observé que dans les systèmes ferrimagnétiques à base de Gd, il sera donc très intéressant d'essayer de comprendre la spécialité de l'élément Gd. Une théorie bien acceptée pour expliquer la commutation dans les ferriaimants à base de Gd (tels que GdCo) est basée sur le taux de démagnétisation lent du sous-réseau Gd, il a été observé que Gd montre beaucoup plus de temps pour être démagnétisé que Co lorsque l'alliage GdCo est excité par une impulsion laser femto-seconde. Un mécanisme basé sur les différents taux de démagnétisation de deux sous-réseaux sera introduit pour expliquer la physique de l'AO-HIS. Pour AO-HDS, son comportement et son système matériel sont très différents de ceux de l'AO-HIS, ainsi que son mécanisme. Trois effets (effet Faraday inverse, dichroïsme circulaire magnétique (MCD pour Magnetic circular dichroism en anglais) et magnétisation induite par l'absorption lumineuse) qui seraient à l'origine de l'AO-HDS seront introduits dans cette section.

Dans le chapitre 2, les méthodes expérimentales que nous avons utilisées dans cette thèse seront présentées. Le dépôt physique en phase vapeur est utilisé pour développer les films magnétiques qui seront étudiés. Dans ce manuscrit, un film multicouche

Co/Pt typique sera utilisé pour étudier le mécanisme de l'AO-HDS, et pour AO-HIS, une série complète d'alliages $\mathrm{Gd}_y\mathrm{R}_{1-x-y}\mathrm{Co}_x$ (R = Tb, Dy et Ho) de 10 nm d'épaisseur sont préparés. Les sections suivantes sont consacrées aux méthodes de caractérisation des échantillons utilisés, y compris les configurations magnéto-optiques basées sur l'effet Kerr magnéto-optique (MOKE pour magneto-optic Kerr effect en anglais), telles que la microscopie MOKE, la mesure MOKE à résolution temporelle et le spectromètre MCD. En outre, la fabrication des dispositifs nécessaires à la détection électrique de l'AO-HDS est décrite. Enfin, nous combinons le système laser femtoseconde, la microscopie MOKE et les mesures de transport électrique à un système AOS qui peut générer et étudier la commutation optiquement et électriquement simultanément.

Dans le chapitre 3, le comportement et la physique sous-jacente de l'AO-HDS dans les multicouches ferromagnétiques Co/Pt sont discutés. On étudie comment certains facteurs critiques, tels que la durée des impulsions, le taux de répétition des impulsions, le nombre d'impulsions et leur fluence, affectent l'efficacité de la commutation. Le mouvement de la paroi du domaine est présenté comme l'ingrédient clé de l'ensemble du processus de commutation, les détails de la dynamique de la paroi du domaine dans les films métalliques minces sont discutés. Après avoir examiné le comportement de commutation de nos échantillons, un modèle pour expliquer AO-HDS est ensuite créé, présentant la commutation comme un processus en deux étapes, en commençant par la combinaison de mécanismes thermiques et non thermiques nucléant un certain nombre de petits domaines. Ceci est suivi, dans la deuxième étape, par la croissance de ces domaines nucléés entraînés par des gradients thermiques.

Pour soutenir ce modèle, nous étudions attentivement la réponse à effet Hall de notre dispositif magnétique Hall pendant et après chaque impulsion. Nous avons remarqué que sous l'excitation d'une impulsion polarisée circulairement, la résistance de Hall subit un saut rapide dans les premiers 20 μs qui est suivi d'une lente relaxation vers la direction opposée jusqu'à l'arrivée de l'impulsion suivante. Essayer de résoudre la physique derrière le saut et la relaxation est très utile pour comprendre le mécanisme de AO-HDS, par conséquent, nous essayons diverses fluence et polarisation laser pour voir comment l'amplitude du saut et de la relaxation change avec ces paramètres. Par la suite, nous avons remarqué que leur comportement montre une différence évidente dans les différentes étapes de l'inversion. Au stade 1, où l'aimantation nette est de -1 à 0, le saut est toujours positif tandis que la relaxation est toujours négative, et l'amplitude du saut augmente avec la fluence laser tandis que celle de relaxation semble être indépendante avec la fluence. Au stade 2, où l'aimantation nette est de 0 à +1, le saut est toujours négatif et la relaxation est toujours positive. Fait intéressant, l'ampleur de la relaxation augmente avec la fluence du laser au stade 2. Après avoir considéré la direction et la relation avec la fluence laser du saut et de la relaxation, nous sommes en mesure de conclure que le saut est le comportement de la nucléation du domaine et que la relaxation est le comportement de la formation du domaine, alors qu'une telle formation de domaine a une force motrice différente dans différentes étapes : la pression du domaine au stade 1 et le gradient thermique au stade 2.

Il est démontré que la réponse à effet Hall du dispositif magnétique pendant et après chaque impulsion avec diverses fluences et polarisations peut bien soutenir ce modèle. Sur la base de ces résultats, on pourrait certainement optimiser le processus pour réduire considérablement le nombre d'impulsions nécessaires à la commutation.

Dans le chapitre 4, nous étudions le mécanisme de l'AO-HIS dans un alliage ternaire GdRCo, nous modifions la concentration des éléments, l'objectif général était de comprendre le rôle des différents éléments de terres rares dans l'efficacité de la commutation. L'inversion de l'aimantation par impulsion laser femtoseconde est observée dans la plupart des échantillons, même lorsque la concentration de Gd est aussi faible que 1,5%. Nous avons également pu démontrer AO-HIS pour une gamme beaucoup plus large de concentrations de Co et de terres rares que les alliages de GdCo ou de GdFeCo purs.

Le diagramme d'état triangulaire pour AO-HIS peut être défini par deux lignes $\boldsymbol{F_{switch}}$: la fluence du seuil d'impulsion laser pour la commutation d'impulsion unique en fonction de la durée de l'impulsion, et $\boldsymbol{F_{multi}}$: la fluence du seuil d'impulsion laser à laquelle le matériau se divise en multi-domaines en fonction de la durée de l'impulsion. Nous avons pu clairement démontrer que ces deux fluences varient différemment avec les paramètres magnétiques des matériaux tels que l'aimantation saturée, le couplage d'échange et la quantité de Gd. Par conséquent, nous pouvons définir les critères qui doivent être remplis pour observer AO-HIS. Nous avons pu démontrer pourquoi, dans de nombreux cas, il est essentiel d'être proche de la compensation pour observer la commutation de l'aimantation sous un seul laser femto-seconde. En étudiant la révolution de certains paramètres clés qui déterminent les propriétés de commutation parmi les échantillons, certaines règles peuvent être révélées pour mieux comprendre le mécanisme de l'AO-HIS, ainsi que pour identifier les paramètres idéaux du matériau et du faisceau pour les dispositifs AOS du point de vue de l'efficacité énergétique et de la stabilité du système.

En conclusion, nous étudions respectivement la physique de l'AO-HDS et de l'AO-HIS, nous sommes en mesure de donner un mécanisme général pour expliquer l'AO-HDS et donner les critères de présence de l'AO-HIS. Ce manuscrit offre non seulement notre compréhension à AOS, mais ouvre également la voie à l'optimisation des matériaux et à l'application d'ingénierie pour un dispositif AOS.

Bibliographie

[1] I.B.M. To Put Out New 'Think' Units. *New York Times* (1956). URL `https://www.nytimes.com/1956/09/14/archives/i-b-m-to-put-out-new-think-units-4-more-electronic-devices-produced.html`.

[2] Baibich, M. N. *et al.* Giant Magnetoresistance of (001)Fe/(001)Cr Magnetic Superlattices. *Physical Review Letters* **61**, 2472–2475 (1988). URL `https://link.aps.org/doi/10.1103/PhysRevLett.61.2472`.

[3] Binasch, G., Grünberg, P., Saurenbach, F. & Zinn, W. Enhanced magnetoresistance in layered magnetic structures with antiferromagnetic interlayer exchange. *Physical Review B* **39**, 4828–4830 (1989). URL `https://link.aps.org/doi/10.1103/PhysRevB.39.4828`.

[4] Katine, J. A., Albert, F. J., Buhrman, R. A., Myers, E. B. & Ralph, D. C. Current-Driven Magnetization Reversal and Spin-Wave Excitations in Co / Cu / Co Pillars. *Physical Review Letters* **84**, 3149–3152 (2000). URL `https://link.aps.org/doi/10.1103/PhysRevLett.84.3149`.

[5] Diao, Z. *et al.* Spin-transfer torque switching in magnetic tunnel junctions and spin-transfer torque random access memory. *Journal of Physics : Condensed Matter* **19**, 165209 (2007). URL `https://iopscience.iop.org/article/10.1088/0953-8984/19/16/165209`.

[6] Liu, L., Lee, O. J., Gudmundsen, T. J., Ralph, D. C. & Buhrman, R. A. Current-Induced Switching of Perpendicularly Magnetized Magnetic Layers Using Spin Torque from the Spin Hall Effect. *Physical Review Letters* **109**, 096602 (2012). URL `https://link.aps.org/doi/10.1103/PhysRevLett.109.096602`.

[7] Liu, L. *et al.* Spin-Torque Switching with the Giant Spin Hall Effect of Tantalum. *Science* **336**, 555–558 (2012). URL `https://www.science.org/doi/10.1126/science.1218197`.

[8] Stanciu, C. D. *et al.* All-Optical Magnetic Recording with Circularly Polarized Light. *Physical Review Letters* **99**, 047601 (2007). URL `https://link.aps.org/doi/10.1103/PhysRevLett.99.047601`.

[9] Radu, I. *et al.* Transient ferromagnetic-like state mediating ultrafast reversal of antiferromagnetically coupled spins. *Nature* **472**, 205–208 (2011). URL http://www.nature.com/articles/nature09901.

[10] Ostler, T. *et al.* Ultrafast heating as a sufficient stimulus for magnetization reversal in a ferrimagnet. *Nature Communications* **3**, 666 (2012). URL http://www.nature.com/articles/ncomms1666.

[11] El Hadri, M. S. *et al.* Two types of all-optical magnetization switching mechanisms using femtosecond laser pulses. *Physical Review B* **94**, 064412 (2016). URL https://link.aps.org/doi/10.1103/PhysRevB.94.064412.

[12] Gorchon, J. *et al.* Role of electron and phonon temperatures in the helicity-independent all-optical switching of GdFeCo. *Physical Review B* **94**, 184406 (2016). URL https://link.aps.org/doi/10.1103/PhysRevB.94.184406.

[13] Wei, J. *et al.* All-optical Helicity-Independent Switching State Diagram in Gd - Fe - Co Alloys. *Physical Review Applied* **15**, 054065 (2021). URL https://link.aps.org/doi/10.1103/PhysRevApplied.15.054065.

[14] Banerjee, C. *et al.* Single pulse all-optical toggle switching of magnetization without gadolinium in the ferrimagnet Mn2RuxGa. *Nature Communications* **11**, 4444 (2020). URL https://www.nature.com/articles/s41467-020-18340-9.

[15] Avilés-Félix, L. *et al.* Single-shot all-optical switching of magnetization in Tb/Co multilayer-based electrodes. *Scientific Reports* **10**, 5211 (2020). URL http://www.nature.com/articles/s41598-020-62104-w.

[16] Davies, C. *et al.* Exchange-driven all-optical magnetic switching in compensated 3 d ferrimagnets. *Physical Review Research* **2**, 032044 (2020).

[17] Mekonnen, A. *et al.* Role of the inter-sublattice exchange coupling in short-laser-pulse-induced demagnetization dynamics of GdCo and GdCoFe alloys. *Physical Review B* **87**, 180406 (2013). URL https://link.aps.org/doi/10.1103/PhysRevB.87.180406.

[18] El-Ghazaly, A. *et al.* Ultrafast magnetization switching in nanoscale magnetic dots. *Applied Physics Letters* **114**, 232407 (2019). URL http://aip.scitation.org/doi/10.1063/1.5098453.

[19] Beens, M., Lalieu, M. L. M., Deenen, A. J. M., Duine, R. A. & Koopmans, B. Comparing all-optical switching in synthetic-ferrimagnetic multilayers and alloys. *Physical Review B* **100**, 220409 (2019). URL http://arxiv.org/abs/1908.07292. ArXiv :1908.07292 [cond-mat].

[20] Lalieu, M. L. M., Peeters, M. J. G., Haenen, S. R. R., Lavrijsen, R. & Koopmans, B. Deterministic all-optical switching of synthetic ferrimagnets using single femtosecond laser pulses. *Physical Review B* **96**, 220411 (2017). URL `https://link.aps.org/doi/10.1103/PhysRevB.96.220411`.

[21] Li, P., Peeters, M. J. G., van Hees, Y. L. W., Lavrijsen, R. & Koopmans, B. Ultra-low energy threshold engineering for all-optical switching of magnetization in dielectric-coated Co/Gd based synthetic-ferrimagnet. *Applied Physics Letters* **119**, 252402 (2021). URL `http://arxiv.org/abs/2110.12063`. ArXiv :2110.12063 [cond-mat, physics :physics].

[22] Moreno, R., Ostler, T. A., Chantrell, R. W. & Chubykalo-Fesenko, O. Conditions for thermally induced all-optical switching in ferrimagnetic alloys : Modeling of TbCo. *Physical Review B* **96**, 014409 (2017). URL `http://link.aps.org/doi/10.1103/PhysRevB.96.014409`.

[23] Ceballos, A. *et al.* Role of Element-Specific Damping on the Ultrafast, Helicity-Independent All-Optical Switching Dynamics in Amorphous (Gd,Tb)Co Thin Films. *Physical Review B* **103**, 024438 (2021). URL `http://arxiv.org/abs/1911.09803`. ArXiv :1911.09803 [cond-mat].

[24] Zhang, W. *et al.* Role of spin-lattice coupling in ultrafast demagnetization and all optical helicity-independent single-shot switching in gd 1- x- y tb y co x alloys. *Physical Review B* **105**, 054410 (2022).

[25] Hu, Z. *et al.* Single-pulse all-optical partial switching in amorphous Dy $_{\mathrm{x}}$ Co $_{\mathrm{1x}}$ and Tb $_{\mathrm{x}}$ Co $_{\mathrm{1x}}$ with random anisotropy. *Applied Physics Letters* **120**, 112401 (2022). URL `https://aip.scitation.org/doi/10.1063/5.0077226`.

[26] Mangin, S. *et al.* Engineered materials for all-optical helicity-dependent magnetic switching. *Nature Materials* **13**, 286–292 (2014). URL `http://www.nature.com/articles/nmat3864`.

[27] Wilson, R. B. *et al.* Ultrafast magnetic switching of GdFeCo with electronic heat currents. *Physical Review B* **95**, 180409 (2017). URL `http://link.aps.org/doi/10.1103/PhysRevB.95.180409`.

[28] Xu, Y. *et al.* Ultrafast Magnetization Manipulation Using Single Femtosecond Light and Hot-Electron Pulses. *Advanced Materials* **29**, 1703474 (2017). URL `https://onlinelibrary.wiley.com/doi/10.1002/adma.201703474`.

[29] Yang, Y. *et al.* Ultrafast magnetization reversal by picosecond electrical pulses. *Science Advances* **3**, e1603117 (2017). URL `https://www.science.org/doi/10.1126/sciadv.1603117`.

[30] Alebrand, S. *et al.* Light-induced magnetization reversal of high-anisotropy TbCo alloy films. *Applied Physics Letters* **101**, 162408 (2012). URL http://aip.scitation.org/doi/10.1063/1.4759109.

[31] Hassdenteufel, A. *et al.* Thermally Assisted All-Optical Helicity Dependent Magnetic Switching in Amorphous Fe $_{100-x}$ Tb $_{x}$ Alloy Films. *Advanced Materials* **25**, 3122–3128 (2013). URL https://onlinelibrary.wiley.com/doi/10.1002/adma.201300176.

[32] Lambert, C.-H. *et al.* All-optical control of ferromagnetic thin films and nanostructures. *Science* **345**, 1337–1340 (2014). URL https://www.science.org/doi/10.1126/science.1253493.

[33] Stupakiewicz, A., Szerenos, K., Afanasiev, D., Kirilyuk, A. & Kimel, A. V. Ultrafast nonthermal photo-magnetic recording in a transparent medium. *Nature* **542**, 71–74 (2017). URL http://www.nature.com/articles/nature20807.

[34] Néel, L. Anisotropie magnétique superficielle et surstructures d'orientation. *Journal de Physique et le Radium* **15**, 225–239 (1954). URL http://www.edpsciences.org/10.1051/jphysrad:01954001504022500.

[35] Gilbert, T. L. A phenomenological theory of damping in ferromagnetic materials. *IEEE transactions on magnetics* **40**, 3443–3449 (2004).

[36] Neudecker, I. *et al.* Comparison of frequency, field, and time domain ferromagnetic resonance methods. *Journal of Magnetism and Magnetic Materials* **307**, 148–156 (2006).

[37] Elsayed-Ali, H. E., Norris, T. B., Pessot, M. A. & Mourou, G. A. Time-resolved observation of electron-phonon relaxation in copper. *Physical Review Letters* **58**, 1212–1215 (1987). URL https://link.aps.org/doi/10.1103/PhysRevLett.58.1212.

[38] Fann, W. S., Storz, R., Tom, H. W. K. & Bokor, J. Electron thermalization in gold. *Physical Review B* **46**, 13592–13595 (1992). URL https://link.aps.org/doi/10.1103/PhysRevB.46.13592.

[39] Agranat, M., Ashitkov, S., Granovskii, A. & Rukman, G. Interaction of picosecond laser pulses with the electron, spin, and phonon subsystems of nickel. *Zh. Eksp. Teor. Fiz* **86**, 10 (1984).

[40] Vaterlaus, A., Beutler, T. & Meier, F. Spin-lattice relaxation time of ferromagnetic gadolinium determined with time-resolved spin-polarized photoemission. *Physical*

Review Letters **67**, 3314–3317 (1991). URL https://link.aps.org/doi/10.1103/PhysRevLett.67.3314.

[41] Vaterlaus, A. *et al.* Different spin and lattice temperatures observed by spin-polarized photoemission with picosecond laser pulses. *Journal of Applied Physics* **67**, 5661–5663 (1990). URL http://aip.scitation.org/doi/10.1063/1.345918.

[42] Beaurepaire, E., Merle, J.-C., Daunois, A. & Bigot, J.-Y. Ultrafast Spin Dynamics in Ferromagnetic Nickel. *Physical Review Letters* **76**, 4250–4253 (1996). URL https://link.aps.org/doi/10.1103/PhysRevLett.76.4250.

[43] Hohlfeld, J., Matthias, E., Knorren, R. & Bennemann, K. H. Nonequilibrium Magnetization Dynamics of Nickel. *Physical Review Letters* **78**, 4861–4864 (1997). URL https://link.aps.org/doi/10.1103/PhysRevLett.78.4861.

[44] Güdde, J., Conrad, U., Jähnke, V., Hohlfeld, J. & Matthias, E. Magnetization dynamics of Ni and Co films on Cu(001) and of bulk nickel surfaces. *Physical Review B* **59**, R6608–R6611 (1999). URL https://link.aps.org/doi/10.1103/PhysRevB.59.R6608.

[45] Scholl, A., Baumgarten, L., Jacquemin, R. & Eberhardt, W. Ultrafast Spin Dynamics of Ferromagnetic Thin Films Observed by fs Spin-Resolved Two-Photon Photoemission. *Physical Review Letters* **79**, 5146–5149 (1997). URL https://link.aps.org/doi/10.1103/PhysRevLett.79.5146.

[46] Koopmans, B. *handbook of magnetism and advanced magnetic materials* (Wiley, 2007).

[47] Zhang, Q., Nurmikko, A. V., Miao, G. X., Xiao, G. & Gupta, A. Ultrafast spin-dynamics in half-metallic Cr O 2 thin films. *Physical Review B* **74**, 064414 (2006). URL https://link.aps.org/doi/10.1103/PhysRevB.74.064414.

[48] Müller, G. M. *et al.* Spin polarization in half-metals probed by femtosecond spin excitation. *Nature Materials* **8**, 56–61 (2009). URL https://www.nature.com/articles/nmat2341.

[49] Kise, T. *et al.* Ultrafast Spin Dynamics and Critical Behavior in Half-Metallic Ferromagnet : Sr 2 FeMoO 6. *Physical Review Letters* **85**, 1986–1989 (2000). URL https://link.aps.org/doi/10.1103/PhysRevLett.85.1986.

[50] Wang, J. *et al.* Ultrafast Quenching of Ferromagnetism in InMnAs Induced by Intense Laser Irradiation. *Physical Review Letters* **95**, 167401 (2005). URL https://link.aps.org/doi/10.1103/PhysRevLett.95.167401.

[51] Sun, C.-K., Vallée, F., Acioli, L. H., Ippen, E. P. & Fujimoto, J. G. Femtosecond-tunable measurement of electron thermalization in gold. *Physical Review B* **50**, 15337–15348 (1994). URL https://link.aps.org/doi/10.1103/PhysRevB.50.15337.

[52] Brown, W. Thermal Fluctuations of Fine Ferromagnetic Particles. *IEEE Transactions on Magnetics* **15**, 1196 – 1208 (1979).

[53] Malinowski, G. *et al.* Control of speed and efficiency of ultrafast demagnetization by direct transfer of spin angular momentum. *Nature physics* **4**, 855–858 (2008). Place : London Publisher : Nature Publishing Group.

[54] Koopmans, B., Kicken, H., van Kampen, M. & de Jonge, W. Microscopic model for femtosecond magnetization dynamics. *Journal of Magnetism and Magnetic Materials* **286**, 271–275 (2005). URL https://linkinghub.elsevier.com/retrieve/pii/S0304885304009497.

[55] Koopmans, B. *et al.* Explaining the paradoxical diversity of ultrafast laser-induced demagnetization. *Nature materials* **9**, 259–265 (2010). Place : England Publisher : Nature Publishing Group.

[56] Kuiper, K. C. *Exciting spins : revealing nonlocal effects in ultrafast magnetization dynamics*. PhD thesis, Technische Universiteit Eindhoven (2013). URL 10.6100/IR761385.

[57] Dalla Longa, F., Kohlhepp, J. T., de Jonge, W. J. M. & Koopmans, B. Influence of photon angular momentum on ultrafast demagnetization in nickel. *Physical Review B* **75**, 224431 (2007). URL https://link.aps.org/doi/10.1103/PhysRevB.75.224431.

[58] Mentink, J. H. *et al.* Ultrafast Spin Dynamics in Multisublattice Magnets. *Physical Review Letters* **108**, 057202 (2012). URL https://link.aps.org/doi/10.1103/PhysRevLett.108.057202.

[59] Davies, C. *et al.* Pathways for Single-Shot All-Optical Switching of Magnetization in Ferrimagnets. *Physical review applied* **13** (2020).

[60] Jakobs, F. & Atxitia, U. Universal Criteria for Single Femtosecond Pulse Ultrafast Magnetization Switching in Ferrimagnets. *Physical Review Letters* **129**, 037203 (2022). URL https://link.aps.org/doi/10.1103/PhysRevLett.129.037203.

[61] Jakobs, F. *et al.* Unifying femtosecond and picosecond single-pulse magnetic switching in Gd-Fe-Co (2021). Backup Publisher : Freie Universität Berlin.

[62] Battiato, M., Carva, K. & Oppeneer, P. M. Superdiffusive Spin Transport as a Mechanism of Ultrafast Demagnetization. *Physical Review Letters* **105**, 027203 (2010). URL https://link.aps.org/doi/10.1103/PhysRevLett.105.027203.

[63] Melnikov, A. *et al.* Ultrafast Transport of Laser-Excited Spin-Polarized Carriers in Au / Fe / MgO (001). *Physical Review Letters* **107**, 076601 (2011). URL https://link.aps.org/doi/10.1103/PhysRevLett.107.076601.

[64] Choi, G.-M., Min, B.-C., Lee, K.-J. & Cahill, D. G. Spin current generated by thermally driven ultrafast demagnetization. *Nature Communications* **5**, 4334 (2014). URL http://www.nature.com/articles/ncomms5334.

[65] Rudolf, D. *et al.* Ultrafast magnetization enhancement in metallic multilayers driven by superdiffusive spin current. *Nature Communications* **3**, 1037 (2012). URL http://www.nature.com/articles/ncomms2029.

[66] Jansen, R. The spin-valve transistor : a review and outlook. *Journal of Physics D : Applied Physics* **36**, R289–R308 (2003). URL https://iopscience.iop.org/article/10.1088/0022-3727/36/19/R01.

[67] Razdolski, I. *et al.* Nanoscale interface confinement of ultrafast spin transfer torque driving non-uniform spin dynamics. *Nature Communications* **8**, 15007 (2017). URL http://www.nature.com/articles/ncomms15007.

[68] Choi, G.-M. & Min, B.-C. Laser-driven spin generation in the conduction bands of ferrimagnetic metals. *Physical Review B* **97**, 014410 (2018). URL https://link.aps.org/doi/10.1103/PhysRevB.97.014410.

[69] Iihama, S. *et al.* Single-Shot Multi-Level All-Optical Magnetization Switching Mediated by Spin Transport. *Advanced Materials* **30**, 1804004 (2018). URL https://onlinelibrary.wiley.com/doi/10.1002/adma.201804004.

[70] Igarashi, J. *et al.* Engineering Single-Shot All-Optical Switching of Ferromagnetic Materials. *Nano Letters* **20**, 8654–8660 (2020). URL https://pubs.acs.org/doi/10.1021/acs.nanolett.0c03373.

[71] Remy, Q. *et al.* Energy Efficient Control of Ultrafast Spin Current to Induce Single Femtosecond Pulse Switching of a Ferromagnet. *Advanced Science* **7**, 2001996 (2020). URL https://onlinelibrary.wiley.com/doi/10.1002/advs.202001996.

[72] Igarashi, J. *et al.* Optically induced ultrafast magnetization switching in ferromagnetic spin valves. *Nature Materials* (2023). URL https://www.nature.com/articles/s41563-023-01499-z.

[73] Chen, J.-Y., He, L., Wang, J.-P. & Li, M. All-Optical Switching of Magnetic Tunnel Junctions with Single Subpicosecond Laser Pulses. *Physical Review Applied* **7**, 021001 (2017). URL `https://link.aps.org/doi/10.1103/PhysRevApplied.7.021001`.

[74] Wang, L. *et al.* Picosecond optospintronic tunnel junctions. *Proceedings of the National Academy of Sciences* **119**, e2204732119 (2022). URL `https://pnas.org/doi/full/10.1073/pnas.2204732119`.

[75] Kimel, A. V. & Li, M. Writing magnetic memory with ultrashort light pulses. *Nature Reviews Materials* **4**, 189–200 (2019). URL `http://www.nature.com/articles/s41578-019-0086-3`.

[76] Lalieu, M. L. M., Lavrijsen, R. & Koopmans, B. Integrating all-optical switching with spintronics. *Nature Communications* **10**, 110 (2019). URL `http://www.nature.com/articles/s41467-018-08062-4`.

[77] Li, P., Kools, T. J., Lavrijsen, R. & Koopmans, B. Ultrafast racetrack based on compensated Co/Gd-based synthetic ferrimagnet with all-optical switching (2022). URL `http://arxiv.org/abs/2204.11595`. ArXiv :2204.11595 [cond-mat].

[78] Li, P. *et al.* Enhancing all-optical switching of magnetization by He ion irradiation. *Applied Physics Letters* **121**, 172404 (2022). URL `https://aip.scitation.org/doi/10.1063/5.0111466`.

[79] Pezeshki, H. *et al.* Design of an integrated hybrid plasmonic-photonic device for all-optical switching and reading of spintronic memory (2022). URL `http://arxiv.org/abs/2209.15556`. ArXiv :2209.15556 [physics].

[80] Gorchon, J., Yang, Y. & Bokor, J. Model for multishot all-thermal all-optical switching in ferromagnets. *Physical Review B* **94**, 020409 (2016). URL `https://link.aps.org/doi/10.1103/PhysRevB.94.020409`.

[81] El Hadri, M. S. *et al.* Domain size criterion for the observation of all-optical helicity-dependent switching in magnetic thin films. *Physical Review B* **94**, 064419 (2016). URL `https://link.aps.org/doi/10.1103/PhysRevB.94.064419`.

[82] Ciuciulkaite, A. *et al.* Magnetic and all-optical switching properties of amorphous Tb x Co 100 x alloys. *Physical Review Materials* **4**, 104418 (2020). URL `https://link.aps.org/doi/10.1103/PhysRevMaterials.4.104418`.

[83] Mathias, S. *et al.* Probing the timescale of the exchange interaction in a ferromagnetic alloy. *Proceedings of the National Academy of Sciences* **109**, 4792–4797 (2012). URL `https://pnas.org/doi/full/10.1073/pnas.1201371109`.

[84] El Hadri, M. S. *et al.* Suppression of all-optical switching in He $^{+}$ -irradiated Co/Pt multilayers : influence of the domain-wall energy. *Journal of Physics D : Applied Physics* **51**, 215004 (2018). URL `https://iopscience.iop.org/article/10.1088/1361-6463/aabf2b`.

[85] Ferre, J. *et al.* Irradiation induced e!ects on magnetic properties of Pt/Co/Pt ultrathin "lms. *Journal of Magnetism and Magnetic Materials* (1999).

[86] Devolder, T. Light ion irradiation of CoÕPt systems : Structural origin of the decrease in magnetic anisotropy. *Physical Review B* **62** (2000). URL `https://journals.aps.org/prb/abstract/10.1103/PhysRevB.62.5794`.

[87] Vomir, M., Albrecht, M. & Bigot, J.-Y. Single shot all optical switching of intrinsic micron size magnetic domains of a Pt/Co/Pt ferromagnetic stack. *Applied Physics Letters* **111**, 242404 (2017). URL `http://aip.scitation.org/doi/10.1063/1.5010915`.

[88] Cheng, F. *et al.* All-Optical Helicity-Dependent Switching in Hybrid Metal–Ferromagnet Thin Films. *Advanced Optical Materials* **8**, 2000379 (2020). URL `https://onlinelibrary.wiley.com/doi/10.1002/adom.202000379`.

[89] Du, Z., Chen, C., Cheng, F., Liu, Y. & Pan, L. Prediction of Deterministic All-Optical Switching of Ferromagnetic Thin Film by Ultrafast Optothermal and Optomagnetic Couplings. *Scientific Reports* **7**, 13513 (2017). URL `http://www.nature.com/articles/s41598-017-13568-w`.

[90] Faraday, M. On the magnetization of light and the illumination of magnetic lines of force. *Philosophical Transactions of the Royal Society of London* **136**, 1–20 (1846).

[91] van der Ziel, J. P., Pershan, P. S. & Malmstrom, L. D. Optically-Induced Magnetization Resulting from the Inverse Faraday Effect. *Physical Review Letters* **15**, 190–193 (1965). URL `https://link.aps.org/doi/10.1103/PhysRevLett.15.190`.

[92] Pershan, P. S., van der Ziel, J. P. & Malmstrom, L. D. Theoretical Discussion of the Inverse Faraday Effect, Raman Scattering, and Related Phenomena. *Physical Review* **143**, 574–583 (1966). URL `https://link.aps.org/doi/10.1103/PhysRev.143.574`.

[93] Kimel, A. V. *et al.* Ultrafast non-thermal control of magnetization by instantaneous photomagnetic pulses. *Nature* **435**, 655–657 (2005). URL `http://www.nature.com/articles/nature03564`.

[94] Vahaplar, K. *et al.* All-optical magnetization reversal by circularly polarized laser pulses : Experiment and multiscale modeling. *Physical review. B, Condensed matter and materials physics* **85** (2012).

[95] Cornelissen, T. D., Córdoba, R. & Koopmans, B. Microscopic model for all optical switching in ferromagnets. *Applied physics letters* **108**, 142405– (2016). Place : Melville Publisher : American Institute of Physics.

[96] Takahashi, Y. *et al.* Accumulative Magnetic Switching of Ultrahigh-Density Recording Media by Circularly Polarized Light. *Physical Review Applied* **6**, 054004 (2016). URL https://link.aps.org/doi/10.1103/PhysRevApplied.6.054004.

[97] Tsema, Y. *et al.* Helicity and field dependent magnetization dynamics of ferromagnetic Co/Pt multilayers. *Applied Physics Letters* **109**, 072405 (2016). URL http://aip.scitation.org/doi/10.1063/1.4961246.

[98] Xiao, Y. *et al.* Magnetization Switching of L1 $_0$ -FePt Nanoparticles by Combination Effect From Multishot Circularly Polarized Laser Pulses. *IEEE Transactions on Magnetics* **54**, 1–5 (2018). URL https://ieeexplore.ieee.org/document/8419721/.

[99] Medapalli, R. *et al.* Multiscale dynamics of helicity-dependent all-optical magnetization reversal in ferromagnetic Co/Pt multilayers. *Physical Review B* **96**, 224421 (2017). URL https://link.aps.org/doi/10.1103/PhysRevB.96.224421.

[100] Hinzke, D. & Nowak, U. Domain Wall Motion by the Magnonic Spin Seebeck Effect. *Physical Review Letters* **107**, 027205 (2011). URL https://link.aps.org/doi/10.1103/PhysRevLett.107.027205.

[101] Schlickeiser, F., Ritzmann, U., Hinzke, D. & Nowak, U. Role of Entropy in Domain Wall Motion in Thermal Gradients. *Physical Review Letters* **113**, 097201 (2014). URL https://link.aps.org/doi/10.1103/PhysRevLett.113.097201.

[102] Wang, X. S. & Wang, X. R. Thermodynamic theory for thermal-gradient-driven domain-wall motion. *Physical Review B* **90**, 014414 (2014). URL https://link.aps.org/doi/10.1103/PhysRevB.90.014414.

[103] Islam, M. T., Wang, X. S. & Wang, X. R. Thermal gradient driven domain wall dynamics. *Journal of Physics : Condensed Matter* **31**, 455701 (2019). URL https://iopscience.iop.org/article/10.1088/1361-648X/ab27d6.

[104] Jiang, W. *et al.* Direct Imaging of Thermally Driven Domain Wall Motion in Magnetic Insulators. *Physical Review Letters* **110**, 177202 (2013). URL https://link.aps.org/doi/10.1103/PhysRevLett.110.177202.

[105] Uchida, K. *et al.* Observation of the spin Seebeck effect. *Nature* **455**, 778–781 (2008). URL `http://www.nature.com/articles/nature07321`.

[106] Quessab, Y. *et al.* Resolving the role of magnetic circular dichroism in multishot helicity-dependent all-optical switching. *Physical Review B* **100**, 024425 (2019). URL `https://link.aps.org/doi/10.1103/PhysRevB.100.024425`.

[107] Quessab, Y. *et al.* Helicity-dependent all-optical domain wall motion in ferromagnetic thin films. *Physical Review B* **97**, 054419 (2018). URL `http://arxiv.org/abs/1709.07645`. ArXiv : 1709.07645.

[108] Raposo, V. *et al.* Micromagnetic Modeling of All Optical Switching of Ferromagnetic Thin Films : The Role of Inverse Faraday Effect and Magnetic Circular Dichroism. *Applied Sciences* **10**, 1307 (2020). URL `https://www.mdpi.com/2076-3417/10/4/1307`.

[109] Kichin, G. *et al.* From Multiple- to Single-Pulse All-Optical Helicity-Dependent Switching in Ferromagnetic Co / Pt Multilayers. *Physical Review Applied* **12**, 024019 (2019). URL `https://link.aps.org/doi/10.1103/PhysRevApplied.12.024019`.

[110] Scheid, P., Malinowski, G., Mangin, S. & Lebègue, S. Ab initio theory of magnetization induced by light absorption in ferromagnets. *Phys. Rev. B* **100**, 214402 (2019). URL `https://link.aps.org/doi/10.1103/PhysRevB.100.214402`.

[111] Stowasser, R. & Hoffmann, R. What do the kohn- sham orbitals and eigenvalues mean ? *Journal of the american chemical society* **121**, 3414–3420 (1999).

[112] Scheid, P., Sharma, S., Malinowski, G., Mangin, S. & Lebègue, S. Ab Initio Study of Helicity-Dependent Light-Induced Demagnetization : From the Optical Regime to the Extreme Ultraviolet Regime. *Nano Letters* **21**, 1943–1947 (2021). URL `https://doi.org/10.1021/acs.nanolett.0c04166`. _eprint : https ://doi.org/10.1021/acs.nanolett.0c04166.

[113] Hinzke, D. *et al.* Domain wall properties of FePt : From Bloch to linear walls. *Physical Review B* **77**, 094407 (2008). URL `https://link.aps.org/doi/10.1103/PhysRevB.77.094407`.

[114] El Hadri, M. S., Hehn, M., Malinowski, G. & Mangin, S. Materials and devices for all-optical helicity-dependent switching. *Journal of Physics D : Applied Physics* **50**, 133002 (2017). URL `https://iopscience.iop.org/article/10.1088/1361-6463/aa5adf`.

[115] Liao, J. *et al.* Controlling All-Optical Helicity-Dependent Switching in Engineered Rare-Earth Free Synthetic Ferrimagnets. *Advanced Science* **6**, 1901876 (2019). URL `https://onlinelibrary.wiley.com/doi/10.1002/advs.201901876`.

[116] Bruno, P. *et al.* Hysteresis properties of ultrathin ferromagnetic films. *Journal of Applied Physics* **68**, 5759–5766 (1990). URL `http://aip.scitation.org/doi/10.1063/1.346944`.

[117] Zhang, B., Krishnan, K. M., Lee, C. H. & Farrow, R. F. C. Magnetic anisotropy and lattice strain in Co/Pt multilayers. *Journal of Applied Physics* **73**, 6198–6200 (1993). URL `http://aip.scitation.org/doi/10.1063/1.352696`.

[118] Engel, B. N., Wiedmann, M. H., Van Leeuwen, R. A. & Falco, C. M. Anomalous magnetic anisotropy in ultrathin transition metals. *Physical Review B* **48**, 9894–9897 (1993). URL `https://link.aps.org/doi/10.1103/PhysRevB.48.9894`.

[119] Johnson, M. T., Bloemen, P. J. H., Broeder, F. J. A. d. & Vries, J. J. d. Magnetic anisotropy in metallic multilayers. *Reports on Progress in Physics* **59**, 1409–1458 (1996). URL `https://iopscience.iop.org/article/10.1088/0034-4885/59/11/002`.

[120] Kim, J. & Shin, S. Interface roughness effects on the surface anisotropy in Co/Pt multilayer films. *Journal of Applied Physics* **80**, 3121–3123 (1996). URL `http://aip.scitation.org/doi/10.1063/1.363124`.

[121] Nakajima, N. *et al.* Perpendicular Magnetic Anisotropy Caused by Interfacial Hybridization via Enhanced Orbital Moment in Co / Pt Multilayers : Magnetic Circular X-Ray Dichroism Study. *Physical Review Letters* **81**, 5229–5232 (1998). URL `https://link.aps.org/doi/10.1103/PhysRevLett.81.5229`.

[122] Knepper, J. W. & Yang, F. Y. Oscillatory interlayer coupling in Co Pt multilayers with perpendicular anisotropy. *Physical Review B* **71**, 224403 (2005). URL `https://link.aps.org/doi/10.1103/PhysRevB.71.224403`.

[123] Gambino, R. J. & Cuomo, J. J. Selective resputtering-induced anisotropy in amorphous films. *Journal of Vacuum Science & Technology* **15** (1998).

[124] Taylor, R. C. & Gangulee, A. Magnetization and magnetic anisotropy in evaporated GdCo amorphous films. *Journal of Applied Physics* **47**, 4666–4668 (1976). URL `http://aip.scitation.org/doi/10.1063/1.322397`.

[125] Harris, V. G., Aylesworth, K. D., Das, B. N., Elam, W. T. & Koon, N. C. Structural origins of magnetic anisotropy in sputtered amorphous Tb-Fe films. *Physical*

Review Letters **69**, 1939–1942 (1992). URL https://link.aps.org/doi/10.1103/PhysRevLett.69.1939.

[126] Harris, V. G., Elam, W. T., Koon, N. C. & Hellman, F. Deposition-temperature dependence of structural anisotropy in amorphous Tb-Fe films. *Physical Review B* **49**, 3637–3640 (1994). URL https://link.aps.org/doi/10.1103/PhysRevB.49.3637.

[127] Yan, X., Hirscher, M., Egami, T. & Marinero, E. E. Direct observation of anelastic bond-orientational anisotropy in amorphous Tb 26 Fe 62 Co 12 thin films by x-ray diffraction. *Physical Review B* **43**, 9300–9303 (1991). URL https://link.aps.org/doi/10.1103/PhysRevB.43.9300.

[128] Mizoguchi, T. & Cargill III, G. S. Magnetic anisotropy from dipolar interactions in amorphous ferrimagnetic alloys. *Journal of Applied Physics* **50**, 3570–3582 (1979). URL http://aip.scitation.org/doi/10.1063/1.326303.

[129] Fu, H., Mansuripur, M. & Meystre, P. Generic source of perpendicular anisotropy in amorphous rare-earth–transition-metal films. *Physical Review Letters* **66**, 1086–1089 (1991). URL https://link.aps.org/doi/10.1103/PhysRevLett.66.1086.

[130] Cheng, S.-N., Kryder, M. & Mathur, M. Stress related anisotropy studies in DC-magnetron sputtered TbCo and TbFe films. *IEEE Transactions on Magnetics* **25**, 4018–4020 (1989). URL http://ieeexplore.ieee.org/document/42509/.

[131] Malmhäll, R. & Chen, T. Thickness dependence of magnetic hysteretic properties of rf-sputtered amorphous Tb–Fe alloy thin films. *Journal of Applied Physics* **53**, 7843–7845 (1982). URL http://aip.scitation.org/doi/10.1063/1.330216.

[132] Nakada, M., Toki, K. & Okada, M. Thickness Dependence of Effective Composition for Amorphous TbFe Films. *IEEE Translation Journal on Magnetics in Japan* **2**, 348–349 (1987). URL http://ieeexplore.ieee.org/document/4549437/.

[133] Hebler, B., Hassdenteufel, A., Reinhardt, P., Karl, H. & Albrecht, M. Ferrimagnetic Tb–Fe Alloy Thin Films : Composition and Thickness Dependence of Magnetic Properties and All-Optical Switching. *Frontiers in Materials* **3** (2016). URL http://journal.frontiersin.org/Article/10.3389/fmats.2016.00008/abstract.

[134] Ishibashi, M. *et al.* Ferrimagnetic compensation and its thickness dependence in TbFeCo alloy thin films. *Applied Physics Letters* **120**, 022405 (2022). URL https://aip.scitation.org/doi/10.1063/5.0078873.

[135] Sato, J. *et al.* Pinning Effect Induced by Underlayer in TbFeCo Magnetic Recording Media. *Japanese Journal of Applied Physics* **47**, 150–153 (2008). URL `https://iopscience.iop.org/article/10.1143/JJAP.47.150`.

[136] Yin, S. Q., Li, X. Q., Xu, X. G., Miao, J. & Jiang, Y. Effect of Ta Underlayer on Perpendicular Anisotropy of TbFeCo Films. *IEEE Transactions on Magnetics* **47**, 3129–3131 (2011). URL `https://ieeexplore.ieee.org/document/6028231/`.

[137] Tang, M., Chen, S., Zhang, X., Zhang, Z. & Jin, Q. Y. Investigation and Effective Control of Perpendicular Magnetic Anisotropy for TbCo Films with Different Underlayers. *SPIN* **06**, 1650009 (2016). URL `https://www.worldscientific.com/doi/abs/10.1142/S2010324716500090`.

[138] Jiang, H., Zhang, W., Zhang, W. & Peng, B. Effects of argon pressure on magnetic properties and low-field magnetostriction of amorphous TbFe films. *Physica B : Condensed Matter* **405**, 834–838 (2010). URL `https://linkinghub.elsevier.com/retrieve/pii/S0921452609006450`.

[139] Na, S. M., Suh, S. J. & Lim, S. H. Fabrication condition effects on the magnetic and magnetostrictive properties of sputtered Tb-Fe thin films. *Journal of Applied Physics* **93**, 8507–8509 (2003). URL `http://aip.scitation.org/doi/10.1063/1.1543870`.

[140] Katayama, T., Hasegawa, K., Kawanishi, K. & Tsushima, T. Annealing effects on magnetic properties of amorphous GdCo, GdFe, and GdCoMo films. *Journal of Applied Physics* **49**, 1759–1761 (1978). URL `http://aip.scitation.org/doi/10.1063/1.324859`.

[141] Ueda, K., Tan, A. J. & Beach, G. S. D. Effect of annealing on magnetic properties in ferrimagnetic GdCo alloy films with bulk perpendicular magnetic anisotropy. *AIP Advances* **8**, 125204 (2018). URL `http://aip.scitation.org/doi/10.1063/1.5054164`.

[142] Kerr, J. Xliii. on rotation of the plane of polarization by reflection from the pole of a magnet. *The London, Edinburgh, and Dublin Philosophical Magazine and Journal of Science* **3**, 321–343 (1877).

[143] Kerr, J. Xxiv. on reflection of polarized light from the equatorial surface of a magnet. *The London, Edinburgh, and Dublin Philosophical Magazine and Journal of Science* **5**, 161–177 (1878).

[144] Ebert, H. Magneto-optical effects in transition metal systems. *Reports on Progress in Physics* **59**, 1665–1735 (1996). URL `https://iopscience.iop.org/article/10.1088/0034-4885/59/12/003`.

[145] Phillips, D. George porter (1920–2002). *Nature* **419**, 578–578 (2002).

[146] Ellis, M. O. A., Fullerton, E. E. & Chantrell, R. W. All-optical switching in granular ferromagnets caused by magnetic circular dichroism. *Scientific Reports* **6**, 30522 (2016). URL `http://www.nature.com/articles/srep30522`.

[147] Hall, E. H. Xviii. on the "rotational coefficient" in nickel and cobalt. *The London, Edinburgh, and Dublin Philosophical Magazine and Journal of Science* **12**, 157–172 (1881).

[148] Moritz, J., Rodmacq, B., Auffret, S. & Dieny, B. Extraordinary Hall effect in thin magnetic films and its potential for sensors, memories and magnetic logic applications. *Journal of Physics D : Applied Physics* **41**, 135001 (2008). URL `https://iopscience.iop.org/article/10.1088/0022-3727/41/13/135001`.

[149] Moretti, S., Raposo, V., Martinez, E. & Lopez-Diaz, L. Domain wall motion by localized temperature gradients. *Physical Review B* **95**, 064419 (2017). URL `https://link.aps.org/doi/10.1103/PhysRevB.95.064419`.

[150] Evans, R. & Fan, W. Atomistic simulation of sub-nanosecond non-equilibrium field cooling processes for magnetic data storage applications. *Applied Physics Letters* **105**, 192405 (2014).

[151] Chen, X.-J. Fundamental mechanism for all-optical helicity-dependent switching of magnetization. *Scientific Reports* **7**, 41294 (2017). URL `http://www.nature.com/articles/srep41294`.

[152] Ono, T., Miyajima, H., Shigeto, K. & Shinjo, T. Magnetization reversal in submicron magnetic wire studied by using giant magnetoresistance effect. *Applied Physics Letters* **72**, 1116–1117 (1998). URL `http://aip.scitation.org/doi/10.1063/1.120941`.

[153] Ono, T. *et al.* Propagation of a Magnetic Domain Wall in a Submicrometer Magnetic Wire. *Science (American Association for the Advancement of Science)* **284**, 468–470 (1999). Place : Washington, DC Publisher : American Society for the Advancement of Science.

[154] Atkinson, D. *et al.* Magnetic domain-wall dynamics in a submicrometre ferromagnetic structure. *Nature Materials* **2**, 85–87 (2003). URL `https://www.nature.com/articles/nmat803`.

[155] Kondou, K., Ohshima, N., Kasai, S., Nakatani, Y. & Ono, T. Single Shot Detection of the Magnetic Domain Wall Motion by Using Tunnel Magnetoresistance Effect.

Applied Physics Express **1**, 061302 (2008). URL https://iopscience.iop.org/article/10.1143/APEX.1.061302.

[156] Metaxas, P. J. *et al.* Creep and flow regimes of magnetic domain wall motion in ultrathin Pt/Co/Pt films with perpendicular anisotropy. *Physical Review Letters* **99**, 217208 (2007). URL http://arxiv.org/abs/cond-mat/0702654. ArXiv :cond-mat/0702654.

[157] Schryer, N. L. & Walker, L. R. The motion of 180 domain walls in uniform dc magnetic fields. *Journal of Applied Physics* **45**, 5406–5421 (1974). URL http://aip.scitation.org/doi/10.1063/1.1663252.

[158] Yang, J., Nistor, C., Beach, G. S. D. & Erskine, J. L. Magnetic domain-wall velocity oscillations in permalloy nanowires. *Physical Review B* **77**, 014413 (2008). URL https://link.aps.org/doi/10.1103/PhysRevB.77.014413.

[159] Berger, L. Exchange interaction between ferromagnetic domain wall and electric current in very thin metallic films. *Journal of Applied Physics* **55**, 1954–1956 (1984). URL http://aip.scitation.org/doi/10.1063/1.333530.

[160] Thiaville, A., Nakatani, Y., Miltat, J. & Suzuki, Y. Micromagnetic understanding of current-driven domain wall motion in patterned nanowires. *Europhysics Letters (EPL)* **69**, 990–996 (2005). URL https://iopscience.iop.org/article/10.1209/epl/i2004-10452-6.

[161] DuttaGupta, S. *et al.* Adiabatic spin-transfer-torque-induced domain wall creep in a magnetic metal. *Nature Physics* **12**, 333–336 (2016). URL http://www.nature.com/articles/nphys3593.

[162] Koyama, T. *et al.* Magnetic field insensitivity of magnetic domain wall velocity induced by electrical current in Co/Ni nanowire. *Applied Physics Letters* **98**, 192509 (2011). URL http://aip.scitation.org/doi/10.1063/1.3590713.

[163] Ngo, D.-T., Ikeda, K. & Awano, H. Direct Observation of Domain Wall Motion Induced by Low-Current Density in TbFeCo Wires. *Applied Physics Express* **4**, 093002 (2011). URL https://iopscience.iop.org/article/10.1143/APEX.4.093002.

[164] Moore, T. A. *et al.* High domain wall velocities induced by current in ultrathin Pt/Co/AlOx wires with perpendicular magnetic anisotropy. *Applied Physics Letters* **93**, 262504 (2008). URL http://aip.scitation.org/doi/10.1063/1.3062855.

[165] Miron, I. M. *et al.* Fast current-induced domain-wall motion controlled by the Rashba effect. *Nature Materials* **10**, 419–423 (2011). URL `https://www.nature.com/articles/nmat3020`.

[166] Mihai Miron, I. *et al.* Current-driven spin torque induced by the Rashba effect in a ferromagnetic metal layer. *Nature Materials* **9**, 230–234 (2010). URL `https://www.nature.com/articles/nmat2613`.

[167] Haazen, P. P. J. *et al.* Domain wall depinning governed by the spin Hall effect. *Nature Materials* **12**, 299–303 (2013). URL `https://www.nature.com/articles/nmat3553`.

[168] Emori, S., Bauer, U., Ahn, S.-M., Martinez, E. & Beach, G. S. D. Current-driven dynamics of chiral ferromagnetic domain walls. *Nature Materials* **12**, 611–616 (2013). URL `https://www.nature.com/articles/nmat3675`.

[169] Hoffmann, A. Spin Hall Effects in Metals. *IEEE Transactions on Magnetics* **49**, 5172–5193 (2013). URL `https://ieeexplore.ieee.org/document/6516040/`.

[170] Goldsmid, H. J. *Introduction to Thermoelectricity*. Springer Series in Materials Science, 121 (Springer Berlin Heidelberg, Berlin, Heidelberg, 2010), 1st ed. 2010. edn.

[171] Bauer, G. E. W., Saitoh, E. & van Wees, B. J. Spin caloritronics. *Nature Materials* **11**, 391–399 (2012). URL `https://www.nature.com/articles/nmat3301`.

[172] Wang, X.-g., Guo, G.-h., Nie, Y.-z., Zhang, G.-f. & Li, Z.-x. Domain wall motion induced by the magnonic spin current. *Physical Review B* **86**, 054445 (2012).

[173] Lemerle, S. *et al.* Domain Wall Creep in an Ising Ultrathin Magnetic Film. *Physical Review Letters* **80**, 849–852 (1998). URL `https://link.aps.org/doi/10.1103/PhysRevLett.80.849`.

[174] Gorchon, J. *et al.* Pinning-Dependent Field-Driven Domain Wall Dynamics and Thermal Scaling in an Ultrathin Pt / Co / Pt Magnetic Film. *Physical Review Letters* **113**, 027205 (2014). URL `https://link.aps.org/doi/10.1103/PhysRevLett.113.027205`.

[175] Bustingorry, S., Kolton, A. B. & Giamarchi, T. Thermal rounding of the depinning transition in ultrathin Pt/Co/Pt films. *Physical Review B* **85**, 214416 (2012). URL `http://arxiv.org/abs/1204.0969`. ArXiv :1204.0969 [cond-mat].

[176] Bigot, J.-Y., Vomir, M. & Beaurepaire, E. Coherent ultrafast magnetism induced by femtosecond laser pulses. *Nature Physics* **5**, 515–520 (2009). URL `http://www.nature.com/articles/nphys1285`.

[177] Kiss, A., Szolnoki, L. & Simon, F. The Elliott-Yafet theory of spin relaxation generalized for large spin-orbit coupling. *Scientific Reports* **6**, 22706 (2016). URL http://www.nature.com/articles/srep22706.

[178] Zhang, G. P. & Hübner, W. Laser-Induced Ultrafast Demagnetization in Ferromagnetic Metals. *Physical Review Letters* **85**, 3025–3028 (2000). URL https://link.aps.org/doi/10.1103/PhysRevLett.85.3025.

[179] Yafet, Y. g factors and spin-lattice relaxation of conduction electrons. In *Solid state physics*, vol. 14, 1–98 (Elsevier, 1963).

[180] Seigler, M. A. *et al.* Integrated Heat Assisted Magnetic Recording Head : Design and Recording Demonstration. *IEEE Transactions on Magnetics* **44**, 119–124 (2008). URL http://ieeexplore.ieee.org/document/4407610/.

[181] Zhao, W. *et al.* Failure and reliability analysis of STT-MRAM. *Microelectronics Reliability* **52**, 1848–1852 (2012). URL https://linkinghub.elsevier.com/retrieve/pii/S0026271412002326.

[182] Parkin, S. S. P., Hayashi, M. & Thomas, L. Magnetic Domain-Wall Racetrack Memory. *Science* **320**, 190–194 (2008). URL https://www.science.org/doi/10.1126/science.1145799.

[183] Breitkreutz, S. *et al.* Time-dependent domain wall nucleation probability in field-coupled nanomagnets with perpendicular anisotropy. *Journal of Applied Physics* **117**, 17B503 (2015). URL http://aip.scitation.org/doi/10.1063/1.4906440.

[184] Fukumoto, K. *et al.* Dynamics of Magnetic Domain Wall Motion after Nucleation : Dependence on the Wall Energy. *Physical Review Letters* **96**, 097204 (2006). URL https://link.aps.org/doi/10.1103/PhysRevLett.96.097204.

[185] Park, H. S., Baskin, J. S. & Zewail, A. H. 4D Lorentz Electron Microscopy Imaging : Magnetic Domain Wall Nucleation, Reversal, and Wave Velocity. *Nano Letters* **10**, 3796–3803 (2010). URL https://pubs.acs.org/doi/10.1021/nl102861e.

[186] Zhang, X. *et al.* Direct Observation of Domain-Wall Surface Tension by Deflating or Inflating a Magnetic Bubble. *Physical Review Applied* **9**, 024032 (2018). URL https://link.aps.org/doi/10.1103/PhysRevApplied.9.024032.

[187] Gaunt, P. The frequency constant for thermal activitation of a ferromagnetic domain wall. *Journal of Applied Physics* **48**, 3470–3474 (1977). URL http://aip.scitation.org/doi/10.1063/1.324195.

[188] Hansen, P., Clausen, C., Much, G., Rosenkranz, M. & Witter, K. Magnetic and magneto-optical properties of rare-earth transition-metal alloys containing Gd, Tb, Fe, Co. *Journal of Applied Physics* **66**, 756–767 (1989). URL http://aip.scitation.org/doi/10.1063/1.343551.

[189] Stanciu, C. D. *et al.* Ultrafast spin dynamics across compensation points in ferrimagnetic GdFeCo : The role of angular momentum compensation. *Physical Review B* **73**, 220402 (2006). URL https://link.aps.org/doi/10.1103/PhysRevB.73.220402.

[190] Gao, S., Cai, R., Xiong, W. & Xu, C. Influence of a damping parameter on helicity-independent all-optical switching. *Optics express* **29**, 32535–32546 (2021).

[191] Gridnev, V. N. Role of compensation points in all-optical magnetization switching. *Physical Review B* **100**, 174405 (2019). URL https://link.aps.org/doi/10.1103/PhysRevB.100.174405.

[192] Russek, S. E. *et al.* Magnetostriction and angular dependence of ferromagnetic resonance linewidth in Tb-doped Ni[sub 0.8]Fe[sub 0.2] thin films. *Journal of Applied Physics* **91**, 8659 (2002). URL http://scitation.aip.org/content/aip/journal/jap/91/10/10.1063/1.1452708.

[193] Radu, I. *et al.* Laser-Induced Magnetization Dynamics of Lanthanide-Doped Permalloy Thin Films. *Physical Review Letters* **102**, 117201 (2009). URL https://link.aps.org/doi/10.1103/PhysRevLett.102.117201.

[194] Woltersdorf, G., Kiessling, M., Meyer, G., Thiele, J.-U. & Back, C. H. Damping by Slow Relaxing Rare Earth Impurities in Ni 80 Fe 20. *Physical Review Letters* **102**, 257602 (2009). URL https://link.aps.org/doi/10.1103/PhysRevLett.102.257602.

[195] Bainsla, L. *et al.* Ultrathin Ferrimagnetic GdFeCo Films with Low Damping. *Advanced Functional Materials* **32**, 2111693 (2022). URL https://onlinelibrary.wiley.com/doi/10.1002/adfm.202111693.

[196] Zhang, W. *et al.* Role of spin-lattice coupling in ultrafast demagnetization and all optical helicity-independent single-shot switching in Gd 1 x y Tb y Co x alloys. *Physical Review B* **105**, 054410 (2022). URL https://link.aps.org/doi/10.1103/PhysRevB.105.054410.

[197] Spence, D. E., Kean, P. N. & Sibbett, W. 60-fsec pulse generation from a self-mode-locked Ti :sapphire laser. *Optics Letters* **16**, 42 (1991). URL https://opg.optica.org/abstract.cfm?URI=ol-16-1-42.

[198] Nisoli, M. *et al.* Compression of high-energy laser pulses below 5 fs. *Optics Letters* **22**, 522 (1997). URL `https://opg.optica.org/abstract.cfm?URI=ol-22-8-522`.

[199] Remy, Q. *et al.* Accelerating ultrafast magnetization reversal by non-local spin transfer. *Nature Communications* **14**, 445 (2023). URL `https://www.nature.com/articles/s41467-023-36164-1`.

[200] Xu, Z., Zhou, S., Ge, J., Du, J. & Sun, L. Magnetization reversal mechanism of perpendicularly exchange-coupled composite l 1 0-fept/cocrpt bilayers. *Journal of Applied Physics* **105**, 123903 (2009).

[201] Davies, J. E. *et al.* Magnetization reversal of Co Pt multilayers : Microscopic origin of high-field magnetic irreversibility. *Physical Review B* **70**, 224434 (2004). URL `https://link.aps.org/doi/10.1103/PhysRevB.70.224434`.

[202] Jhuria, K. *et al.* Spin–orbit torque switching of a ferromagnet with picosecond electrical pulses. *Nature Electronics* **3**, 680–686 (2020). URL `https://www.nature.com/articles/s41928-020-00488-3`.

[203] Chubykalo-Fesenko, O., Nowak, U., Chantrell, R. W. & Garanin, D. Dynamic approach for micromagnetics close to the Curie temperature. *Physical Review B* **74**, 094436 (2006). URL `https://link.aps.org/doi/10.1103/PhysRevB.74.094436`.

[204] Hoveyda, F., Hohenstein, E., Judge, R. & Smadici, S. Ultrafast demagnetization at high temperatures. *Journal of Physics : Condensed Matter* **30**, 195802 (2018). URL `https://iopscience.iop.org/article/10.1088/1361-648X/aab9f1`.

[205] Koopmans, B., Ruigrok, J. J. M., Longa, F. D. & de Jonge, W. J. M. Unifying Ultrafast Magnetization Dynamics. *Physical Review Letters* **95**, 267207 (2005). URL `https://link.aps.org/doi/10.1103/PhysRevLett.95.267207`.